Spring 2015

Advancements in uncertainty quantification with stochastic expansions applied to supersonic and hypersonic flows

Thomas Kelsey West IV

Department: Mechanical and Aerospace Engineering

ADVANCEMENTS IN UNCERTAINTY QUANTIFICATION WITH STOCHASTIC EXPANSIONS APPLIED TO SUPERSONIC AND HYPERSONIC FLOWS

by

THOMAS KELSEY WEST IV

A DISSERTATION

Presented to the Faculty of the Graduate School of the

MISSOURI UNIVERSITY OF SCIENCE AND TECHNOLOGY

In Partial Fulfillment of the Requirements for the Degree

DOCTOR OF PHILOSOPHY

in

AEROSPACE ENGINEERING

2015

Approved by

Dr. Serhat Hosder, Advisor
Dr. David W. Riggins
Dr. Xiaoping Du
Dr. K. M. Isaac
Dr. Luca Maddalena

ABSTRACT

The primary objective of this study was to develop improved methodologies for efficient and accurate uncertainty quantification with stochastic expansions and apply them to problems in supersonic and hypersonic flows. Methods introduced included approaches for efficient dimension reduction, sensitivity analysis, and sparse approximations. These methods and procedures were demonstrated on multiple stochastic models of hypersonic, planetary entry flows, which included high-fidelity, computational fluid dynamics models of radiative heating on the surface of hypersonic inflatable aerodynamic decelerators during Mars and Titan entry. For these stochastic problems, construction of an accurate surrogate model was achieved with as few as 10% of the number of model evaluations needed to construct a full dimension, total order expansion. Another objective of this work was to introduce methodologies used for further advancement of a quantification of margins and uncertainties framework. First, the use of stochastic expansions was introduced to efficiently quantify the uncertainty in system design performance metrics and performance boundaries. Then, procedures were defined to measure margin and uncertainty metrics for systems subject to multiple types of uncertainty in operating conditions and physical models. To demonstrate the new quantification of margins and uncertainties methodologies, two multi-system, multi-physics stochastic models were investigated: (1) a model for reentry dynamics, control, and convective heating and (2) a model of ground noise prediction of low-boom, supersonic aircraft configurations. Overall the methods and results of this work have outlined many effective approaches to uncertainty quantification of large-scale, high-dimension, aerospace problems containing both epistemic and inherent uncertainty. The methods presented showed significant improvement in the efficiency and accuracy of uncertainty analysis capability when stochastic expansions were used for uncertainty quantification.

ACKNOWLEDGMENTS

I would like to sincerely thank my advisor, Dr. Serhat Hosder, for the opportunity and honor he has bestowed upon me by working with me over my entire graduate school career. He has given me the utmost dedication and guidance in developing me into not only a better student and researcher, but also a better person. I cannot begin to express my gratitude for the time, effort, and patience Dr. Hosder as dedicated to me as my advisor.

I would like to thank my committee members, Dr. David Riggins, Dr. Xiaoping Du, Dr. K. M. Isaac, and Dr. Luca Maddalena for their dedication, support, and time commitment to this research. I would like to thank Dr. Christopher Johnston from the NASA Langley Research Center for his invaluable support of this work. I would also like to thank my fellow graduate students Andrew Brune and Harsheel Shah for many discussions and much collaboration on this research.

I would like to thank the Department of Mechanical and Aerospace Engineering at the Missouri University of Science and Technology for a great educational opportunity, as well as the provided facilities and funding. Partial funding for this work was provided by NASA STTR grant no. NNX11CC60C and M4 Engineering Inc. I would also like to thank the NASA-Missouri Space Grant Consortium and the Missouri S&T Chancellor's Fellowship program for additional funding. I would like to thank Dr. Eric Walker for his support and for providing me with multiple internship opportunities at the NASA Langley Research Center.

Finally, I absolutely must thank my family and fiancée for their love and support over the course of my education. This has been a long and trying road. Without them, I would not be where I am today, and this work would not have been possible.

TABLE OF CONTENTS

LIST OF ILLUSTRATIONS

LIST OF TABLES

NOMENCLATURE

A_{el}	Leading rate (Arrhenius) constant for electron-impact excitation
$A_{f,i}$	Leading rate (Arrhenius) constant for chemical kinetic reaction i
A_{hp}	Leading rate (Arrhenius) constant for heavy-particle impact excitation
CR	Confidence Ratio
c_i	Mass Fraction of Species i
D	Total statistical variance
$D_{f,i}$	Characteristic temperature for chemical kinetic rate constant i
$D_{i_1,\ldots,i_s}$	Partial statistical variance
E_{el}	Characteristic temperature for electron-impact excitation
E_{hp}	Characteristic temperature for heavy-particle impact excitation
F_{actual}	Response value from deterministic model
$F_{surr.}$	Response value from surrogate model
F	Performance Metric
FL	Lower Performance Limit
FU	Upper Performance Limit
h	Enthalpy or Altitude (km)
h_D	Enthalpy of Diffusion (J/kg)
h_f^0	Heat of Formation (J/kmol)
h_0	Totoal Enthalpy (J/kg)
$K_{f,ij}^{el}$	Forward reaction rate for the electron-impact excitation from electronic state i to j ($\mathrm{cm^3 s^{-1}}$)
$K_{f,ij}^{hp}$	Forward reaction rate for the heavy-particle excitation from electronic state i to j ($\mathrm{cm^3 s^{-1}}$)

$k_{f,i}$	Forward rate for chemical reaction i ($\mathrm{cm^3 mole^{-1} s^{-1}}$)
Le	Lewis Number
M_{UP}	Upper Performance Gate Margin
M_{LW}	Lower Performance Gate Margin
m	mass (kg)
N_s	Number of samples
N_t	Number of terms in a total-order polynomial chaos expansion
N_{TP}	Number of test points
n	Number of random dimensions
n_{el}	Temperature exponent for electron-impact excitation
$n_{f,i}$	Temperature exponent for chemical kinetic reaction i
n_{hp}	Temperature exponent for heavy-particle impact excitation
P	Number of output modes or Pressure (Pa)
Pr	Prandtl Number
p	Order of polynomial expansion
$\dot{q}$	Heat Flux (W/cm^2)
q_λ	Monochromatic radiative heating ($\mathrm{Wcm^{-2}}$)
r	Orbital Radius (km)
S	Reference Area ($\mathrm{m^2}$)
S_e	Percent absolute error
$S_{i_1,\ldots,i_s}$	Partial Sobol index
S_T	Total Sobol index
s	Down Range Distance (km)
T	Temperature (K)
T_a	Dissociation controlling average temperature defined as $(\mathrm{T}_{tr}\mathrm{T}_{ve})^{1/2}$
T_e	Test point error

T_x	Temperature, where $x = ve$ or tr for vibrational or rotational modes
U_F	Performance Metric Uncertainty
U_{FU}	Upper Performance Limit Uncertainty
U_{FL}	Lower Performance Limit Uncertainty
U_{UP}	Upper Performance Gate Uncertainty
U_{LW}	Lower Performance Gate Uncertainty
U	Velocity (m/s)
x	Independent input random variable
α	Deterministic coefficient in the polynomial chaos expansion
α^*	Generic uncertain function
β	Confidence Level
γ	Flight Path Angle (Deg.)
δ	Truncation error
ϵ	Wall Emissivity
θ	Longitude (Deg.)
λ	Wavelength (nm)
μ	Dynamic Viscosity (kg/m-s)
μ_e	Mean error
ξ	Standard input random variable
ρ	Density (kg/m^3)
σ	Bank Angle or Stefan-Boltzmann Constant ($5.67x10^{-8}\ W/m^2 - K^4$)
Ψ	Random basis function or Heading Angle (Deg.)
ϕ	Latitude (Deg.)
ω	Planetary Body Rotation Rate (rad/s)

Subscripts

w	Wall Condition
e	Boundary Layer Edge Condition
∞	Free Stream Condition
r	Radiation
c	Conduction
d	Diffusion

1. INTRODUCTION

1.1. MOTIVATION FOR UNCERTAINTY QUANTIFICATION

With recent advancements in computational hardware and numerical algorithms, computational fluid dynamics (CFD) has become one of the main tools used in the analysis and design of aerospace vehicles and systems. In complex aerospace engineering problems, reliability and robustness is a key component of the design process. The challenge is that many of the models have a significant amount of nondeterministic parameters that make assessing the reliability and the robustness a substantial obstacle due to the cost associated with quantifying the effect of the nondeterministic parameters on design quantities. A particular area of interest are models of supersonic and hypersonic flows. These models may be difficult due to the complexity of the physics governing, not only the fluid dynamics, but also the thermodynamics, heat transfer, and chemical kinetics.

Uncertainty quantification (UQ) of large-scale, highly complex models with large amounts of uncertainty can be challenging due to the computational demand of sophisticated deterministic models. Traditional uncertainty propagation is done with sampling approaches, such as Monte Carlo. The challenge with this approach is that numerous samples ($\sim 10^5$) are typically required for accurate results. High-fidelity, numerical models tend to be extremely expensive, which may make traditional sampling techniques impractical or infeasible for performing an accurate UQ analysis. Therefore, there is a strong demand for UQ methods that can provide

computationally efficient and accurate results with a minimal number of deterministic model evaluations.

1.2. OBJECTIVES OF THE CURRENT STUDY

The primary objective of this study is to develop improved methodologies for efficient and accurate UQ with stochastic expansions and apply them to problems in supersonic and hypersonic flows. Methods to be introduced include approaches for efficient dimension reduction, sensitivity analysis, and sparse approximations. These new tools will allow for efficient and accurate analysis of stochastic models with a large number of both aleatory (inherent) and epistemic uncertainties. When developing these methods, the focus is to reduce the number of computationally expensive model evaluations, while maintaining the accuracy of the uncertainty analysis.

A second objective of this work is to define procedures for an improved quantification of margins and uncertainties (QMU) framework for the analysis of aerospace systems subject to multiple types of uncertainty in the operating conditions and physical models used in the calculation of the design condition and performance boundaries. In many engineering applications, uncertainty representation in design conditions may be different than the representation of the performance boundaries. Representation may be a pure probabilistic representation, an interval based representation, or a combination of the two (i.e., mixed uncertainty). There may also be instances when no uncertainty exists in performance limits. This may be typical when trying to meet some specific design criteria. The goal is to outline how measures can be made between these different uncertainty representations to provide an accurate estimation of the reliability of the system and/or performance metrics. In addition, a secondary objective is to demonstrate the use of stochastic response surfaces for efficient quantification of uncertainty in system performance metrics, as well as performance boundaries.

The methods and procedures developed in this study will be demonstrated on multiple stochastic models of supersonic and hypersonic flows. For the supersonic flow regime, a high-fidelity, CFD models of low-boom, supersonic, cruise vehicles is investigated for the prediction of ground level noise. In the hypersonic flow regime, high-fidelity, CFD simulations of shock-layer, radiative heating on the surface of a vehicle during planetary entry are investigated. Because of the large amount of uncertainty that exist in the models and their computational expense, they are of particular interest in terms of, not only the challenge they pose as stochastic models, but also their application to cutting edge research, model development, and design.

1.3. CONTRIBUTIONS OF THE CURRENT STUDY

The first contribution of this study is the development of a multi-step UQ process for high-fidelity, hypersonic re-entry flow simulations, which may include a large number of both aleatory and epistemic uncertainties. This process is aimed to reduce the computational cost in terms of the required number of deterministic model evaluations necessary for accurate UQ with a stochastic expansion. The key components of this process include a sensitivity-based dimension reduction scheme based on the approximation of global sensitivities with local sensitivities. Then, a methodology is implemented to update the existing deterministic response values in the reduced dimension stochastic problem, which allows for the reuse of existing response values. Lastly, a modification of the existing point-collocation non-intrusive polynomial chaos (NIPC) method is performed to incorporate the use of response sensitivities, as well as the response values at the selected collocation locations in the determination of the polynomial chaos expansion (PCE) coefficients.

The second contribution of this work is the investigation and application of sparse approximations of PCEs. The goal is introduce alternative measures of accuracy for PCE coefficients and to present approaches for determining their

convergence while iteratively increasing sample size. The accuracy and convergence of the PCE coefficients are measured in two ways. The first is by determining the global, nonlinear sensitivity of each uncertain parameter based on the variance obtained from the PCE. The second method is by measuring the accuracy of the polynomial chaos response surface when compared to selected test points distributed throughout the design space. These approaches have the advantage of implicitly monitoring the change in all of the PCE coefficients while not being significantly affected by changes in weakly contributing uncertain variables, which may yield little to no change in the overall response. The goal is, again, to minimize the number of computationally expensive deterministic model evaluations needed for an accurate UQ analysis.

A third contribution is the improvement of the QMU framework methodology and efficiency. This includes demonstrating the use of stochastic response surfaces based on NIPC for efficient quantification of uncertainty in system performance metrics, as well as performance boundaries and the definition of procedures to calculate the margin and uncertainty metrics of systems containing multiple types of uncertainty in the design condition and performance limits.

The final contribution of this study is the uncertainty analysis of the various high-speed flow model problems. Uncertainty and sensitivity analysis of low-boom, supersonic, cruise vehicles has not previously been investigated. With the industry moving towards commercial supersonic flight over populated areas, assessment of the uncertainty in ground noise predictions is critical for facilitating low-boom configuration design approaches. The shock-layer, radiation models investigated for planetary entry, hypersonic flows are particularly interesting due to the shear amount of uncertainty that exists in these complex models. While previous studies (which will be discussed later) have performed uncertainty analysis on some of these models, they have not been as rigorous or as inclusive of as many sources of uncertainty as will be investigated in the current study. The uncertainty analysis of all of these models

will aid the design of reliable and robust aerospace vehicles by informing resource allocation for model improvement and the management and reduction of uncertainty in these models.

1.4. DISSERTATION OUTLINE

The following section provides a brief literature review of UQ with stochastic expansions and previously investigated stochastic models in supersonic and hypersonic flows. Section 3 describes the types of uncertainty in numerical modeling and provides a discussion of mixed uncertainty propagation. Section 4 describes the basics of polynomial chaos expansions and details of the non-intrusive point-collocation technique. Section 5 outlines approaches for global sensitivities analyses. Section 6 then introduces the multi-step UQ approach, which is applied to two stochastic models of hypersonic flows. Section 7 introduces the sparse approximation of the polynomial chaos expansion technique, which is applied to three stochastic model problems of hypersonic flows. Section 8 then discusses the quantification of margins and uncertainties for aerospace systems. Two mutli-system models including reentry trajectory modeling and sonic-boom loudness predictions are investigated. Lastly, Section 9 discusses important conclusions from this study and outlines possible future work areas.

2. LITERATURE REVIEW

The following literature review considers two main topics. The first subsection includes a review of previous studies on advancements and application of stochastic expansions as a means of uncertainty quantification. The second subsection includes a review of the quantification of margins and uncertainties (QMU) methodologies.

2.1. UNCERTAINTY QUANTIFICATION WITH STOCHASTIC EXPANSIONS

The use of stochastic expansions in the analysis of nondeterministic engineering problems has become an increasingly popular approach in the last few decades. The original theory on polynomial chaos was introduced by Norbert Wiener in 1938 [2]. He presented the idea of modeling a stochastic process or chaos with a series of polynomials that represent the statistical parameters of the process. Since then, many efforts have been made to build upon and generalize the work of Wiener, many of which are presented by Ghanem and Spanos [3]. Work by Xiu and Karniadakis [4] outlined an approach for representing a stochastic process with on optimal basis from the Askey set of orthogonal polynomials, which allowed for reduced dimensionality and improved error convergence.

More recently, many uncertainty quantification (UQ) studies have been conducted on extending the applicability and capability of using stochastic expansions as a means of efficient UQ. Walters and Huse [5] surveyed methods in UQ, including polynomial chaos, and their application to fluid mechanics. Work by Najm [6] reviewed UQ and polynomial chaos techniques in computational fluid dynamics. Hosder and Bettis [7] investigated using non-intrusive polynomial chaos (NIPC) as a means of efficient propagation of mixed aleatory and epistemic uncertainties in reentry

flows. Bettis et al. [8] applied NIPC to a multidisciplinary analysis of reusable launch vehicles. Works by Hosder et al. [9, 10] investigated efficient sampling approaches and the use of the point-collocation NIPC technique. Furthermore, Eldred [11] summarized recent advancements in NIPC methodologies for uncertainty analysis and design.

As with many surrogate modeling approaches, gradient-enhancement may be used to improve accuracy and reduce computational cost. With regards to polynomial chaos, previous studies by Lockwood et al. [12] and Roderick et al. [13] have investigated incorporating gradient information into the point-collocation NIPC approach and a means of enhancing the stochastic expansion and improving the UQ analysis. These works utilized adjoint-based techniques to obtain local sensitivity information that was used to improve surrogate models created with regression methods at a reduced computational cost over performing additional deterministic function evaluations.

One weakness of polynomial chaos is dependence on the number of uncertainty sources, or random variables. While developing methods to alleviate this dependency is one focus of the current study, work by Doostan and Owhadi [14] has shown that the polynomial chaos expansion (PCE) coefficients can be recovered from a sparse sample set with a compressive sampling approach. This involved casting a sparse point-collocation NIPC formulation into an optimization problem to recover the PCE coefficients from the underdetermined system of equations. This technique was applied to model problems of large dimension to demonstrate the potential of the method in using fewer number of samples than normally required to construct the PCE directly.

In the area of supersonic and hypersonic flow uncertainty analysis with stochastic expansions, there has been a limited number of studies beyond those already mentioned. For supersonic flows, work by Witteveen et al. [15] used

polynomial chaos for uncertainty quantification and error estimation in scramjet simulations. Hosder and Maddalena [16] used NIPC to efficiently quantify the uncertainty in supersonic pressure probe design. Suga and Yamazaki [17] performed uncertainty quantification of the aerodynamics of a supersonic biplane with polynomial chaos. In the hypersonic flow regime, a study by Kulakhmetov and Alexeenko [18] used polynomial chaos to quantify the uncertainty in hypersonic leading-edge flows.

2.2. QUANTIFICATION OF MARGINS AND UNCERTAINTIES

Quantification of Margins and Uncertainties (QMU) is a methodology developed to facilitate analysis and communication of confidence for certification of complex systems. This is performed with quantified uncertainty and margin metrics obtained for various system responses and performance parameters [19]. In recent years, a number of studies were reported on the theoretical development and the application of the QMU concept. The description of the key elements of a QMU framework was presented by Sharp and Wood-Schultz [19], who used the QMU methodology for the certification of nuclear weapons. Eardley et al. [20] described QMU as a formalism dealing with the reliability of complex technical systems, and the confidence which can be placed in estimates of reliability. They also investigated the main components (performance gates, margins, and uncertainties) of QMU methodology. Pilch et al. [21] presented the main ideas underlying QMU, who also emphasized the need to separate aleatory and epistemic uncertainty in QMU. Helton [22] presented a comprehensive study on the QMU, which included a detailed analysis of the concept with different representations of uncertainty. Romero [23] discussed the issues and needs in QMU of complex coupled systems. Pepin et al. [24] presented a practical QMU metric for the certification of complex systems, which allowed uncertainty both on the operating region and the performance requirement and was not restrictive

to a probabilistic definition of the uncertainty. A QMU approach was used for the characterization of the operational limits of the supersonic combustion engine of a hypersonic air-breathing vehicle by Iaccarino et al. [25]. A study by Lucas et al. [26] used the QMU methodology to study the reliability of a ring structure. Swiler et al. [27] studied various approaches to characterize epistemic uncertainty in the calculation of margins.

3. TYPES OF UNCERTAINTY AND UNCERTAINTY PROPAGATION

A critical step in any uncertainty analysis is the classification of the uncertain parameters. These parameters may be mathematically represented differently based on the nature of the uncertainty source. Incorrect classification and/or treatment of uncertain parameters can result in widely different ranges of output uncertainty. The objective of this section is to describe the two main categories of uncertainty that exist in numerical modeling and outline a procedure for propagating the uncertainty through stochastic models.

3.1. TYPES OF UNCERTAINTY IN HIGH-SPEED FLOWS

Two main types of uncertainty exist in numerical modeling: aleatory uncertainty and epistemic uncertainty [28]. Aleatory uncertainty is the inherent variation of a physical system. Such variation is due to the random nature of input data and can be mathematically represented by a probability density function if substantial experimental data is available for estimating the distribution type. By definition, these variables are not controllable and are assumed to be as well understood as possible in terms of their uncertain nature. This type of uncertainty is, therefore, sometimes referred to as irreducible uncertainty. An example of this for stochastic CFD simulations could be the fluctuation in freestream quantities such as velocity, temperature, and density. An additional example of this uncertainty is manufacturing tolerances.

Aleatory uncertainty is propagated through a stochastic model by sampling the distribution of each parameter and then calculating the output from model with in the design points. Because the inputs are probabilistic in nature, the outputs also carry an associated probability of occurrence. By rigorously sampling within the design space,

the probabilistic realizations can be used to create a discrete cumulative distribution function of the output from the stochastic model problem.

Epistemic uncertainty in a stochastic problem comes from several potential sources. These include a lack of knowledge or incomplete information of the behavior of a particular variable. Also, ignorance or negligence with regards to accurate treatment of model input parameters is a source of epistemic uncertainty. Contrary to aleatory uncertainty, epistemic uncertainty is sometimes referred to as reducible uncertainty. An increase in knowledge regarding the physics of a problem, along with accurate modeling, can reduce the amount of this type of uncertainty. Epistemic uncertainty is typically modeled using intervals because the use of probabilistic distributions (even a uniform distribution) can lead to inaccurate predictions in the amount of uncertainty in a system. Upper and lower bounds of these intervals can be drawn from limited experimental data or from expert predictions and judgment [7, 8].

An additional, special case of epistemic uncertainty is numerical error. This uncertainty is common in numerical modeling and is defined as a recognizable deficiency in any phase or activity of modeling and simulations that is not due to lack of knowledge of the physical system. In CFD, an example of this type of uncertainty would be the discretization error in both the temporal and spatial domains that comes from the numerical solution of the partial differential equations that govern the system [8]. This uncertainty can be well understood and controlled through code verification and grid convergence studies.

Epistemic uncertainty can be propagated through a stochastic model in multiple ways. The traditional approach is to rigorously sample the uncertainty space, much like with the aleatory uncertainty. The difference now is that because epistemic uncertainty, by definition, carries no probabilistic meaning, the realizations form the uncertainty space are viewed simply as possible outcomes, but have the same

probability of occurrence as any other output. What is of interest then is the maximum and minimum possible occurrences. Large sample sizes can be used to approximate these boundaries.

As an alternative, because we are only interested in the limits of the uncertain output, optimization on the domain of the epistemic input parameters can be used so seek out the maximum and minimum output values. Eldred and Swiler [29] discuss that this optimization can be performed using a variety of local and global optimization methods. While the optimization approach is generally assumed to provide the most accurate result (assuming that no local extrema is found that is not the interval bound), the computational cost of the optimization may be significant with a very large number of uncertain variables.

3.2. MIXED UNCERTAINTY PROPAGATION

Many stochastic problems may contain both epistemic and aleatory uncertainty. The desired approach is to consider the contribution of both types of uncertainty simultaneously by propagating this mixed uncertainty through the stochastic model. This can be done using a procedure known as second-order probability [29]. Second-order probability is a type of double loop sampling, shown in Figure 3.1, and can also be implemented using a Monte Carlo sampling approach of the deterministic model. When using stochastic expansions, the NIPC response surface can be used within second-order probability in place of the deterministic code. In the outer loop, a vector of specific values for the epistemic variables is passed into the inner loop where the stochastic response surface resulting from the NIPC process is sampled for the single epistemic sample vector and every aleatory sample vector. The process is repeated for all of the epistemic sample vectors. This means that the total number of samples of the NIPC response surface is the number of epistemic samples times the number of aleatory samples.

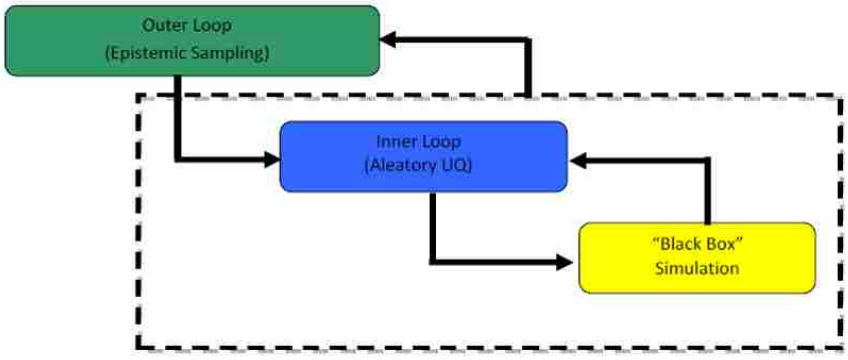

Figure 3.1. Schematic of Second-Order Probability

Each iteration of the outer loop generates a cumulative distribution function (CDF) based on the aleatory uncertainty analysis in the inner loop. After completion of the process, what remains is a series of CDFs, which, when plotted, gives intervals of the output variable from the model at different probability levels (i.e., a probability or "P-box" representation of mixed uncertainty output). Important information can be taken from P-boxes, including confidence intervals. For the case of mixed uncertainty, one approach to obtaining the 95% confidence interval, for example, is to take the upper 97.5% probability level and the lower 2.5% probability level as the interval. The P-box and confidence interval measurement are illustrated in Figure 3.2. Note that the boundaries of the P-box are typically hold the greatest interest during analysis and design, as will be shown in later sections.

Note that a combination of sampling and optimization can also be implemented to potentially reduce the computational expense for large-scale problems. In this approach, the outer loop is first evaluated with a small number of samples to determine robust estimates for the initial values of the epistemic variables used in optimization. The optimization is then performed with these initial starting points for minimizing or maximizing the response at selected probability levels.

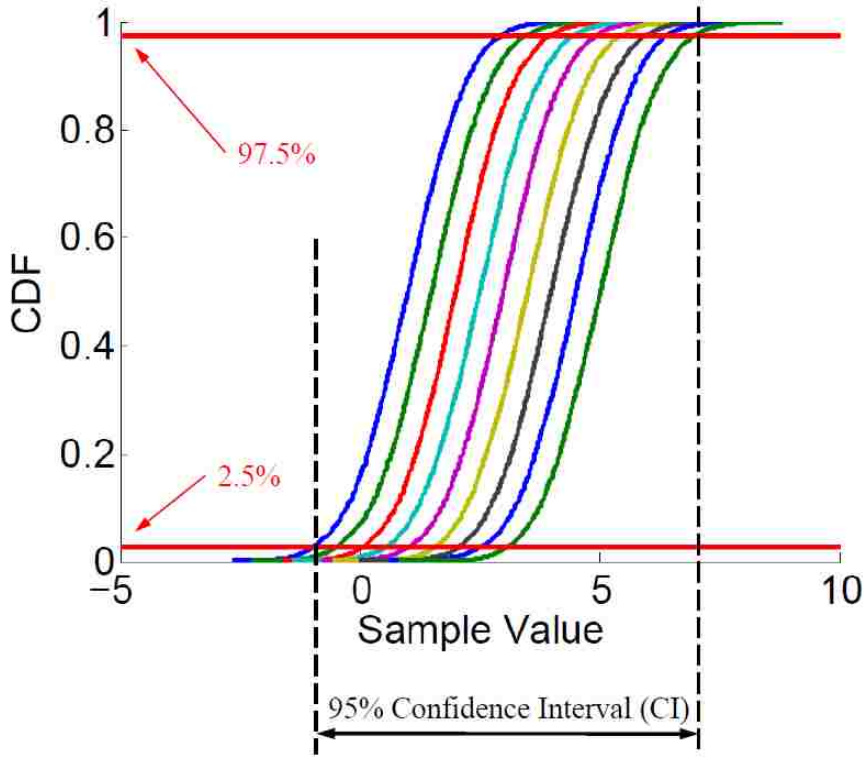

Figure 3.2. P-box Representation of Mixed Uncertainty Output and Confidence Interval Measurement

4. POLYNOMIAL CHAOS EXPANSIONS

This section provides the details of the polynomial chaos techniques used in this study. The first part outlines the general polynomial chaos expansion formulation. Then, the point-collocation non-intrusive approach is discussed. Among this, difference methodologies are described including the general point-collocation approach and gradient enhancement.

4.1. BASICS OF POLYNOMIAL CHAOS

In recent studies, [7, 8, 10, 30, 31] the polynomial chaos method has been used as a means of UQ over traditional methods, such as Monte Carlo, for computational efficiency. Polynomial chaos is a surrogate modeling technique based on the spectral representation of the uncertainty. An important aspect of spectral representation of uncertainty is that a response value or random function α^* can be decomposed into separable deterministic and stochastic components, as shown in Eq. (1).

$$\alpha^*(\mathbf{x}, \boldsymbol{\xi}) \approx \sum_{i=0}^{P} \alpha_i(\mathbf{x}) \Psi_i(\boldsymbol{\xi}) \tag{1}$$

Here, α_i is the deterministic component and Ψ_i is the random variable basis functions corresponding to the ith mode. α^* is assumed to be a function of the vector $\mathbf{x}$ of independent random variables and the n-dimensional standard random variable vector $\boldsymbol{\xi}$. Note that this series is, by definition, an infinite series. However, in practice, it is truncated and a discrete sum is taken over a number of output modes [11]. To form a complete basis or for a total order expansion, N_t terms are required, which can be computed from Eq. (2) for a PCE of order p and a number of random dimensions or variables, n.

$$N_t = P + 1 = \frac{(n+p)!}{n!p!} \tag{2}$$

Further details on polynomial chaos theory are given by Ghanem [3] and Eldred [11].

The objective with any PCE method is to determine the expansion coefficients, α_i. To do this, polynomial chaos methods can be implemented using an intrusive or a non-intrusive approach. While an intrusive method may appear straightforward in theory, for complex problems this process may be time consuming, expensive, and difficult to implement [7]. In contrast, the non-intrusive approach can be easily implemented to construct a surrogate model that represents a complex computational simulation, because no modification to the deterministic model is required. The non-intrusive methods require only the response (or sensitivity) [32, 12, 13] values at selected sample points to approximate the stochastic response surface.

Polynomial chaos can be implemented using an intrusive or a non-intrusive approach. While an intrusive methods may appear straightforward in theory, for complex problems this process may be time consuming, expensive, and difficult to implement [7]. In contrast, the non-intrusive approach can be easily implemented to model the uncertainty propagation in complex computational simulations, since no modification to the deterministic model is required. The non-intrusive methods require only the response (or sensitivity) [33, 12, 13] values at selected sample points to approximate the stochastic response surface.

4.2. POINT COLLOCATION NON-INTRUSIVE POLYNOMIAL CHAOS

4.2.1. General Approach. Several methods have been developed for NIPC including spectral projection, sparse collocation, and sampling approaches [11]. Of these, the point-collocation NIPC method has been used extensively in many aerospace simulations and CFD problems [8, 10, 31, 32] and is the focus of this work.

The point-collocation method starts with replacing a stochastic response or random function with its PCE using Eq. (1). Then, N_t vectors are chosen in random space and the deterministic code is then evaluated at these points, which is the left hand side of Eq. (1). Following this, a linear system of N_t equations can be formulated and solved for the spectral modes of the random variables. This system is shown in Eq. (3).

$$\begin{pmatrix} \Psi_0(\boldsymbol{\xi}_0) & \Psi_1(\boldsymbol{\xi}_0) & \cdots & \Psi_P(\boldsymbol{\xi}_0) \\ \Psi_0(\boldsymbol{\xi}_1) & \Psi_1(\boldsymbol{\xi}_1) & \cdots & \Psi_P(\boldsymbol{\xi}_1) \\ \vdots & \vdots & \ddots & \vdots \\ \Psi_0(\boldsymbol{\xi}_P) & \Psi_1(\boldsymbol{\xi}_P) & \cdots & \Psi_P(\boldsymbol{\xi}_P) \end{pmatrix} \begin{pmatrix} \alpha_0 \\ \alpha_1 \\ \vdots \\ \alpha_P \end{pmatrix} = \begin{pmatrix} \alpha^*(\mathbf{x}, \boldsymbol{\xi}_0) \\ \alpha^*(\mathbf{x}, \boldsymbol{\xi}_1) \\ \vdots \\ \alpha^*(\mathbf{x}, \boldsymbol{\xi}_P) \end{pmatrix} \tag{3}$$

Note that for this linear system, N_t is the minimum number of deterministic samples required to obtain an analytical solution (i.e., the coefficient vector). If more samples are available and that are linearly independent, the system is considered overdetermined and can be solved using a least squares approach. The number of samples over the required minimum is represented by the use of an oversampling ratio (OSR), defined as the ratio of number of actual samples to the minimum number required (i.e., N_t). In general, the number of collocation points can be determined by multiplying Eq. (2) by an OSR. Hosder et al.[9] determined an effective OSR of two for the stochastic model problems studied. Later in Section 7, an approach will be discussed for recovering a solution when the system in Eq. (3) is underdetermined.

4.2.2. Sensitivity-Based Approach. The general point-collocation approach can be expanded on to include gradients in calculating the expansion coefficients. In surrogate modeling, this commonly refereed to as gradient enhancement. When using the point-collocation NIPC approach, the gradient formulation can be developed by first differentiating Eq. (1) with respect to a standard random variable as shown in Eq. (4)

$$\frac{\partial \alpha^*(\mathbf{x}, \boldsymbol{\xi})}{\partial \xi_i} \approx \sum_{i=0}^{P} \alpha_i(\mathbf{x}) \frac{\partial \Psi_i(\boldsymbol{\xi})}{\partial \xi_i} \tag{4}$$

Then, expanding the LHS yields Eq. (5):

$$\frac{\partial \alpha^*(\mathbf{x}, \boldsymbol{\xi})}{\partial x_i} \frac{\partial x_i}{\partial \xi_i} \approx \sum_{i=0}^{P} \alpha_i(\mathbf{x}) \frac{\partial \Psi_i(\boldsymbol{\xi})}{\partial \xi_i} \tag{5}$$

Note that the first derivative on the on the LHS is the sensitivity derivative obtained from the local SA. The second derivative is based on the distribution of the input uncertain variable and is known. An example for a normally distributed variable with mean μ and standard deviation σ is shown in Eq. (6):

$$x_i = \sigma \xi_i + \mu \rightarrow \frac{\partial x_i}{\partial \xi_i} = \sigma \tag{6}$$

The differentiated polynomial chaos expansion with respect to each uncertain variable at each sample point (Eq. (5)) can be appended to the linear system shown in Eq. (3). The new system of linear equations is shown in Eq. (7). Note that the dimensions of the coefficient matrix is $N_S(N+1)$ by N_t, the solution vector has dimension $N_S(N+1)$, and the unknown vector has dimensions N_t.

$$
\begin{pmatrix}
\Psi_0(\boldsymbol{\xi}_0) & \Psi_1(\boldsymbol{\xi}_0) & \cdots & \Psi_P(\boldsymbol{\xi}_0) \\
\frac{\partial \Psi_0(\boldsymbol{\xi}_0)}{\partial \xi_1} & \frac{\partial \Psi_1(\boldsymbol{\xi}_0)}{\partial \xi_1} & \cdots & \frac{\partial \Psi_P(\boldsymbol{\xi}_0)}{\partial \xi_1} \\
\vdots & \vdots & \ddots & \vdots \\
\frac{\partial \Psi_0(\boldsymbol{\xi}_0)}{\partial \xi_N} & \frac{\partial \Psi_1(\boldsymbol{\xi}_0)}{\partial \xi_N} & \cdots & \frac{\partial \Psi_P(\boldsymbol{\xi}_0)}{\partial \xi_N} \\
\Psi_0(\boldsymbol{\xi}_1) & \Psi_1(\boldsymbol{\xi}_1) & \cdots & \Psi_P(\boldsymbol{\xi}_1) \\
\frac{\partial \Psi_0(\boldsymbol{\xi}_1)}{\partial \xi_1} & \frac{\partial \Psi_1(\boldsymbol{\xi}_1)}{\partial \xi_1} & \cdots & \frac{\partial \Psi_P(\boldsymbol{\xi}_1)}{\partial \xi_1} \\
\vdots & \vdots & \ddots & \vdots \\
\frac{\partial \Psi_0(\boldsymbol{\xi}_1)}{\partial \xi_N} & \frac{\partial \Psi_1(\boldsymbol{\xi}_1)}{\partial \xi_N} & \cdots & \frac{\partial \Psi_P(\boldsymbol{\xi}_1)}{\partial \xi_N} \\
\vdots & \vdots & \ddots & \vdots \\
\vdots & \vdots & \ddots & \vdots \\
\Psi_0(\boldsymbol{\xi}_{N_s-1}) & \Psi_1(\boldsymbol{\xi}_{N_s-1}) & \cdots & \Psi_P(\boldsymbol{\xi}_{N_s-1}) \\
\frac{\partial \Psi_0(\boldsymbol{\xi}_{N_s-1})}{\partial \xi_1} & \frac{\partial \Psi_1(\boldsymbol{\xi}_{N_s-1})}{\partial \xi_1} & \cdots & \frac{\partial \Psi_P(\boldsymbol{\xi}_{N_s-1})}{\partial \xi_1} \\
\vdots & \vdots & \ddots & \vdots \\
\frac{\partial \Psi_0(\boldsymbol{\xi}_{N_s-1})}{\partial \xi_N} & \frac{\partial \Psi_1(\boldsymbol{\xi}_{N_s-1})}{\partial \xi_N} & \cdots & \frac{\partial \Psi_P(\boldsymbol{\xi}_{N_s-1})}{\partial \xi_N}
\end{pmatrix}
\begin{pmatrix}
\alpha_0 \\ \alpha_1 \\ \alpha_2 \\ \vdots \\ \vdots \\ \vdots \\ \vdots \\ \vdots \\ \vdots \\ \vdots \\ \vdots \\ \alpha_P
\end{pmatrix}
=
\begin{pmatrix}
\alpha^*(\mathbf{x}, \boldsymbol{\xi}_0) \\
\frac{\partial \alpha^*(\mathbf{x}, \boldsymbol{\xi}_0)}{\partial x_1} \frac{\partial x_1}{\partial \xi_1} \\
\vdots \\
\frac{\partial \alpha^*(\mathbf{x}, \boldsymbol{\xi}_0)}{\partial x_N} \frac{\partial x_N}{\partial \xi_N} \\
\alpha^*(\mathbf{x}, \boldsymbol{\xi}_1) \\
\frac{\partial \alpha^*(\mathbf{x}, \boldsymbol{\xi}_1)}{\partial x_1} \frac{\partial x_1}{\partial \xi_1} \\
\vdots \\
\frac{\partial \alpha^*(\mathbf{x}, \boldsymbol{\xi}_1)}{\partial x_N} \frac{\partial x_N}{\partial \xi_N} \\
\vdots \\
\vdots \\
\alpha^*(\mathbf{x}, \boldsymbol{\xi}_{N_s-1}) \\
\frac{\partial \alpha^*(\mathbf{x}, \boldsymbol{\xi}_{N_s-1})}{\partial x_1} \frac{\partial x_1}{\partial \xi_1} \\
\vdots \\
\frac{\partial \alpha^*(\mathbf{x}, \boldsymbol{\xi}_{N_s-1})}{\partial x_N} \frac{\partial x_N}{\partial \xi_N}
\end{pmatrix}
\tag{7}
$$

Note that the derivatives of the basis polynomials in the LHS of Eq. (7) can be obtained either analytically or through finite differencing. The solution procedure is no different than that used for the original point-collocation scheme. However, this modified scheme makes use of gradients, which can be obtained through a sensitivity analysis a priori. This approach has the advantage of reducing the number of samples needed to construct the surrogate model. This assumes that the cost of computing the local sensitivities is less than the cost of the actual model solution.

5. GLOBAL SENSITIVITY ANALYSIS METHODS

An important part of uncertainty quantification is determining the sensitivity of a model to each input uncertain variable. The purpose of this section is to outline methods for global sensitivity analyses.

5.1. GLOBAL NONLINEAR SENSITIVITIES VIA SOBOL INDICES

One appraoch to determining the global, nonlinear sensitivity values of each uncertain parameter can be done using an approach known as Sobol indices [34]. Sobol indices can be derived using Sobol Decomposition, which is a variance-based global sensitivity analysis method. True advantage of this approach, in the context of this study, is that it aligns well with information already provided in a polynomial chaos expansion (PCE). First, the total variance, D, can be written in terms of the PCE as shown in Eq. (8).

$$D = \sum_{j=1}^{P} \alpha_j^2(t, \vec{x}) \left\langle \Psi_j^2(\vec{\xi}) \right\rangle \tag{8}$$

Then, the total variance can be decomposed as:

$$D = \sum_{i=1}^{i=n} D_i + \sum_{1 \le i < j \le n}^{i=n-1} D_{i,j} + \sum_{1 \le i < j < k \le n}^{i=n-2} D_{i,j,k} + \cdots + D_{1,2,\ldots,n} \tag{9}$$

where the partial variances ($D_{i_1,\ldots,i_s}$) are given by:

$$D_{i_1,\ldots,i_s} = \sum_{\beta \in \{i_1,\ldots,i_s\}} \alpha_\beta^2 \left\langle \Psi_\beta^2(\vec{\xi}) \right\rangle, \qquad 1 \le i_1 < \ldots < i_s \le n \tag{10}$$

Then the Sobol indices ($S_{i_1 \cdots i_s}$) are defined as,

$$S_{i_1 \cdots i_s} = \frac{D_{i_1,\ldots,i_s}}{D} \tag{11}$$

which satisfy the following equation:

$$\sum_{i=1}^{i=n} S_i + \sum_{1\le i<j\le n}^{i=n-1} S_{i,j} + \sum_{1\le i<j<k\le n}^{i=n-2} S_{i,j,k} + \cdots + S_{1,2,\ldots,n} = 1.0 \tag{12}$$

The Sobol indices provide a varianced-based sensitivity measure due to individual contribution from each input uncertain variable (S_i), as well as the mixed contributions ($\{S_{i,j}\}, \{S_{i,j,k}\}, \cdots$). As shown by Sudret [34] and Ghaffari et al. [35], the total (combined) effect (S_{T_i}) of an input parameter i is defined as the summation of the partial Sobol indices that include the particular parameter:

$$S_{T_i} = \sum_{L_i} \frac{D_{i_1,\ldots,i_s}}{D}; \quad L_i = \{(i_1, \ldots, i_s) : \exists\, k,\ 1 \le k \le s,\ i_k = i\} \tag{13}$$

For example, with $n = 3$, the total contribution to the overall variance from the first uncertain variable ($i = 1$) can be written as:

$$S_{T_1} = S_1 + S_{1,2} + S_{1,3} + S_{1,2,3} \tag{14}$$

From these formulations, it can be seen that the Sobol indices can be used to provide a relative ranking of each input uncertainty to the overall variation in the output, with the consideration of nonlinear correlations between the input variables and the output quantities of interest.

5.2. GLOBAL SENSITIVITY APPROXIMATION VIA LOCAL SENSITIVITIES

Another approach to determinig the global sensitivies is an approach based on a local sensitivity analysis. A local sensitivity analysis is the most common form of sensitivity analysis as it is simple and computationally cheap for simple models. Mathematically, a local sensitivity analysis is performed by differentiating a function (response) with respect to an uncertain variable at a sample point. This is typically

performed with respect to each uncertain variable to rank the variables in order of greatest sensitivity at that particular sample location.

A couple of drawbacks to this method do exist. First and foremost is the differentiation requirement. For complex models, analytical derivatives may be difficult to obtain. Some CFD solvers may provide accurate sensitivities through the solution of automatic differentiation, complex step methods, or adjoint equations. Currently, however, many hypersonic legacy CFD codes lack these capabilities. An alternaive is to calculate the sensitivities through the use of finite difference approximations. Eq. (15) gives a first-order forward finite difference approximation of the derivative of the response function F with respect to the i_{th} variable, x_i, at sample point j.

$$S_{i,j} = \left(\frac{\partial F}{\partial x_i}\right) = \frac{F(x_{i,j} + \Delta x_i) - F(x_{i,j})}{\Delta x_i} + O(\Delta x_i) \tag{15}$$

Note here that Δx_i is a small step size equal to the nominal value of variable x_i times a global step size (e.g., $\sim 10^{-6}$). This implies that the step size is different for each variable. This ensures that the relative step size is the same for each variable in the instance when the uncertain variables are of different orders of magnitude. The step size used in the evaluation of the finite difference approximations was determined based on the achievement of the first order asymptotic truncation error convergence at multiple sample points that correspond to different locations in the uncertainty space. Note that the selection of a first order finite difference was made to limit the required number of deterministic code evaluations in determining the sensitivity derivatives. Higher order differences could be used, but with an added cost of additional deterministic model evaluations.

The local sensitivity approach provides the sensitivity information at a particular sample point. For a proper ranking of the uncertain variables in a stochastic problem, the sensitivity of the response (output) with respect to each uncertain

variable should be considered over the entire domain of each uncertain variable. To achieve this with a local sensitivity based approach, one approach is to take multiple samples distributed throughout the uncertainty space. Note that the number of samples influences the computational cost of this approach. For each sample, two evaluations of the deterministic code are necessary to calculate the sensitivity per uncertain variable. In general, this means that $N_S(N+1)$ function evaluations are required for N number of uncertain variables and N_S number of samples. Note again that alternative approaches to calculate the derivatives, such as those obtained through adjoint methods, would improve the accuracy of the sensitivity derivatives and may come at a reduced computational cost over the deterministic code samples required for the evaluation of the above finite difference approximation.

An approximation of the global response sensitivity with respect to each uncertain variable across the entire uncertainty space can be made by first computing an average of the local sensitivity values for each uncertain variable, as shown in Eq. (16).

$$\bar{S}_i = \frac{\sum_{j=1}^{N_s} |S_{i,j}|}{N_s} \Delta h_i \tag{16}$$

In this equation, Δh_i is the range of each uncertain variable (the maximum minus the minimum value for each uncertain variable.) The sensitivities $S_{i,j}$ are the local sensitivity values calculated using Eq. (15). A variance-based approximation to the total output uncertainty of each variable is then given by Eq. (17) as:

$$G_i = \frac{(\bar{S}_i)^2}{\sum_{i=1}^{N} (\bar{S}_i)^2} \tag{17}$$

Here, G_i is defined as the approximation to the global sensitivity of the response with respect to ith uncertain variable. This metric, which will be between 0 and 1, can be used for ranking each uncertain variable based on its contribution to the output

variance when other methods such as Sobol Indices (global nonlinear sensitivity) are not possible due to the computational cost (i.e., when only small sample sizes of the model are possible.) The sensitivities calculated by Eq. (17) are global linear sensitivity approximations constructed through the use of local sensitivities and they are expected to be accurate indicators used for the dimension reduction process for uncertainty quantification of nonlinear, but smooth responses.

For large scale, complex problems with highly nonlinear responses, determining local or global sensitivities from a global response surface (surrogate model) fit to the data may not be an accurate approach. Due to the computational cost, the sample size may not be sufficiently large for an accurate surrogate fit to the data. Therefore, the first step will be to reduce the dimensions of the problem so that an accurate stochastic fit to the data can be achieved in the reduced problem. In addition, Latin Hypercube sampling is used to improve the coverage of each uncertain parameter and the calculation of its sensitivity over the entire uncertainty space.

6. MULTI-STEP UNCERTAINTY QUANTIFICATION

Many models of high-speed flows may possess a significant number of uncertainty sources. When using stochastic expansions, a large number of uncertain variables may be problematic because a large number of deterministic model evaluations may be required to construct an accurate surrogate model. In these cases, one approach may be to reduce the number of random dimensions, which in turn will reduce the number of model evaluations needed to construct a stochastic expansion. In this section, a process is outlined that can be used for dimension reduction and efficient construction of a stochastic surrogate.

6.1. COMPONENTS AND PROCESS

To reduce the number of random dimensions, the importance of each uncertain variable with respect to the output quantity of interest must be determined. This can be done through a global sensitivity analysis. The complication is that many global sensitivity analysis approaches, such as scatter plotting, require large sample sizes. In this study, the global sensitivity approximation (G_i approximation) approach outlined in Section 5.2 may be used as an alternative means of global sensitivity approximation.

In addition to the potential computational cost savings, using local sensitivities provides not only a sensitivity of each uncertain variable with respect to the output quantity for each sample point, but also the sample value. This means that for N_s samples of the uncertainty space, N_s model response values and $N_s \times N_0$ sensitivities are created for N_0 uncertain parameters. When using the G_i approach with local sensitivities obtained through first-order finite differencing, the number of computational model evaluations is then $N_s(N_0+1)$. Choosing the number of samples

necessary for the sensitivity analysis may be based on resource availability, time, or by tracking the convergence of the global sensitivities.

After performing the sensitivity analysis and ranking all of the uncertain variables in terms of their importance, the next step is to decide how many variables should be retained. This selection will be depended on the type of analysis. If the analysis is on a conceptual level, eliminating more of the uncertainty may be acceptable to produce results more quickly. On the contrary, final design assessment may require better estimates of the uncertainty. The dimension reduction will also depend on the results of the sensitivity analysis. For example, if a large number of the uncertainty parameters contributed very little to uncertainty, eliminating those parameters that contribute less than a specified percentage to the total output uncertainty may be acceptable. In the end, there is no prescribed metric to how many parameters can or should be reduced. This decision is left to the engineer.

When reducing the dimensions of a stochastic problem, the desired approach is to reuse the original samples taken for the sensitivity analysis to achieve computational efficiency. This may reduce or eliminate the need for additional deterministic code evaluations to construct the surrogate model. One approach is to make the existing N_s samples independent of the input uncertain variables that are to be eliminated. This can be done with a simple Taylor series expansion and retaining the first-order terms as shown in Eq. (18), where the response F at the j^{th} sample point is made independent of the i^{th} variable, for a total number of k variables to be eliminated.

$$\tilde{F}_j = F_j + \sum_{i=1}^{k} \frac{\partial F_j}{\partial x_i}(x_i^0 - x_i^j) \tag{18}$$

Here, x_i^0 is the nominal (baseline) value of the i^{th} eliminated variable and x_i^j is the random variable value corresponding to the j^{th} deterministic sample. For a uniformly

or normally distributed value, the nominal value may be taken as the mean value of the random variable. The derivative term in this equation is the sensitivity obtained from the local sensitivity analysis. The update procedure given with Eq. (18) allows for the reuse of deterministic response values $\tilde{F}_j$ for further uncertainty analysis in the reduced dimension, which contributes to the efficiency of overall multi-step UQ process. Note that the accuracy of this first-order approximation is dependent on the magnitude of the sensitivity derivative. For dimension reduction, this derivative is small for weakly dependent variables making Eq. (18) an accurate approximation.

After reducing the dimensions of the problem to a more manageable level, the polynomial chaos expansion can be constructed. To further improve the computational efficiency, the gradient-enhanced polynomial chaos expansion discussed in Section 4.2.2 can be implemented as part of the multi-step UQ process. As local sensitivity information is already available, the linear system given in Eq. (7) can be assembled and solved for the polynomial chaos coefficients. Note that after performing the dimension reduction, more samples may need to be generated to met the minimum number of samples and sensitivities requirement given by Eq. (2), which allows for a direct solution of the linear system. After constructing the surrogate model, the uncertainty can be efficiently propagated through the model.

The steps of the multi-step UQ process are given below. This process is also shown in a flow chart in Figure 6.1. The purpose of step six of this process is to add the option of further exploring a problem in the reduced dimension. The desired approach may be to improve the accuracy of the reduced dimension response surface by adding more sample points to the original sample set and/or increasing the order of the polynomial expansion. The last step is merely an indicator that this process can be repeated using the existing information in the reduced dimension.

1. Select a number of samples (N_S) at which the deterministic model will be evaluated to calculate the response and the local sensitivities.

2. Perform a local sensitivity analysis and obtain the G_i (approximation to global sensitivity) values to estimate and rank the contribution of each uncertain variable to the total output variance.

3. Select the variables to be eliminated. The number of variables to be retained may be based on a specified number (e.g., retain the first "N_r" number of uncertain variables in the ranking) or may be based on a specified amount of the total variance to be covered out of the total (e.g., retain the variables which account for 90% of total variance).

4. Perform the deterministic sample update in Eq. (18) for each of the existing deterministic samples. Note that when normalizing the samples such that they are independent of the selected variables, the sensitivities of the model to these variables are lost (i.e., become zero) and therefore cannot be used as part of the modified point-collocation scheme.

5. Solve Eq. (7) for the polynomial chaos response surface.

6. Repeat this multi-step process (steps 2 through 5) if necessary.

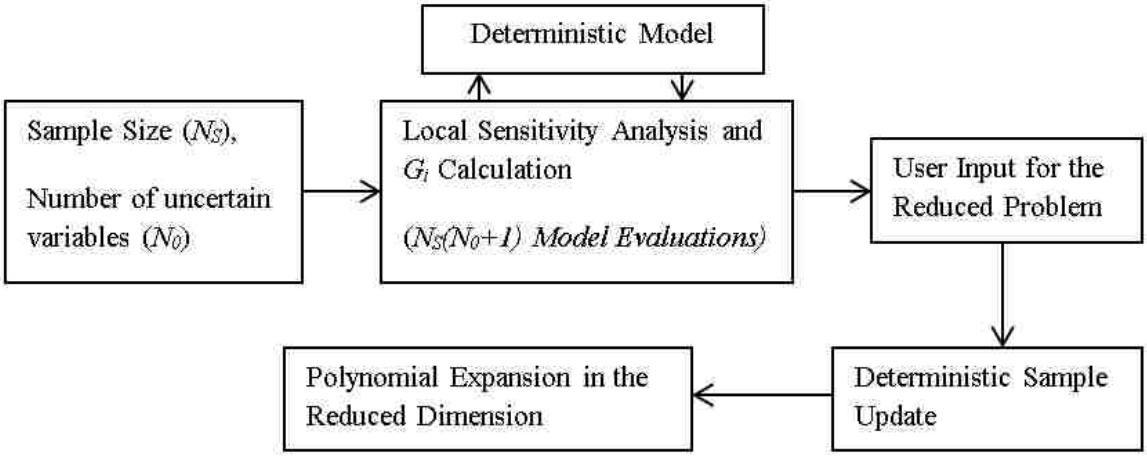

Figure 6.1. Multi-Step UQ Framework Flow Chart

6.2. DEMONSTRATION PROBLEMS

To demonstrate the capability and key aspects of the multi-step UQ process, two model problems are investigated. the first is a stochastic model used for the prediction of stagnation point convective heat transfer of blunt bodies in hypersonic flow. The second model is a high-fiedlity, computational fluid dynamics model used for the prediction of radiative heat transfer on the surface of a vehicle during hypersonic entry into Mars. For each problem, a description of the deterministic model and the stochastic problem are given, along with a discussion of the results and the applicability of the multi-step UQ approach.

6.2.1. Stagnation-Point Convective Heat Transfer in Hypersonic Flow. The Fay and Riddell [36] correlation can be used to approximate the stagnation point heat transfer for a blunt body in hypersonic flow. This model assumes a laminar boundary layer, thermo-chemical equilibrium flow, and a fully catalytic wall. The model is shown in Eq. (19).

$$\dot{q}_w = 0.76(Pr^{-0.6})(\rho_w\mu_w)^{0.1}(\rho_e\mu_e)^{0.4}\sqrt{\frac{du_e}{dx}}(h_{0_e} - h_w)\left(1 + (Le^{0.52} - 1)\frac{h_D}{h_{0_e}}\right) \tag{19}$$

where,

$$\frac{du_e}{dx} = \frac{1}{R_n}\sqrt{\frac{2(P_e - P_\infty)}{\rho_e}} \tag{20}$$

$$h_D = \sum_i c_i(h_f^0)_i \tag{21}$$

In the above equations, Pr is the Prandtl number, Le is the Lewis number, R_n is the radius of curvature of the body, h_D is the dissociation enthalpy, c_i is the mass fraction of the atomic species within the boundary layer, and $(h_f^0)_i$ is heat of

formation of atomic species i. Note also that the subscripts w and e represent the wall and boundary layer edge quantities, respectively. For this problem, a boundary condition at the wall is necessary to close the problem as fluid properties at the wall are required. A radiation, adiabatic wall condition was assumed. This implies that the wall temperature is not fixed, but the heat flux through the wall is zero (i.e. the heat transfer to the wall from the fluid due to conduction and diffusion must equal the heat transfer radiated away from the surface.) Mathematically this is shown with Eq. (22).

$$\dot{q}_r = \dot{q}_d + \dot{q}_c = \dot{q}_w \tag{22}$$

where,

$$\dot{q}_r = \epsilon \sigma T_w^4 \tag{23}$$

Here, $\dot{q}_d$ is the heat transfer due to diffusion, $\dot{q}_c$ is the heat transfer due to conduction, ϵ is the wall emissivity and σ is the Stefan-Boltzmann constant. Note that the heat transfer due to the radiation from the shock layer has been neglected, which is valid for the maximum temperature in the shock layer for this problem ($\sim$6000 K) resulting from the selected free stream parameters and vehicle dimensions. For given free stream conditions, the flow properties behind the standing bow shock along the stagnation streamline can be calculated using an equilibrium shock calculation procedure outlined in Anderson [37]. It can be assumed that the properties directly behind the shock are the properties on the edge of the boundary layer. The boundary layer edge viscosity is calculated using Sutherlands law. The pressure at the wall can be assumed to be the pressure at the boundary layer edge. Finally, the last step is to find the remaining properties at the wall; however, these are unknown because wall temperature is not specified. This requires then that Eqs. (19) and (22) be solved simultaneously with the system being implicitly dependent on the

wall enthalpy (found using high temperature equilibrium polynomial curve fits from Tannehill et al. [38]), wall viscosity (from Sutherlands Law) and the wall density (from the equation of state.) A simple root finding method can be implemented to resolve the system. The solution of the system then gives the radiative, adiabatic wall temperature at which the convective heat flux to the wall is radiated away from the surface.

For the above model problem, 11 variables were selected as sources of uncertainty. Both epistemic (model form) and aleatory (inherent) forms of uncertainty were considered. The epistemic uncertain variables were as follows: Lewis number, Prandtl number, boundary layer edge viscosity, emissivity, the heats of formation for nitrogen and oxygen and the power over the Lewis number. These model variables are considered as epistemic by imposing uncertainty on them due lack of knowledge. Note that uncertainty in the two heats of formation and the boundary layer edge viscosity were modeled through the introduction of a factor, k, to each variable, which was used to represent a variation in the uncertain variable (e.g. $x = k(x_{ref})$.) The factor k for each variable was treated as an epistemic uncertain variable.

The other four variables were treated as aleatory (inherent) uncertain variables: free stream velocity, free stream density, free stream temperature and the radius of curvature of the body. Random fluctuations in the free-stream conditions are possible during flight and variations in the vehicle geometry are possible due to manufacturing processes. These variables were assumed normally distributed about some mean with a coefficient of variance (CoV) of 1%. The uncertainty bounds of the seven epistemic uncertain variables and the input uncertainties for the four aleatory uncertainty variables are summarized in Table 6.1.

12 samples were taken from the deterministic model using Latin Hypercube (LHS) sampling. With only 12 samples, it is not possible to carry out the UQ analysis

Table 6.1. Uncertain Parameter Information

Input	Distribution	Lower Bound/ Mean	Upper Bound/ CoV
Le	Epistemic	1.358	1.442
Pr	Epistemic	0.679	0.721
μ_e Factor	Epistemic	0.97	1.03
ϵ	Epistemic	0.776	0.824
h_f^0 (N) Factor	Epistemic	0.97	1.03
h_f^0 (O) Factor	Epistemic	0.97	1.03
U_∞, m/s	Gaussian	7315.2	1%
ρ_∞, kg/m^3	Gaussian	5.30E-05	1%
T_∞, K	Gaussian	212.01	1%
R_n, m	Gaussian	0.3048	1%

directly as a problem with 11 uncertain variables requires a minimum of 78 function evaluations for a 2nd order polynomial chaos expansion (see Eq. (2)).

After generating the samples, the next step is to perform local SA to obtain the G_i, or the approximation to global sensitivity for each uncertain variable. Using the 12 samples, a total of 132 additional deterministic code evaluations are necessary. The G_i values are shown in Figure 6.2. Also in this figure, a comparison is made to Sobol Indices which give the global, nonlinear sensitivities obtained from the polynomial chaos expansion. Because Sobol Indices require an accurate PCE, it is not provided as part of the multi-step UQ process since obtaining an accurate expansion may not be possible before dimension reduction. It may, however, be desirable to obtain the Sobol Indices for the reduced problem after the final PCE is constructed to acquire the most accurate estimate of the contribution of each variable to the total output variance. In this test case, it was possible to obtain an accurate PCE as Eq. (2) reveals that there are only 78 output modes, indicating that the system in Eq. (7) can be solved with an over sampling ratio of about two for a 2nd order PCE. This allows for the calculation of accurate Sobol indices for comparison to the G_i. As

can be seen from Figure 6.2, G_i values compare well to the Sobol indices. The slight difference between the G_i and Sobol Indices results from the G_i not accounting for the interaction between uncertain parameters and the approximation of using an average of multiple local sensitivity values in a nonlinear design space as achieved by using Sobol indices. However, when the sample size is not large enough to determine the Sobol indices, this approximation is shown to be a sufficient approximation to the contribution of each variable to the total output variance.

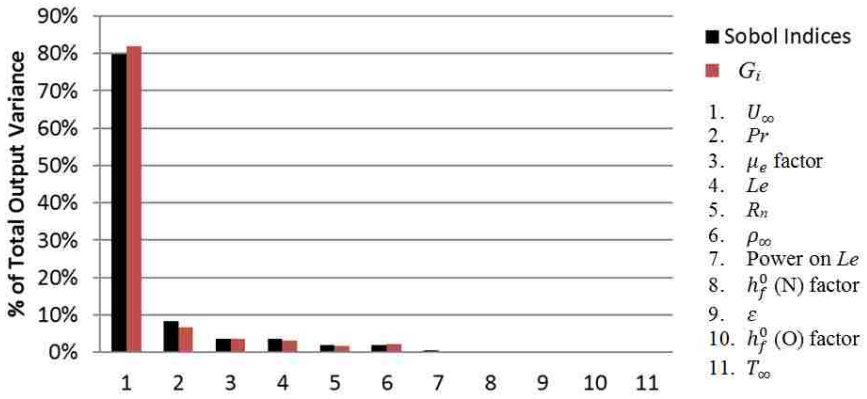

Figure 6.2. Sobol Indices (2^{nd} Order PCE) and G_i (12 Initial Samples)

The next step of the multi-step UQ process is to reduce the dimensions of the original problem. This was done for two different scenarios based on the G_i results. In the first, the problem was reduced from the full 11 variable problem to six variables. In the next scenario, the problem was reduced, again, from the full 11 variable problem, but down to only two variables.

Case 1: Dimension Reduction from 11 to 6 Variables

From the results shown in Figure 6.2, the first six variables (free stream velocity, Prandtl number, boundary layer edge viscosity factor, Lewis number, body radius of curvature, and free stream density) account for 99% of the total uncertainty. Reducing

the problem to six variables reduces the number of terms in the PCE from 78 to 28 for a 2nd order PCE. Using the modification scheme in Eq. (18), the number of available equations in the system in Eq. (7) drops from 144 to 84, as the sensitivities equations for the neglected variables are not included. The p-box results of the second-order probability for the reduced NIPC problem are shown in Figure 6.3, compared to the Monte Carlo simulation of the original problem (i.e. 11 uncertain variables). Associated probability levels are shown in Table 6.2. Notice that there is only a slight change from the full 11 variable problem results. This is because these six variables account for 99% of the uncertainty and the five neglected variables had little influence on the total uncertainty. For this problem the 95% confidence interval is then obtained as [73.73, 89.87] W/cm^2 for the NIPC analysis and [73.51, 89.69] W/cm^2 for the Monte Carlo analysis.

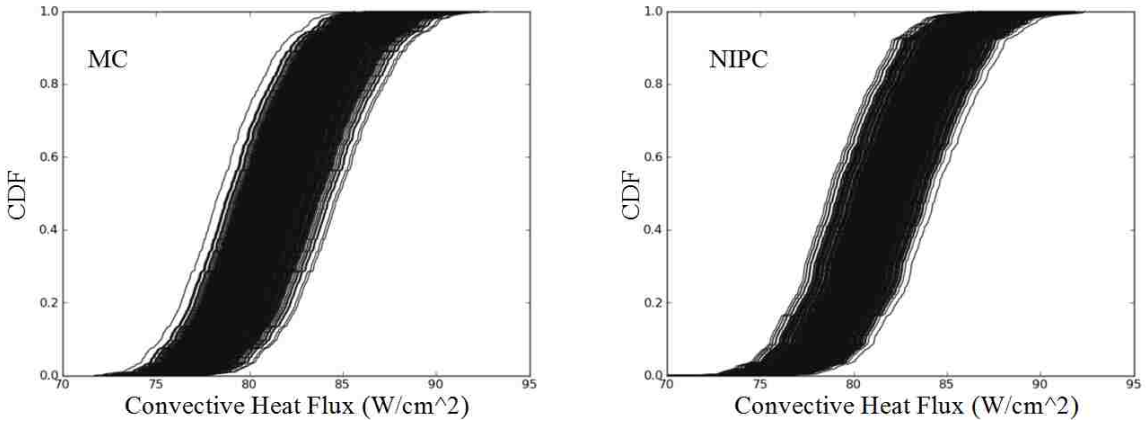

Figure 6.3. P-box plots for Mixed Uncertainty Analysis: 11 Variable Monte Carlo vs. 6 Variable 2nd order PCE

Case 2: Dimension Reduction from 11 to 2 Variables

Using the results from Figure 6.2, it can be seen that the first two variables (Free-Stream Velocity and the Prandtl Number) account for about 88% of the total uncertainty. Reducing the problem to two variables reduces the number of terms

Table 6.2. Stagnation Point, Convective Heat Transfer (W/cm^2) Probability Level Intervals for Figure 6.3

Probability Level	**Monte Carlo, 11 Variables**	**2nd Prder PCE, 6 Variables**
2.5%	[73.51 , 79.23]	[73.73 , 79.16]
50%	[78.34 , 84.46]	[78.65 , 84.45]
97.5%	[83.16 , 89.69]	[83.71 , 89.87]

in the PCE from 78 to 6 for a 2nd order PCE. Using the modification scheme in Eq. (18), the number of available equations drops from 144 to 36, as the sensitivity equations for the neglected variables are not included. The p-box results of the second order probability analysis for the two variable NIPC problem are shown in Figure 6.4, compared to the 11 variable Monte Carlo simulation. Associated probability levels are shown in Table 6.3. There is a noticeable difference in the results between the NIPC and the Monte Carlo simulation. This is expected because about 12% of the original uncertainty is no longer being accounted for, explaining the decrease in the width of the probability box in Figure 6.4. (Note that in this problem, it is possible to generate a 3rd order expansion given the number of remaining samples and sensitivities. However, depending on the size of the problem, this may not always be an option without additional sampling of the deterministic model in the reduced dimension. Higher order expansions may be necessary if the accuracy of the stochastic response surface is not at a desired level.) For some design cases, accounting for this amount of uncertainty may be acceptable as this may outweigh the time or ability to obtain additional samples to account for more uncertainty. For this problem, the 95% confidence interval is then obtained as [75.42, 88.09] W/cm^2 for the NIPC analysis and [73.51, 89.69] W/cm^2 for the Monte Carlo analysis.

Table 6.3. Stagnation Point, Convective Heat Transfer (W/cm^2) Probability Level Intervals for Figure 6.3

Probability Level	**Monte Carlo, 11 Variables**	**2nd Prder PCE, 2 Variables**
2.5%	[73.51 , 79.23]	[75.42 , 78.06]
50%	[78.34 , 84.46]	[80.27 , 83.07]
97.5%	[83.16 , 89.69]	[85.12 , 88.09]

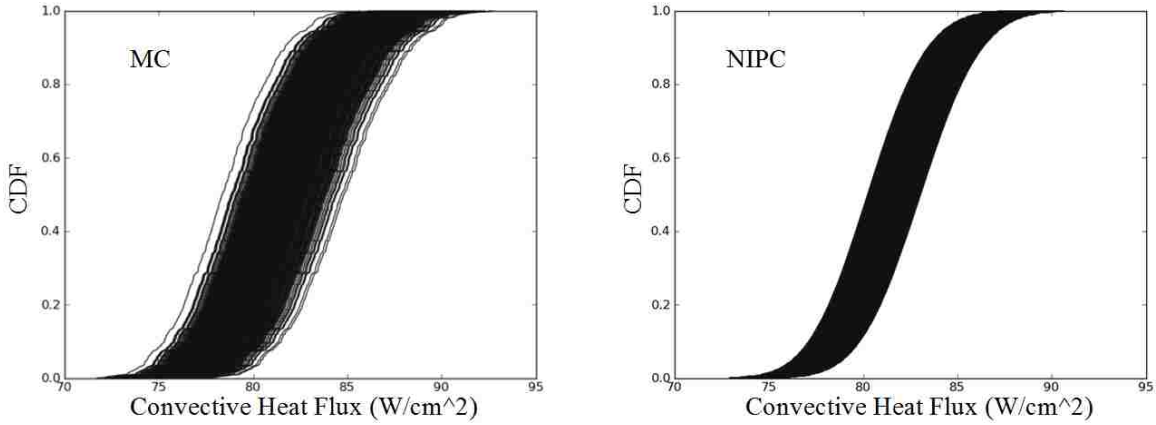

Figure 6.4. P-box plots for Mixed Uncertainty Analysis: 11 Variable Monte Carlo vs. 2 Variable 2nd order PCE

Previous work by Witteveen and Bijl [30] have shown that it may be possible to add back the uncertainty not accounted for after dimension reduction through the use of sensitivity information. The presented approach was to develop a linear estimate of the uncertainty not accounted for and add it to the problem with reduced dimensions. Since the sensitivity information for all the variables is already determined as part of the current multi-step UQ process, that approach, while not applied in the present work, may also be considered to approximate the uncertainty in the output due to the uncertain variables that not accounted for in the reduced dimension.

Since a significant amount of the uncertainty has been ignored in this scenario, it is necessary to measure the accuracy of the sample modification scheme described in Eq. (18). Table 6.4 shows the 12 original sample values, the outcome after modification, followed by the actual sample values if the code was analyzed using only the two uncertain variables of interest at the same sample points (the other variables at their respective nominal value.) Notice that the error is extremely small, indicating that the modification scheme is an accurate tool for dimension reduction problems.

Table 6.4. Comparison of Updated Sample Heat Flux Values with Actual Sample Values for the Two Variable Problem (W/cm^2)

Original	**Modified**	**Actual**	**% Error**
84.3473	84.7261	84.7043	0.0258
81.8917	80.3461	80.3543	0.0102
83.9082	83.2516	83.2253	0.0315
77.1334	78.1108	78.1045	0.0081
79.4474	80.7777	80.7924	0.0182
82.7980	81.4752	81.4982	0.0281
82.9207	82.9542	82.9193	0.0420
84.8559	85.8026	85.7952	0.0085
78.5117	78.2335	78.2187	0.0189
79.8163	80.7458	80.7561	0.0127
79.0190	79.1076	79.1007	0.0088
83.9843	83.7741	83.7684	0.0068

6.2.2. High-Fidelity Radiative Heat Flux Prediction during Mars Entry. In this model problem, taken from Johnston et al. [39], the flow field was modeled using the LAURA finite-volume, Navier-Stokes flow solver [40]. The solver uses a second order upwind discretization scheme with relaxation of both inviscid and viscous terms for solution stability. The flow field, assumed to be steady state, was

modeled using a two-temperature, thermochemical nonequilibrium model with a 17 species composition: CO_2, CO, N_2, O_2, NO, C, N, O, CN, C_2, C^+, O^+, CO^+, O_2^+, NO^+, CN^+, and e^-. The radiation was modeled using the HARA nonequilibrium radiation code [41, 42]. The details regarding the radiation modeling approach and parameters are given by Johnston et al. [39] as the same modeling approach was used. Note here that the flow field solver and the radiative heat transfer calculations are coupled.

The radiation in this problem is modeled for flow over a generic HIAD configuration. This geometry is modeled with a 70 degree spherical cone with a nose radius of 3.75 m, a shoulder radius of 0.375 m, and a base radius of 7.5 m. The computational grid used for this geometry was 128x48 and is shown in Figure 6.5. Notice in this figure the clustering of the grid in the flow field. Previous study have shown that a significant portion of the radiation emitted from the shock layer comes from a strong non-equilibrium region near the shock [39]. Because of this, accurately capturing the flow field properties and quantities near the shock is important. LAURA uses a gradient based shock capturing technique to detect and cluster the grid in the flow direction, near the shock location.

For the boundary conditions, the free stream was comprised of 96% CO_2 and 4% N_2, by mole, at 150 K with a density of 1.0e-4 kg/m^3. The velocity was taken to be 7.0 km/s to simulate a high speed Mars reentry, with 0 degrees angle of attack. The wall of the HIAD was modeled as a super-catalytic wall with a constant temperature of 1500 K.

6.3. DESCRIPTION OF THE STOCHASTIC PROBLEM

In this model problem, a total of 93 uncertain parameters were treated as part of the UQ analysis. The uncertainty in this problem comes from two primary sources: uncertainty in the flow field modeling parameters and the uncertainty in the

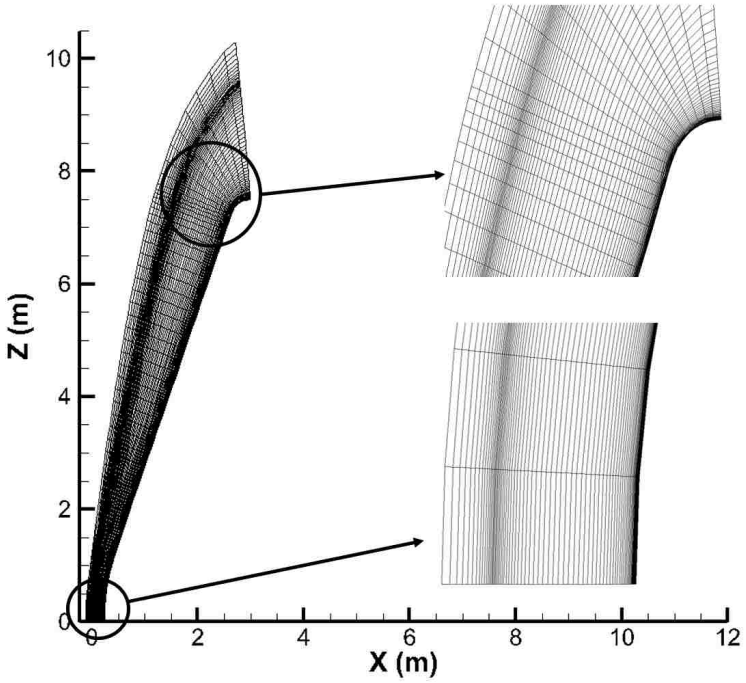

Figure 6.5. Computational Grid

radiation modeling parameters. Uncertainty in the flow field modeling parameters is primarily due to the uncertainty in the chemical kinetic rates. Because of the 17 species being treated in this problem, there are many chemical reactions taking place throughout the shock layer. Chemical rates can be difficult to accurately measure and model, making them a potentially significant source of uncertainty. In this analysis, 20 chemical kinetic rates are treated as uncertain input parameters. A list of the chemical reactions, their baseline rate parameters (of an Arrhenius form), and the input uncertainty are given in Table A1 of the Appendix.

The second source of uncertainty is due to the radiation modeling parameters. This is further broken down into two groups. The first is the uncertainty in the spectrum modeling. In this study, 16 molecular band processes are treated as uncertain. The molecular band information and associated uncertainty in the

oscillator strengths of these bands are given in Table A2 in the appendix. The second group of radiation modeling parameters with uncertainty are those parameters associated with the non-Boltzmann modeling of the radiating atomic and molecular states. Similar to the chemical kinetics, the treatment of the collisional processes for non-Boltzmann modeling can be a significant source of uncertainty due to the difficulty in obtaining accurate impact excitation rates for both heavy particle impacts and electron excitation impacts. Tables A3 and A4, in the Appendix, give the reactions, their baseline rate parameters (of an Arrhenius form), and the input uncertainty for 35 electron-impact excitation rates and 22 heavy particle impact excitation rates, respectively.

The details regarding the selection of the uncertainty parameters, their associated uncertainty, and the specifics of the radiation modeling, in particular the non-Boltzmann modeling can be found in Johnston et al. [39], which is the foundation of this stochastic model problem.

The multi-step UQ was applied to this stochastic problem for two different scenarios: (1) the reduction from 93 to 10 variables and (2) the reduction from 93 to 5 variables. An initial sample size of 20 was used for the local SA. The sampling method used, as in the previous problem, was Latin Hypercube (LHS) sampling. (Note that with only 20 samples, it is not possible to carry out the UQ analysis directly as a problem with 93 uncertain variables requires a minimum of 4465 function evaluations for a 2^{nd} order polynomial chaos expansion, by Eq. (2). Further analysis is required.) The effect of the input uncertainty can be seen in Figure 6.6 which shows a scatter plot of the 20 samples and also a plot of the maximum and minimum wall-directed radiative heat flux along the stagnation line, though the shock layer obtained from this sample set. Of the 20 samples taken, notice that radiative heat flux at the wall ranges from about 6 W/cm^2 to nearly 22 W/cm^2 indicating the significance of the uncertain input parameters.

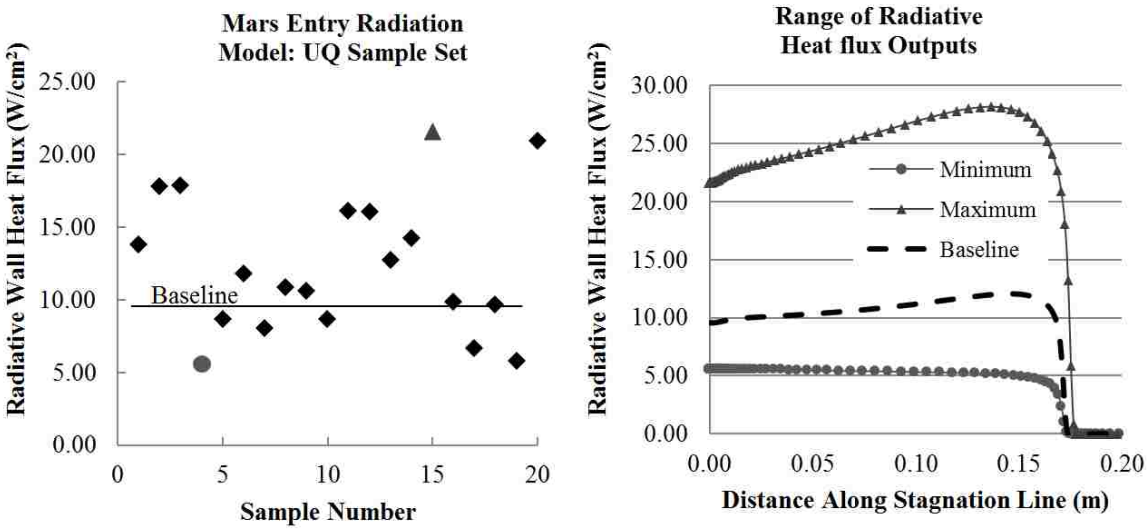

Figure 6.6. Effect of Input Uncertainty on the Flow field and Wall Radiation

In the multi-step UQ process, the next step is to perform the local SA and generate the G_i. One important aspect of this problem is that many of the uncertain variables have very wide uncertainty ranges; as much as two orders of magnitude. To have better approximations for the sensitivities and to create a more accurate NIPC response surface to be used in the UQ analysis, it is more appropriate to perform both of these analyses on a log scale when uncertainties with wide range are involved. A similar approach was followed by Hosder and Bettis [7]. In this analysis, many variables with an order of magnitude variation in the uncertainty were represented on a $\log_{10}$ scale. For example, this approach takes a variable with a ± 2 order of magnitude uncertainty range (0.01 to 100) and transforms it to a variable with a ± 2 uncertainty range (-2 to 2).

Implementing the use of variables on a $\log_{10}$ scale also requires some modification to the local sensitivity analysis methodologies. In Eq. (24), notice that the derivative with respect to the $\log_{10}$ of variable x_i can be expanded into two terms: the original sensitivity value and the derivative of variable x_i with respect to the $_{10}$ of variable x_i.

$$\frac{\partial F}{\partial \log_{10}(x_i)} = \frac{\partial F}{\partial x_i}\frac{\partial x_i}{\partial \log_{10}(x_i)} = \frac{\partial F}{\partial x_i}\ln(10)x_i \tag{24}$$

This logarithmically scaled local sensitivity value can then be used in Eq. (17), by simply replacing the standard sensitivity with the above logarithmic sensitivity and the range of the uncertain variable with the logarithmic range.

A total number of 1880 evaluations of the CFD model was required (20 sample points and 1860 sensitivities.) Figure 6.7 shows the variation in the sensitivity value across the design space for the most important input parameter. Notice that the sensitivity varies significantly in the uncertainty space (i.e., for each sample point) indicating the nonlinear behavior of the response with respect to this variable.

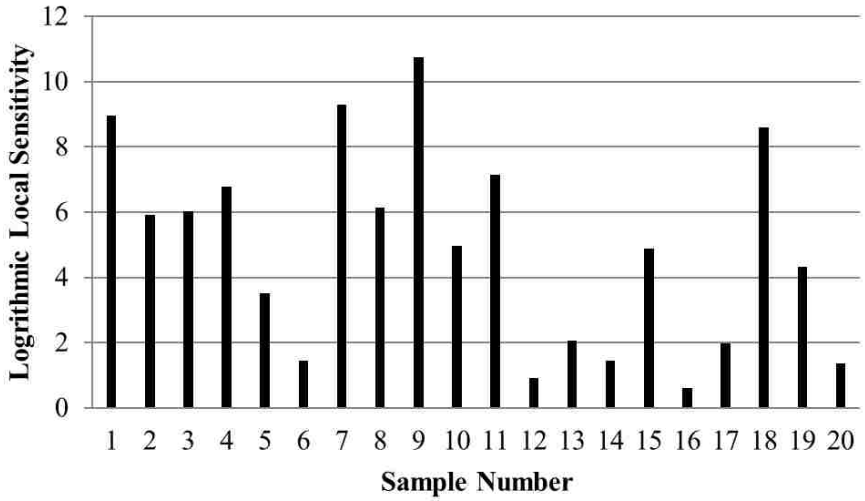

Figure 6.7. Sensitivity Values of the Most Contributing Random Variable

Figure 6.8 shows the results of the G_i values. Many of the variables have nearly zero contribution to the total output variance. This may be typical for problems with many uncertain variables, in that a small portion of the input parameters may dominate the amount of uncertainty. Note that here there is no

Sobol Indices comparison to the G_i values as in the previous model problem because the calculation of the Sobol Indices required a polynomial chaos expansion. With the high dimensionality of this problem, it is not feasible to perform a polynomial chaos expansion prior to dimension reduction.

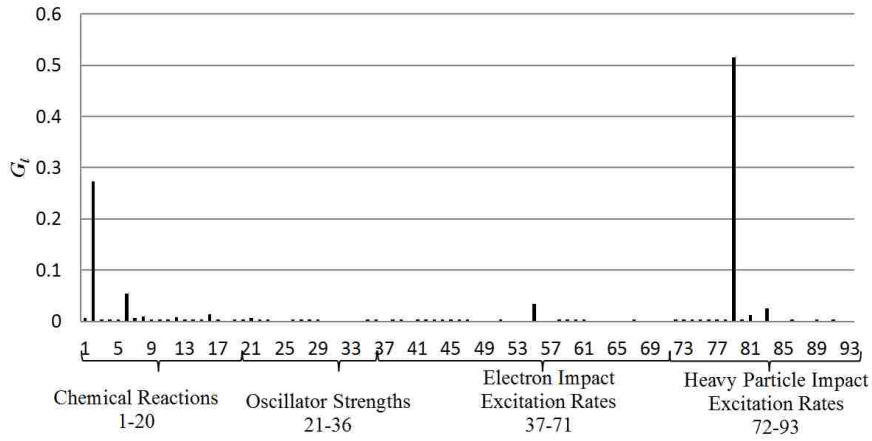

Figure 6.8. Gi Values for the Stagnation Point, Radiation Model

The next step in the multi-step UQ analysis is to reduce the dimension of the problem. From the G_i analysis results in Figure 6.8, 10 of the 93 uncertain variable account for approximately 95% of the total output variance. Further reduction shows that 5 of the 93 variables accounts for approximately 90% of the total output variance. The top ten uncertain parameters are given in Table 6.5 along with their percent of contribution to the total output variance. The top five uncertain parameters found in this study are consistent with the five most important variables found in the analysis performed by Johnston et al. [39]

Using the sample update scheme given in Eq. (18), the original 20 deterministic model evaluations were modified to make them independent of both the 83 and 88 variables neglected for dimension reduction to ten and five variables, respectively. Recall that for variables that are neglected, their sensitivities are also lost as the

Table 6.5. Top 10 Most Contribution Uncertain Parameters Based on the G_i Analysis

Rank	Reaction	Uncertainty Contribution	Category
1	$CO(X^1\Sigma^+) + M \leftrightarrow CO(A^1\Pi) + M$	51.6%	Heavy-Particle Impact Excitation Rate
2	$CO + M \leftrightarrow C + O + M$	27.3%	Flow Field Chemical Reaction Rate
3	$NO + M \leftrightarrow N + O + M$	5.5%	Flow Field Chemical Reaction Rate
4	$CO(a^3\Pi) + e^- \leftrightarrow CO(A^1\Pi) + e^-$	3.5%	Electron Impact Excitation Rate
5	$CO(e^3\Sigma^-) + M \leftrightarrow CO(A^1\Pi) + M$	2.5%	Heavy-Particle Impact Excitation Rate
6	$N + CO \leftrightarrow NO + C$	1.3%	Flow Field Chemical Reaction Rate
7	$CO(a'^3\Sigma^+) + M \leftrightarrow CO(d^3\Delta) + M$	1.3%	Heavy-Particle Impact Excitation Rate
8	$CO_2 + O \leftrightarrow O_2 + CO$	0.9%	Flow Field Chemical Reaction Rate
9	$CO + O \leftrightarrow O_2 + C$	0.9%	Flow Field Chemical Reaction Rate
10	$CO(A^1\Pi) \leftrightarrow CO(X^1\Sigma^+) h\nu$	0.8%	Molecular Band Process

model is no longer sensitive to those parameters. For the reduction of the uncertain variables to a total number of 10 variables, 200 sensitivities remain while for the 5 variable problem only 100 sensitivities remain.

The last step in multi-step UQ analysis is to formulate the response surface using the gradient-enhanced point-collocation scheme given in Eq. (7). For the ten variable problem, the response surface was analyzed using both a pure epistemic analysis as well as pure aleatory analysis. A pure epistemic analysis has no probability associated with the output. This is basically the case that gives the absolute maximum and minimum response values. These values are given in Table 6.6. A pure aleatory analysis is a probabilistic analysis. This method assumes that all of the input parameters have a probabilistic uncertainty distribution. For this analysis, it was assumed that all of the input parameters were uniformly distributed over the intervals given for each parameter in the appendix. The response values at different probability levels are given in Table 6.7. The output cumulative distribution function (CDF) curve is also shown in Figure 6.9, along with the epistemic boundaries. Note how the epistemic values bound the aleatory analysis curve. This is expected, given that the epistemic outputs come from the bounds of the response for the considered input uncertainty range.

Table 6.6. Reduced Dimension Epistemic Intervals

5 Variables	[1.98 , 28.65] W/cm^2
10 Variables	[0.54 , 24.49] W/cm^2

Table 6.7. Reduced Dimension Pure Aleatory Analysis, Selected Probability Level Values

Probability Level	**5 Variables (W/cm^2)**	**10 Variables (W/cm^2)**
2.50%	4.66 W/cm^2	4.08
25.00%	8.22 W/cm^2	7.81
50.00%	10.86 W/cm^2	10.52
75.00%	13.98 W/cm^2	13.74
97.50%	20.47 W/cm^2	20.52

From Figure 6.9, the five variable problem lies inside the ten variable problem. As seen in the previous model problem, with an increase in the amount of uncertainty neglected during the dimension reduction process, there is a reduction in the uncertainty range of the output response.

For a pure aleatory analysis, a 95% confidence interval can be calculated by taking the interval between the 2.5% probability level and 97.5% probability level value. For the ten variable problem this interval is [4.08, 20.52] W/cm^2, where, for the five variable, the 95% confidence interval is [4.66, 20.47] W/cm^2. As with the epistemic analysis, notice the slight decrease in the interval for the five variable case due to neglecting additional uncertain variables.

A third analysis was performed on the reduced, five variable problem assuming the contribution of both aleatory and epistemic input parameters. In this mixed uncertainty analysis, the two remaining flow field chemical kinetic rates were assumed

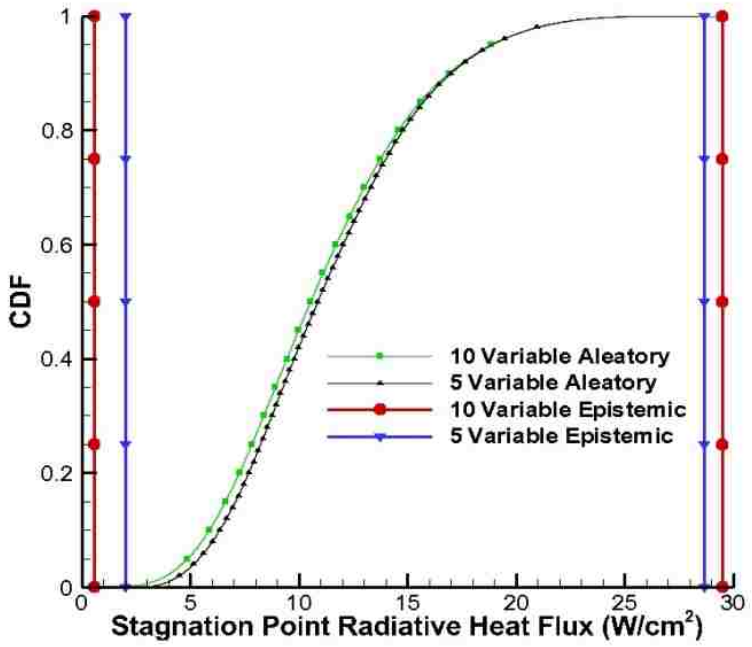

Figure 6.9. Pure Aleatory and Epistemic Analysis Probability Box

to have a uniform probability distribution and the three remaining radiation modeling parameters were considered as epistemic uncertain variables. The resulting output response at selected probability levels is given in Table 6.8, and the p-box plot is given in Figure 6.10. Note that the epistemic boundaries given back in Table 6.6 for the five variable problem still bound the results of the mixed uncertainty analysis as this, again, gives the most conservative uncertainty in the output. As done in the pure aleatory analysis, a 95% confidence interval can also be defined for the mixed uncertainty output. One approach to calculate the 95% confidence interval for this case is taking the smallest value of the 2.5% probability interval and the largest value of 97.5% probability level. For this problem the 95% confidence interval is then obtained as [2.24, 25.68] W/cm^2.

The results of all the above analyses are summarized in Table 6.9. Compared to the results obtained by Johnston et al. [39], the results of this study are consistent

Table 6.8. Mixed Uncertainty Analysis, Selected Probability Level Values

Probability Level	**5 Variables(W/cm^2)**
2.50%	[2.24 , 15.08]
25.00%	[2.82 , 16.33]
50.00%	[3.14 , 18.29]
75.00%	[4.55 , 21.11]
97.50%	[7.28 , 25.68]

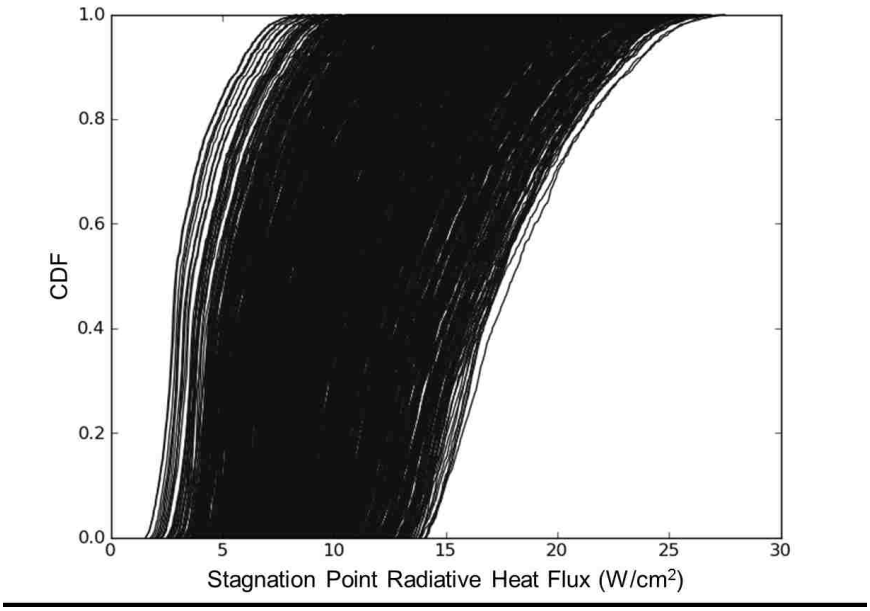

Figure 6.10. Mixed Uncertainty Analysis Probability Box (5 Variables).

given the differences in the uncertainty quantification techniques. Overall, the multi-step UQ approach has been shown to be a powerful tool when quantifying the uncertainty of complex reentry flow simulations. Accurate ranking of the uncertain parameters was achieved with the proposed global sensitivity approximation and a computationally efficient UQ analysis was performed for pure epistemic, pure probabilistic, and mixed input uncertainty cases. The multi-step UQ analysis also

provided valuable information on the ranking of important variables in terms of their contribution to the output uncertainty, which might allow for an increased focus on developing more accurate uncertainty representations on these significant variables.

Table 6.9. Reduced Dimension Epistemic Intervals

Analysis	**Difference from Baseline**
10 Variable Aleatory (95% C.I.)	-57% , +115%
10 Variable Epistemic	-94% , +209%
5 Variable Aleatory (95% C.I.)	-51% , +114%
5 Variable Epistemic (95% C.I.)	-79% , +200%
5 Variable Miked (95% C.I.)	-77% , +169%

As a final check of the validity of the results, the accuracy of the polynomial chaos model can be conducted. A check was performed by generating 20 new Latin Hypercube samples of the CFD model for the reduced, 5 variable problem and comparing them with outputs from the reduced dimension polynomial chaos expansion at the same sample locations. The root-mean-square error between the CFD solution and the surrogate model was determined to be approximately 10%. This level of error was perceived as acceptable considering the range of output uncertainties obtained and the approximations made in the multi-step UQ process (first-order finite difference and first-order sample correction method) as well as any uncertainties associated with the numerical solution of the deterministic CFD simulations (e.g., discretization errors).

7. SPARSE APPROXIMATIONS OF STOCHASTIC EXPANSIONS

As discussed in previous sections, polynomial chaos techniques suffer from the "curse of dimensionality" meaning that the number of deterministic model evaluations required to create an accurate surrogate model grows exponentially with the number of random dimensions. For many large-scale, complex problems, generating even the minimum number of deterministic model samples may be infeasible or even impossible simply due to the computational cost. The desired approach is to obtain an accurate surrogate model with as few deterministic samples as possible to limit the computational cost, even if the minimum number of samples required for a total order expansion is not achievable. This section outlines an approach for a sparse approximation of the polynomial chaos expansion, including a discussion of accuracy and convergence. The approach is then applied to three hypersonic, planetary entry flow problems.

7.1. SPARSE APPROXIMATION METHODOLOGY

In general, a system of linear equations that has fewer linearly independent equations than unknowns, possesses an infinite number of solutions. In many PCEs, only a small fraction of the coefficients may carry significant weight in the surrogate model and/or are near zero. This would then allow for an assumption that many of the expansion coefficients are zero, making the vector of expansion coefficients sparse. With this assumption, the linear system can be regularized allowing for a well-posed solution. The objective is to seek out a solution to the linear system with the fewest number of non-zero coefficients. Using convex relaxation, a solution can be obtained from the L_1-minimization problem shown in Eq. (25).

$$\min \left\| \alpha \right\|_1 \text{ subject to } \left\| \Psi\alpha - \alpha^* \right\|_2 \leq \delta \tag{25}$$

Here, δ is the truncation error associated with the truncation of the series in Eq. (1). For the problems in this study, δ is assumed equal to zero, as it can be shown that the solution to Eq. (25) is unique in this instance. In the above formulation, the dimensions of Ψ are N_s x N_t and the vector α^* is of length N_s where $N_s < N_t$ for the underdetermined problem. The vector α is of length N_t. Doostan and Owhadi [14] discuss, in great detail, the theory and formulation of the above method, as well as discussion on stability.

The optimization problem in Eq. (25) is commonly referred to as Basis Pursuit Denoising (BPDN) [14, 43, 44]. This type of problem can be solved using many methods from quadratic programming, and the discussion of these methods is left to other works [43, 44]. In the current study, the least absolute shrinkage and selection operator (LASSO) homotopy optimization routine [44] was selected to find the optimal solution of Eq. (25). While many methods exist for solving the above minimization problem, the homotopy method was selected for efficiency, as this method is not significantly affected by the dimensionality of the problem [43].

7.2. SAMPLE SIZE, ACCURACY, AND CONVERGENCE

The optimization and sparse solution recovery approach poses two fundamental issues: (1) how to determine the necessary number of samples, N_s, required to obtain an accurate solution and (2) how to measure the accuracy of the solution. The latter of these assumes, of course, that no other means of obtaining the exact solution is possible, thereby relying on the solution obtained from Eq. (25). To reduce the computational cost, the desired approach is to limit the total number of deterministic model evaluations. To address both the sample size and the accuracy issues simultaneously, there must be a measure of the convergence of the expansion

coefficients with increasing sample size. The objective of this section is to outline a procedure for determining an acceptable sample size along with measuring the convergence of the stochastic expansion coefficients.

The first step in this process will be to generate an initial sample set of the random variables. The size of this initial sample set, generated using Latin Hypercube sampling, is taken as the size, N_t, given by Eq. (2) as this would be the minimum number of samples required to obtain a total order expansion. Note that generating large sample sets of the uncertain parameters is not computationally expensive compared to the cost of evaluating the deterministic model. The idea is to start with a small subset of the initial sample structure and evaluate the deterministic model at these points. Then, a first set of PCE coefficients can be obtained using the minimization routine in Eq. (25). This process is then repeated by iteratively adding more samples to the solution procedure (i.e., addition of new subsets of the full sample structure) until the convergence of the expansion coefficients is achieved. Note that each subset of the full sample structure added at each iteration should not contain any repeated sample vectors from the previous iterations. This would not provide any new information in recovering new solutions at each iteration.

After the expansion coefficients are approximated, their convergence should be checked at each iteration. In theory, this could be done by monitoring each individual coefficient. Unfortunately, for large scale problems, there may be thousands of coefficients. Also, because the expansion coefficient vector is known to be sparse, this may not be an accurate approach as the degree of sparseness of the solution vector may decrease with increasing sample size causing radical changes in any convergence error measurement. A logical choice for a convergence metric would be to use output statistics based on the expansion coefficients. One metric that could be used is the Sobol indices outlined in Section 5.1.

Recall that the accuracy of the Sobol indices depend on the accuracy of the expansion coefficients, making it an ideal measure of their convergence. Also, because the number of total Sobol indices is the same as the number of uncertain parameters, there will be less parameters to track as this number will always be less than the number of expansion coefficients. To monitor the convergence of the total Sobol indices with the addition of more samples at each iteration, an absolute error, $S_{e_{i,j}}$ can be defined for the j^{th} total Sobol index at iteration i using Eq. (26).

$$S_{e_{i,j}} = \left\| S_{T,i,j} - S_{T,i-1,j} \right\| \tag{26}$$

Note that measuring the convergence based on this absolute error puts emphasis on the variables that contribute to the output uncertainty more significantly. The errors of each total Sobol index, at each iteration, can then be averaged giving a single value for monitoring, which is shown in Eq. (27).

$$\mu_{e,i} = \frac{1}{n} \sum_{j=1}^{n} S_{e_{i,j}} \tag{27}$$

Plotting this average error at each iteration would then illustrate the convergence of the PCE coefficients. The objective will be to seek out nearly asymptotic convergence, as zero error would likely not be achievable simply due to the randomness of the samples added at each iteration and any numerical inaccuracies that may occur during the analysis of complex models.

The second approach to measure the convergence of the PCE coefficients is to compare response values from the PCE to a set of sample points obtained from the design space, separate from the surrogate model training samples. The objective is to measure the error between response values from the polynomial approximation and the actual response at the test sample locations. In this study, test points are distributed throughout the design space using a Latin Hypercube sample structure.

This has the advantage of improving the coverage of the design space when a small sample set is used. Note that each test point used to measure the accuracy of the surrogate model does require an additional evaluation of the deterministic model to obtain the exact functional value. These test points could be rolled into the sample set used to approximate the surrogate. This could improve the accuracy of the model as more samples are included in the solution recovery. The magnitude of improvement will depend on the convergence (i.e., the accuracy of the model at the current iteration) and the number of test points used. The error between the points, $T_{e,i}$, may be estimated by the empirical error defined by Eq. (28) [45].

$$T_{e,i} = \frac{1}{N_{TP}} \sum_{j=1}^{N_{TP}} (F_{surr.}(\mathbf{x_j}) - F_{actual}(\mathbf{x_j}))^2 \tag{28}$$

Here, N_{TP} is the number of test points, $F_{surr.}$ is the response value from the PCE surrogate model, and F_{actual} is the actual test point value from the design space. The error between the surrogate and the deterministic model, at each test point, is an indication of the local accuracy of the surrogate model. Maximizing the number of test points will provide better coverage in the design space and would provide the best indication of the accuracy of the surrogate. Again, however, this does come at the cost of additional evaluations of the deterministic model.

7.3. DEMONSTRATION OF THE SPARSE APPROXIMATION APPROACH

To demonstrate the applicability and capabilities of the sparse approximation approach for the creation of a stochastic surrogate (i.e., PCE), three model problems are investigated. The first two problems are the same as the ones used to demonstrate the multi-step approach in Section 6.2. Comparisons between the two methods are made in this section. The third problem is high-fidelity model for the prediction of radiative heat transfer on the surface of a vehicle entering into Saturn's moon Titan,

which will be shown to have a unique radiative environment with a significant amount of uncertainty.

7.3.1. Stagnation-Point, Convective Heat Transfer in Hypersonic Flow. This problem was the same one used to demonstrate multi-step UQ in Section 6.2.1 for the prediction of stagnation-point, convective heating on a blunt-body in hypersonic flow. The details of deterministic model and the stochastic problem are given in the previous section.

To measure the convergence of the PCE coefficients using the sparse approximation approach outlined in this section, both the Sobol index and test point convergence approaches are employed. For the convergence of the Sobol indices, the first step is to generate the initial sample size. Section 6.2.1 showed that a second order expansion is sufficiently accurate for this model problem. From Eq. (2) the minimum number of samples required for a total order expansion is 78. For this problem, two samples were added at each iteration. The convergence of the mean Sobol index error calculated from Eq. (27), is shown in Figure 7.1(a) normalized by the maximum error value. Notice that there are large changes in the error at the beginning with a small sample size. As the sample size increases beyond approximately 30, the error tends to converge to a near zero value, asymptotically.

20 test points were generated in the uncertainty to measure the accuracy of the surrogate model. Note that these points were generated using a Latin Hypercube sampling of the uncertain parameters. The error between the test point values and the response values predicted by the PCE is measure using Eq. (28). The convergence of the test point empirical error, normalized by the maximum, is shown in Figure 7.1(a). Similar to the Sobol error convergence, notice that the error drops to near zero after about 20 samples. The convergence observed for both methods is indicative that the PCE coefficients are converged.

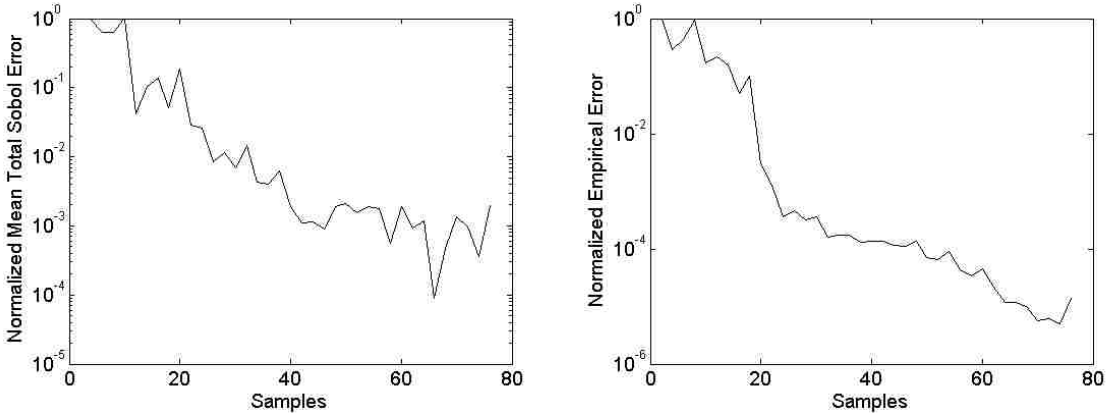

(a) Mean Total Sobol Error (b) Test Point Error

Figure 7.1. Convergence of the Sparse PCE for the Fay-Riddell Model

Since this problem is of smaller scale in terms of the number of uncertain variables, a least squares solution of the over determined system in Eq. (3) can be obtained for comparison without significant computational cost. In Figure 7.2, the Sobol indices at 30 and 50 samples are compared to those obtained from the least squares solution with an OSR of 2 which consists of 156 samples. Results obtained using an OSR of 2 were verified with Monte Carlo simulation in previous work by West et al. [33]. Notice that for even lesser sample sizes, the Sobol values are quite close to the values obtained from the least squares solution and the variable ranking is accurate. The accuracy of the Sobol index values is expect given the convergence shown in Figure 7.1(a).

A comparison of the output response at various probability levels can also be checked for convergence. Analyzing the response surface as described in Section 3 for mixed uncertainty at selected sample sizes provides the upper and lower CDFs which are shown in the P-box plot shown in Figure 7.3. The corresponding 95% confidence intervals values are shown in Table 7.1, which is measured as the distance between the lower bound of the 2.5% probability level and the upper bound of the 97.5% probability level. Notice that the 95% confidence interval converges rapidly. However,

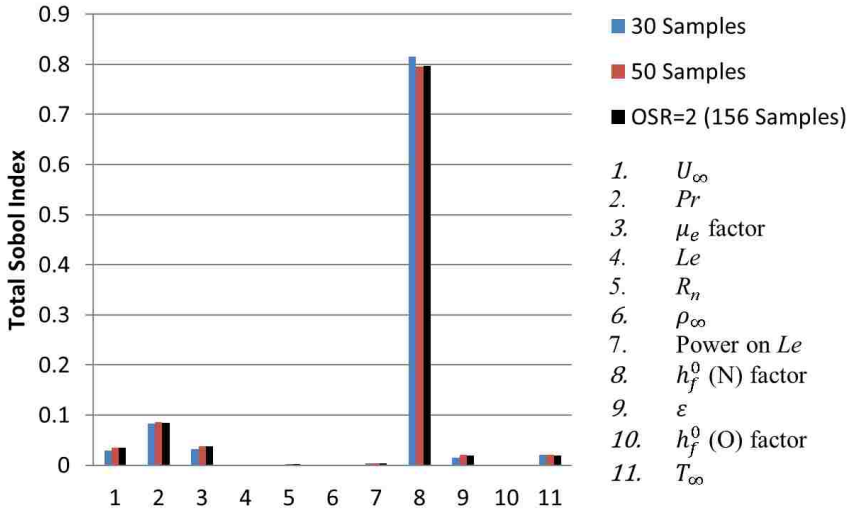

Figure 7.2. Total Sobol Index Values at Selected Sample Sizes

as can be seen for the sample size of 10, there is some degree of reduction in the output uncertainty. This is due to the lack of sufficient information required to construct the response surface that spans the actual response surface region. Increasing the sample size converges the expansion coefficients and forces the results to match with those obtained from a Monte Carlo simulation of this model problem. Overall, the sparse sampling approach is able to recover an accurate solution of the PCE coefficients using a sample size that is less than half what is normally required for a total order expansion given by Eq. (2).

7.3.2. Radiative Heat Flux Prediction during Mars Entry. This problem was the same one used to demonstrate multi-step UQ in Section 6.2.2 for the prediction radiative heat transfer on the surface of a hypersonic inflatable aerodynamics decelerator (HIAD) during entry into Mars. The details of deterministic model and the stochastic problem are given in the previous section.

With 93 uncertain parameters in this problem, construction of a surrogate model using polynomial chaos may not be feasible as the "curse of dimensionality" for PCEs requires that a minimum of 4465 evaluations of the CFD code are required for a second

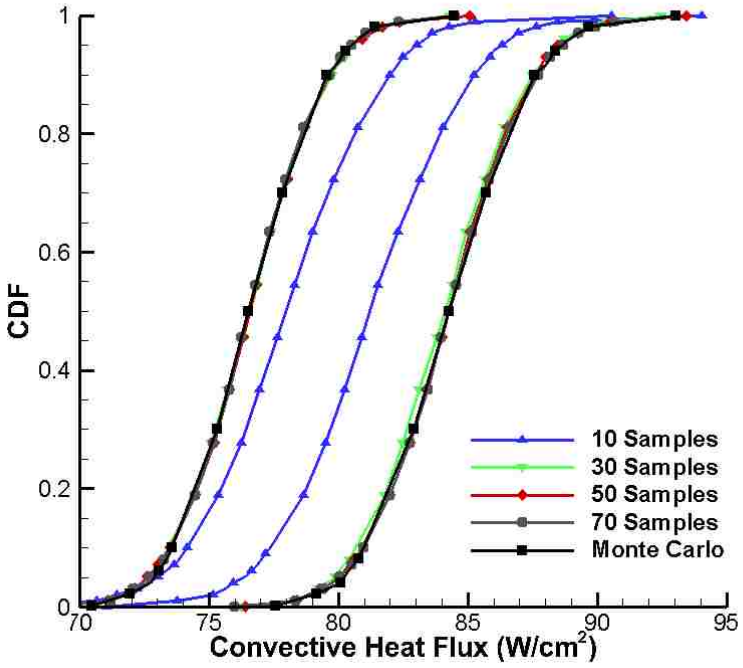

Figure 7.3. P-Box for Mixed Uncertainty Analysis at Selected Sample Sizes

Table 7.1. Output Intervals at Selected Probability Levels

Sample Size	**95% Confidence Interval (W/cm^2)**
10	[71.68 , 88.15]
30	[71.87 , 88.79]
50	[72.05 , 89.48]
70	[72.08 , 89.63]
400,000 (Monte Carlo)	[72.08 , 89.48]

order expansion. Given the complexity and time demand of the simulations, a Monte Carlo analysis is also not feasible as even more evaluations of the CFD code would likely be necessary to obtain accurate results. The ideal approach would be to only evaluate the CFD model enough times to construct an accurate surrogate model.

Here in lies the benefit of using a sparse sampling approach coupled with methods for checking convergence as the sample size increase.

The same analysis can be formed as was done in the previous model problem. First, to check the convergence of the Sobol indices, an initial sample set must be generated. In this model problem, the sample size was increased by 10 samples at each iteration. The convergence of the mean total Sobol error, normalized by the maximum, is shown in Figure 7.4(a). As with the previous model problem, there is a significant amount of error with small sample sizes. However, as the sample size increases, the error in the total Sobol indices drops rapidly and is less than about 5% with only 300 samples. This is significant given that 4465 samples are required to construct a total order expansion.

The convergence in the expansion coefficients can be also be checked by comparing test point values with those response values produced by the surrogate model at the same sample locations. For this model problem, 100 test points were generated. Using Eq. (28), the convergence of the error between the test point values is shown in Figure 7.4(b). Notice that there is a similar trend with the convergence of the total Sobol indices in that the error drops rapidly from the initial sample set and, by about 300 samples, has begun to show asymptotic convergence. The error for this convergence method is higher than that for the Sobol method. This is not unexpected as errors in the numerical solution of the CFD model may influence the test point comparison.

Additionally, the convergence of the total Sobol index values can also be checked. This is shown in Figure 7.5 for selected sample sizes. Notice that for a small sample size, the values are significantly different than those of the higher sample sizes. This is expected given the convergence results in the above figures. As the sample size increase, the accuracy of the total Sobol values increases. In this figure, the results are compared to previous work by West et al. [33] where a sensitivity analysis was

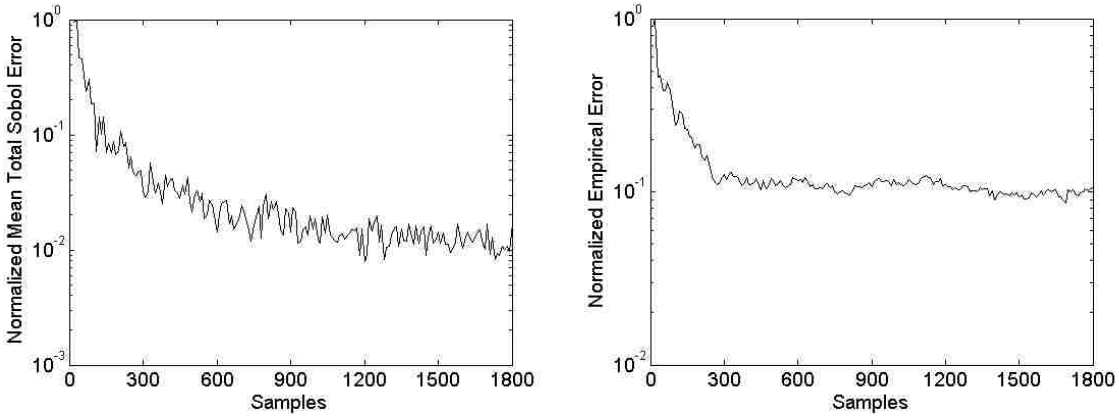

(a) Mean Total Sobol Error (b) Test Point Error

Figure 7.4. Convergence of the Sparse PCE for Mars Entry

performed for the same model problem. In the previous work, the global sensitivity values for each parameter were approximated using a series of local sensitivity values. Given the different between the two sensitivity methods, slight differences in the contribution of each uncertain parameter to the total output uncertainty are observed.

Another check of the most significant parameters and their total Sobol index values shows how quickly the correct ranking of the parameters is achieved. Figure 7.6 shows the convergence of the top five uncertain parameters, which account for over 90% of the total ouput uncertainty. Notice that the ranking is achieved with only about 100 samples. Additional samples make the Sobol indices converge as the PCE coefficient become more accurate.

After obtaining the expansion coefficients at each iteration, the response surface can be utilized for uncertainty quantification. Three different analyses were performed using the surrogate model at each iteration: a pure epistemic analysis, a pure aleatory analysis, and a mixed uncertainty analysis. For the pure epistemic analysis, an interval of the output can be obtained, which has no probabilistic interpretation. The convergence of this interval is shown in Figure 7.7. Notice that convergence of the epistemic interval takes longer to converge than what is reflected in the convergence

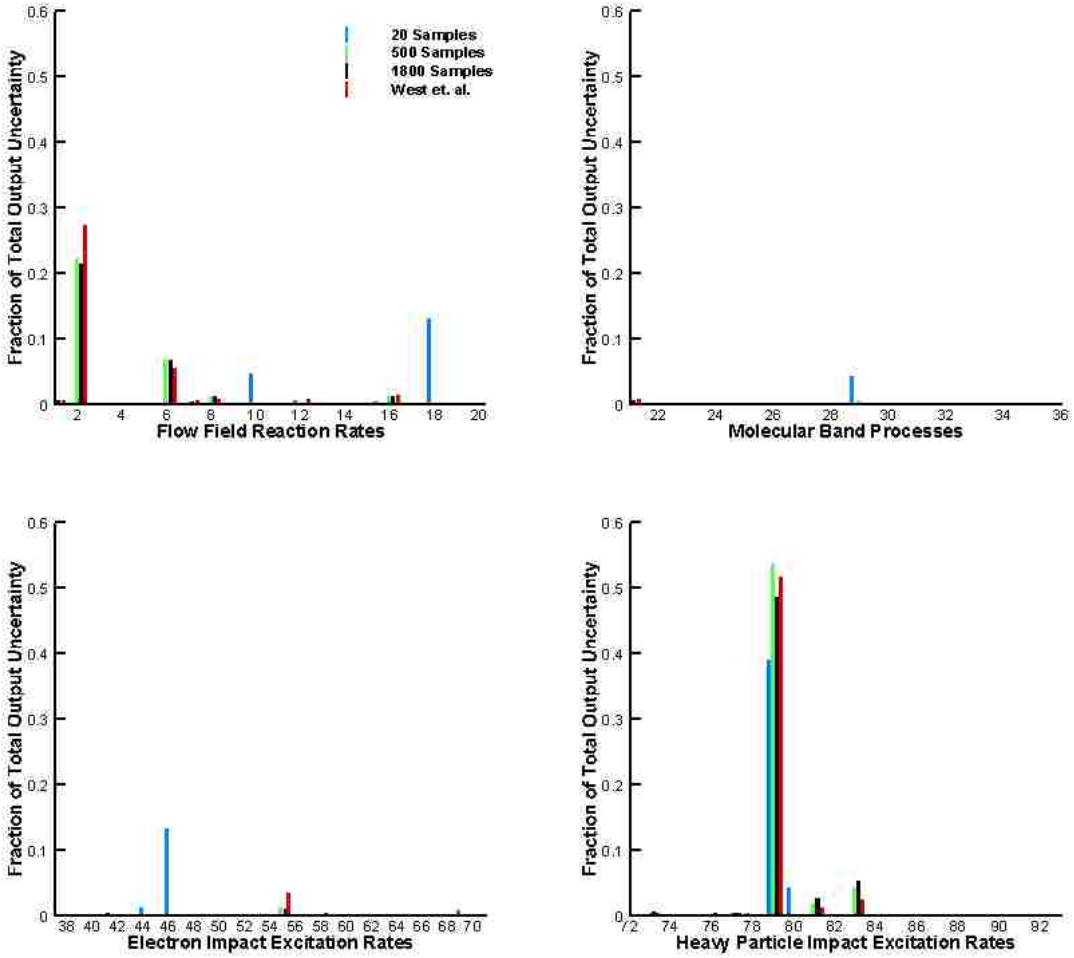

Figure 7.5. Fractions of Total Output Uncertainty at Selected Sample Sizes

metrics used for the PCE coefficients. This is because the epistemic interval is the very edges of the response surface. It is much more sensitive to the amount of information (i.e. the number of samples) used to construct the surrogate. Also note that the edges of the response surface may carry a small amount of uncertainty in itself simply due to the stochastic nature of the problem and the numerical error in the computational model. However, convergence is still observed with only about 600 samples.

A pure aleatory analysis was also performed. Here, all of the uncertain parameters were treated with uniform probability distributions as information about

each parameter is only known on an interval. The output of this analysis is a single CDF which provides a probabilistic view of the output. For this analysis the convergence of the 95% confidence interval can be tracked and is shown in Figure7.7. Note that the 95% confidence interval is measured between the 2.5% and 97.5% probability levels. This interval converges faster than the epistemic interval as it is not the far ends of the response surface. Additionally, the convergence of the mean of the PCE is also shown in this figure. The mean converges with a sample size less than 100 samples. This is expected as the first moment of the expansion is the easiest of the statistics to converge for a response surface.

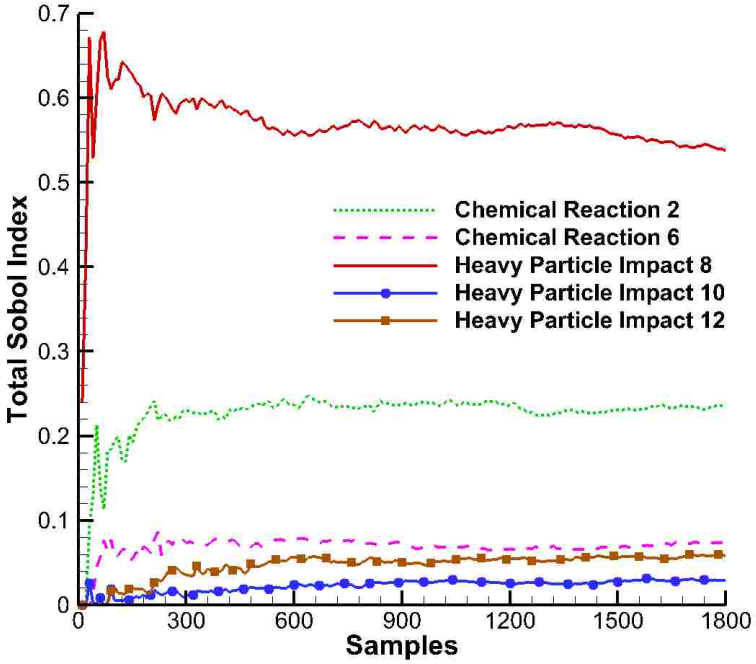

Figure 7.6. Convergence of Top 5 Uncertain Parameters at the Stagnation Point

A third, mixed uncertainty analysis was also performed. In this analysis, the top two chemical reaction rates were selected as uniformly distributed aleatory parameters

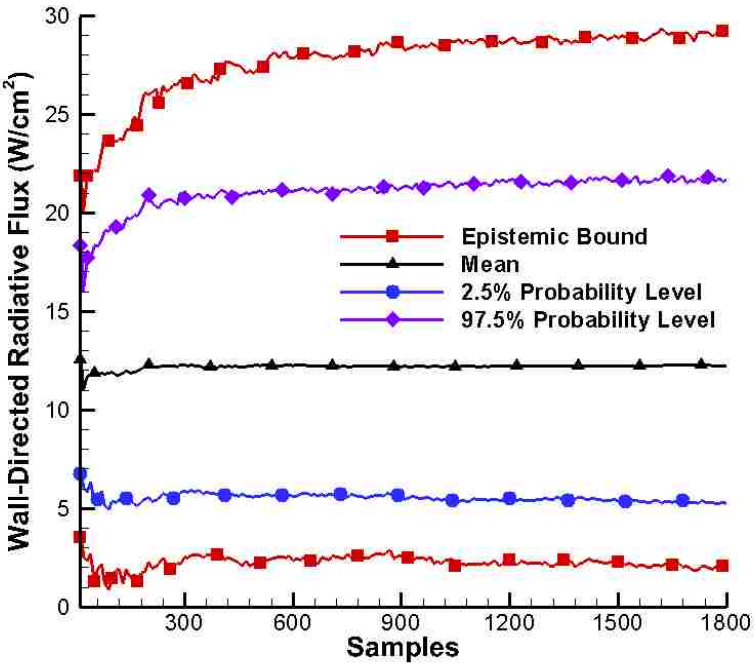

Figure 7.7. Convergence of Pure Aleatory and Epistemic Intervals for the Stagnation Point

while the remaining 91 variables were assumed epistemic. These were the same two parameters that were assumed aleatory in previous work by West et al. [33] Following the procedure outlined in Section 3, probability box plots could be obtained at each iteration. A collection of p-boxes are shown in Figure 7.8 at selected sample sizes. Note that in this figure, the 20 sample bounds are vertical lines. This is because the recovery procedure found a solution which did not include contribution from the two aleatory parameters. This is not correct as these two parameters account for about 35% of the total output uncertainty, as seen from Figure 7.6, indicating that more iterations to converge the PCE coefficients are necessary.

A comparison of the above analyses with previous work by West et al. [33] confirms the results obtained with the sparse sampling approach of the current work. The 95% confidence intervals of the pure aleatory and mixed uncertainty analyses

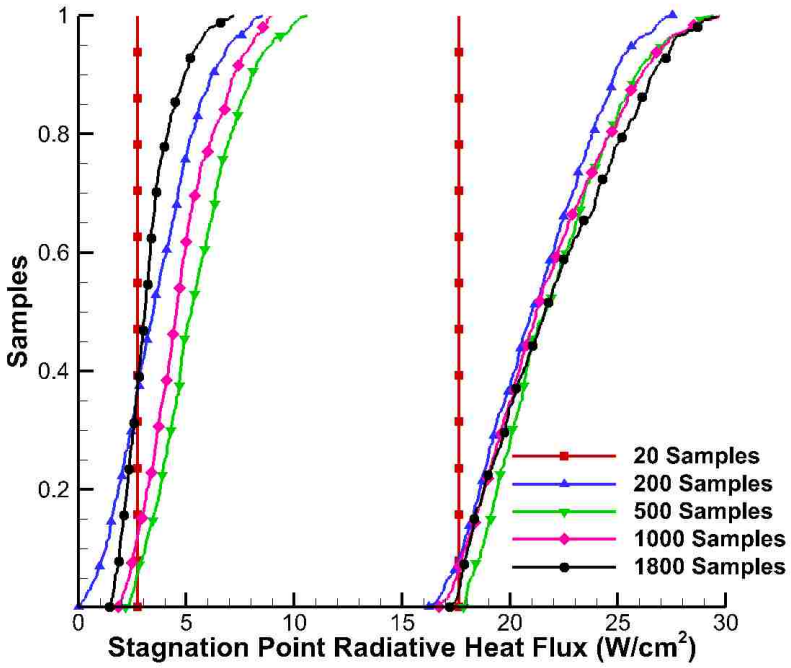

Figure 7.8. P-box of Mixed Uncertainty Analysis at Selected Sample Sizes

as well as the pure epistemic analysis are compared in Table 7.2. Note that in the previous work, a dimension reduction scheme was employed before creating the surrogate mode. The 93 variables were reduced to 5 variables which accounted for over 90% of the uncertainty. This will inherently make the intervals narrower than those obtained in the current work as 10% of the uncertainty is not being accounted for in the previous work. The differences between the intervals between the previous work and the current study are small with the differences between all six interval values being less than 3 W/cm^2.

The variation in the fraction of the total sample set required for accurate results between the two model problems can be explained by the difference in the faction of uncertain variables that contribute significantly to the total uncertainty. For the convective heat transfer model problem, it can be seen that 6 of the 11 uncertain

Table 7.2. Comparison of Stagnation Point Radiative Flux Intervals for Different Analyses

Parameter	1800 Samples (W/cm^2)	West et al. [33] (W/cm^2)	Difference (W/cm^2)
Epistemic Interval	[1.22 , 31.26]	[1.98 , 28.65]	[0.76 , 2.61]
Aleatory 95% Confidence Interval	[5.25 , 21.70]	[4.66 , 20.47]	[0.59 , 1.23]
Mixed 95% Confidence Interval	[1.63 , 28.38]	[2.24 , 25.68]	[0.61 , 2.70]

variable contribute more than 1% to the total uncertainty and the recovery procedure needed about 30 of the 78 samples (about 40%) to obtain accurate PCE coefficients. On the other hand, for the Mars entry radiation problem, only about 8 of the 93 uncertain parameters contribute over 1% to the total uncertainty. In light of this, less than 10% of the full 4465 sample set is needed to recover accurate expansion coefficients, as measured by the two converge approaches. Because such a small fraction of the uncertain parameters in the Mars entry problem actually contribute to the total uncertainty, a significantly large portion of the expansion coefficients are close to zero. This is the assumption of the Basis Pursuit Denoising problem used to recover the PCE coefficients. Therefore, the Mars entry problem may be more suited for this type of sparse sampling analysis allowing for accurate PCE coefficients to be obtained with a small fraction of the samples normally required for an analytical result. For many large scale problems, with many uncertain variables, it may be the case that only a few variables contribute significantly to the total uncertainty making the ideas presented in the current work an attractive approach to performing efficient and accurate uncertainty quantification. However, even if this is not the case, it has still been shown by the convective heat flux model that accurate PCE coefficients and subsequent response surfaces can be obtained for a reduced number of evaluations of the deterministic model over the number needed for a least squares solution of Eq. (2).

Because of the flexibility and ease of implementation of NIPC, analyses can be performed on multiple design quantities of interest using the same deterministic model evaluations. In the previous section, the radiative heat flux was investigated at the stagnation point of the HIAD. As the deterministic CFD simulations are already available, the radiative heat flux was investigated along the entire surface of the HIAD at 14 point selected between the stagnation point and the shoulder region. The same three aleatory, epistemic, and mixed uncertainty analyses were performed on each of the 14 points on the wall. Note that new surrogate models were constructed at each point using the aforementioned sparse sampling approach. Figure 7.9 shows the distribution of the wall directed radiative flux for all three analyses using 1800 samples.

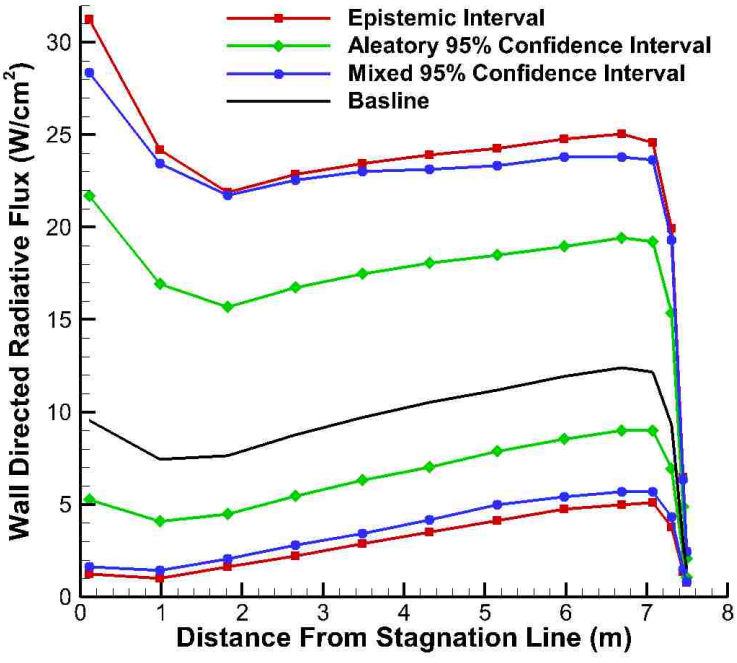

Figure 7.9. Wall Directed Radiative Heat Flux Distribution Along HIAD Surface

As with the analysis in the previous section, notice that the epistemic interval bounds both the aleatory and mixed analyses as this is the extrema of the response surface. This figure shows the importance of correct representation of the uncertainty. A pure epistemic analysis is a "worst case" analysis. This type of analysis may result in a over design of a thermal protection system (TPS) if some of the parameters are not classified correctly. Also, the edges of the response surface can carry a significant amount of uncertainty themselves. A probabilistic analysis may be the more appropriate method. However, this should be done with caution. Assuming that all parameters have a probabilistic representation can lead to a potential under design. From Figure 7.9, notice that the aleatory analysis 95% confidence interval is inside the mixed uncertainty interval. A mixed uncertainty analysis propagates both epistemic and aleatory parameters through a model and may be the most accurate approach in the instance when both types of uncertainty exist. This strongly highlights the importance of accurate uncertain variable classification.

From Figure 7.9, it can be seen that the radiative flux varies along the surface of the HIAD. It may be of interest to investigate the sensitivity of the radiative flux to the uncertain parameters at different points along the surface. Figures 7.10 and 7.11 show the convergence of the Sobol indices of the parameters that account for 90% of the uncertainty at wall points 3 and 9, respectively, which are about 1.8 m and 6.7 m from the stagnation point. It should be pointed out that, in this particular case, the Sobol indices are independent of the classification of uncertainty parameters. Each parameter was represented by an interval. Therefore, the basis of the PCE is comprised entirely of a Legendre basis [11].

In Figure 7.10 the variable ranking is unchanged and only small changes in the total Sobol Values exist when compared to the stagnation point results in Figure 7.6. However, a difference can be noticed for the wall point 9 results given in Figure 7.11. First of all, seven parameters now represent about 90% of the total uncertainty were,

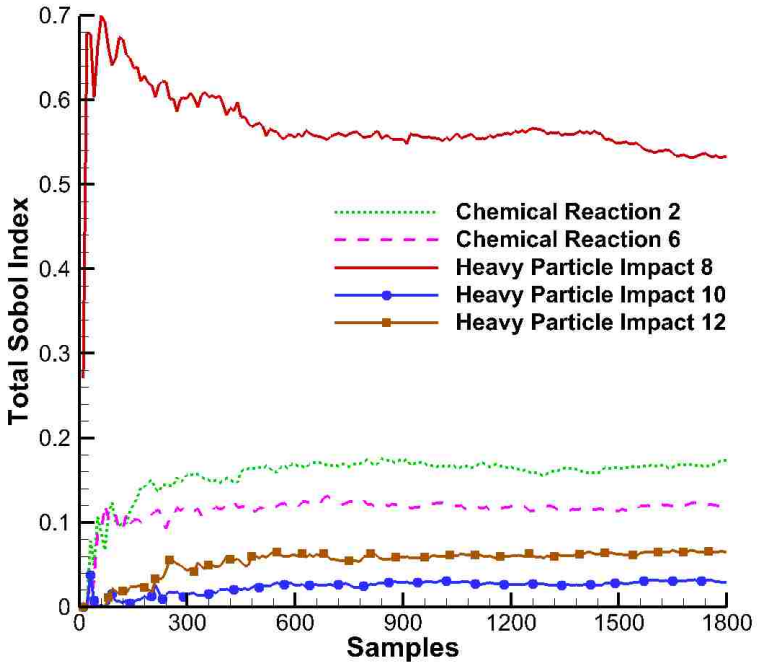

Figure 7.10. Convergence of Uncertain Parameters Accounting for 90% Uncertainty at Wall Point 3 (x=1.8 m from the Stagnation Point)

as before, only five variables accounted for 90% of the uncertainty. Second, notice that the top three parameters remain the top three, but with a change in the ranking between variables two and three. The inclusion of new parameters is the result of changes within the shock layer. Johnston et al. [39] discusses that there is a large region of thermochemical nonequilibrium within the shock layer and is located just behind the shock. Moving down stream along the surface of the HIAD, the size of the nonequilibrium region decreases and the shock stand-off distance begins to grow linearly from the sphere-cone juncture as shown in Figure 7.12. It is known that the CO 4th Positive band is the highest emitting band at near the stagnation region in this analysis due to the region of nonequilibrium [39]. However, the emission of this band decreases downstream due to the reduction in the nonequilibrium region size, as shown in Figures 7.13, 7.14, and 7.15. The volumetric radiance from the CO 4th

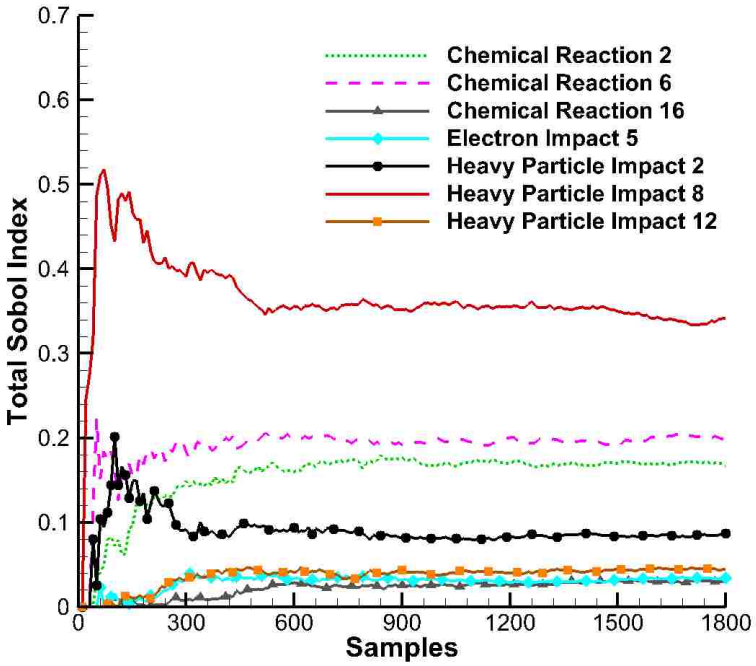

Figure 7.11. Convergence of Uncertain Parameters Accounting for 90% Uncertainty at Wall Point 9 (x=6.7 m from the Stagnation Point)

Positive band decreases from the stagnation point. In addition to the decrease in emission, the increase in shock stand-off distance creates a longer path for absorption of the optically thick CO 4th Positive band emission from the nonequilibrium region.

In terms of the Sobol indices, this explains the decrease in the contribution from parameters involving CO. In Figure 7.11, the new parameters that arise to account for 90% of the uncertainty are related to the CN Violet band. This band is known to be the second highest emitter in this model problem [39]. Unlike the CO 4th Positive band, CN violet is optically thin and, therefore, is not subject to significant self absorption. Because of this, the contribution from CN Violet to the radiative flux increases linearly with shock stand off distance. This is evident in Figure 7.15 as the wall directed radiative flux is increasing from the shock to the wall.

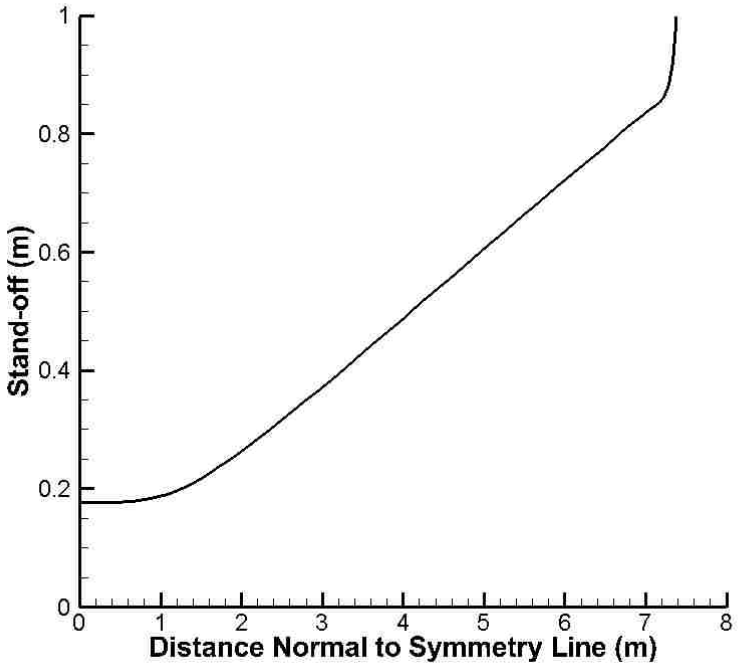

Figure 7.12. Shock Stand-off Distance for Mars Entry HIAD

7.3.3. Radiative Heat Flux Prediction during Titan Entry. The objective with this problem is to investigate the uncertainty in high-fidelity radiative heat flux predictions on the surface of a HIAD scale geometry during Titan entry by using the sparse approximation approach. This problem is similar to the Mars problem discussed in previous sections, but for entry into Titan. The flow field was modeled using the LAURA finite-volume, Navier-Stokes flow solver [40]. This solver uses a second-order, upwind, discretization scheme with relaxation of both inviscid and viscous terms for solution stability. LAURA has been used for many high energy flow studies and has been extensively validated for various atmospheric entry flow scenarios. The flow field was assumed to be steady state and was modeled using a two-temperature, thermochemical nonequilibrium model [46, 47]. A constant 1500

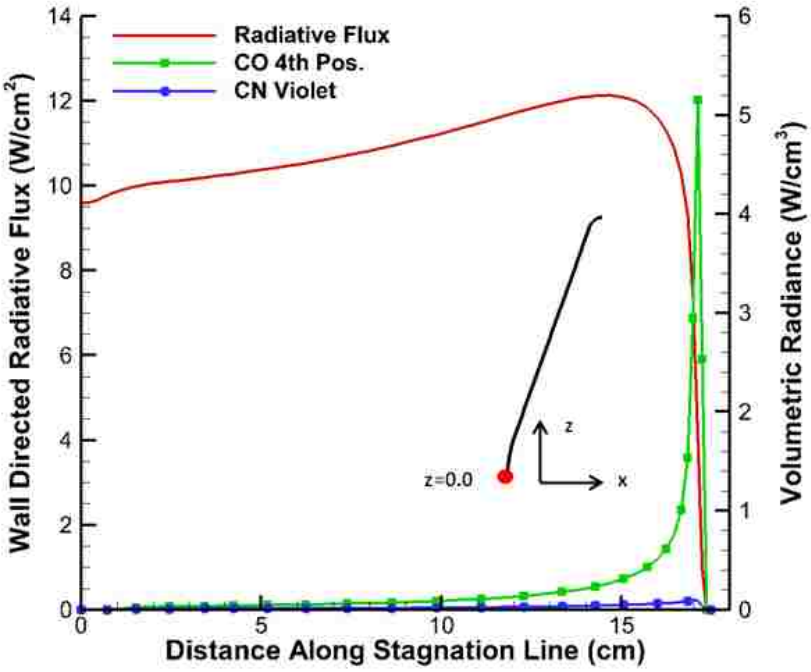

Figure 7.13. Radiative Flux and Volumetric Radiance Along the Stagnation Line

K, super-catalytic wall boundary condition is assumed. Note that the super-catalytic assumption has a negligible effect on the radiative heating [39].

Johnston et al. [39] details the vibrational relaxation models used in the present study. Bose et al. [48] showed that uncertainty in the vibrational relaxation parameters contributes about 5% to the total uncertainty due to the increased thermal equilibrium in the radiating portion of the shock layer. Note that this 5% is relative to the total amount of uncertainty observed in that study, which is less than the amount obtained in the current study. These parameters are subsequently neglected in the current study, because they have been shown to have a relatively weak contribution.

The radiation was modeled using the High-Temperature Aerothermodynamic Radiation (HARA) code [41, 42]. This nonequilibrium radiation code uses a tangent-slab approximation for computing the radiative flux and its divergence. HARA is

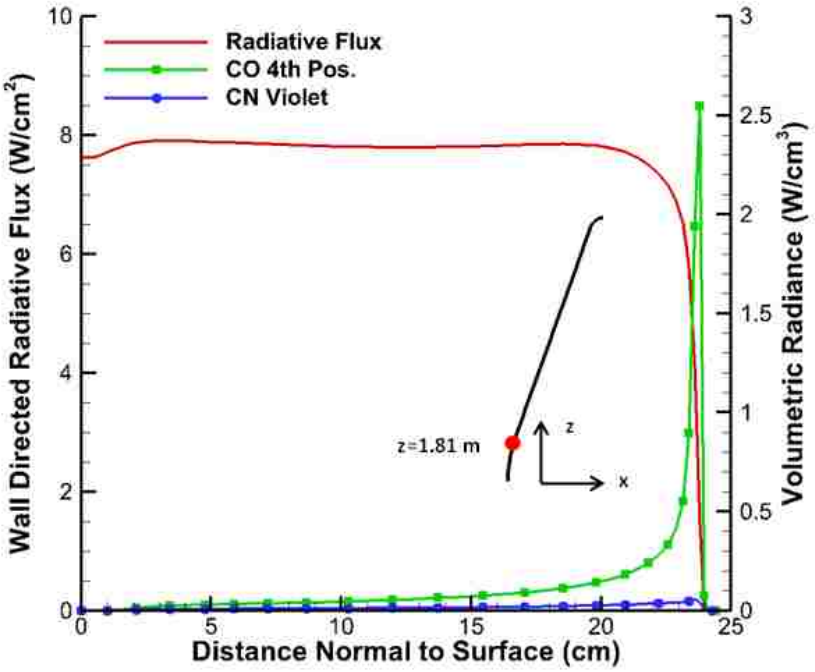

Figure 7.14. Radiative Flux and Volumetric Radiance Normal to Wall Point 3

based on a set of atomic levels and lines obtained from the National Institute of Standards and Technology (NIST) database [49], Opacity Project databases [50], and atomic bound-free (photoionization) cross-sections from the TOPbase [51]. In the present study, the flow field solver and the radiative heat transfer calculations are coupled. HARA calculates the radiative flux and the divergence of the radiative flux, which are included in the flow field calculations. Previous work has shown that this coupling can significantly affect the radiation prediction [52]. HARA uses a Collisional Radiative (CR) or non-Boltzmann modeling of atomic and molecular electronic states. The non-Boltzmann approach used in this study is described in detail by Johnston et al. [39]

Molecular band systems, considered in this study, are treated using the smeared-rotational band (SRB) approach. However, the use of an SRB approach may be a

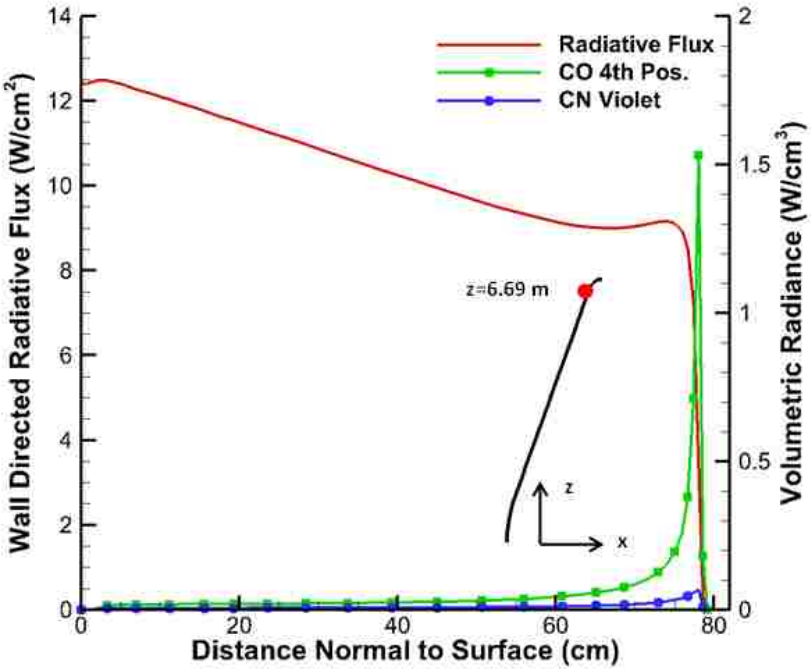

Figure 7.15. Radiative Flux and Volumetric Radiance Normal to Wall Point 9

significant approximation for strong band systems. When multiple simulations are needed, such as when performing UQ, detailed Line-by-Line (LBL) treatment may not be feasible due to a significant increase in computational expense. However, the effect of the SRB approximation will only change the magnitude of the radiation. Output uncertainty ranges and sensitivity information are not significantly effected by using the SRB approach versus the LBL treatment, for the cases considered here[53]. A comparison of the computational cost between SRB and LBL treatment is made at the end of this section.

The HIAD geometry is modeled as a 70 degree spherical cone with a nose radius of 3.75 m, a shoulder radius of 0.375 m, and a base radius of 7.5 m. A sample of the computational grid and grid convergence study results are shown in Figure 7.16. The computational grid used for this geometry was 128×48. The grid varies based

on the shock location. LAURA uses a gradient-based shock capturing technique to detect and cluster the grid in the flow direction. A sample of the grid is shown in Figure 7.16(a). Results of a grid convergence study are shown in Figure 7.16(b). The difference between the finest grid and the grid used in this study is less than 2% at the peak heat value. Because of the added computational cost of the finer grid, this error was deemed acceptable. Note that the HIAD is symmetric and is at zero angle of attack. This makes the flow asymmetric.

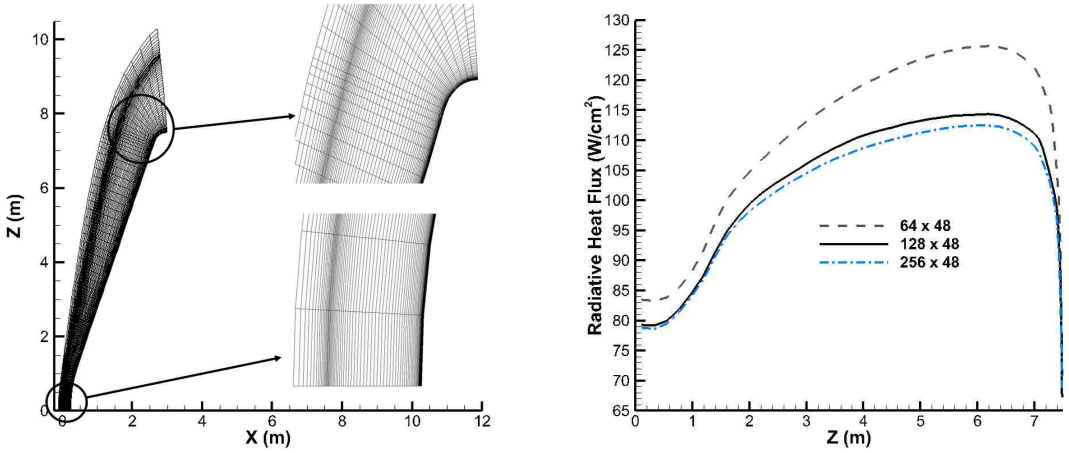

(a) Computational Grid

(b) Surface Radiative Heat Flux for Different Grid Sizes

Figure 7.16. Computational Grid and Grid Convergence

The Titan atmosphere is composed of primarily N_2 (97% per mole) with a small amount of methane (2.3% per mole) and argon (0.7% per mole). A unique feature of the Titan atmosphere is its height. The Huygens Probe detected entry interface at over 1,200 km above the surface [54]. While the atmosphere starts well above the surface, it is not overly dense as the Huygens probe dropped to about 400 km above surface before significant aerodynamic drag became present [55]. To determine the entry conditions used in the present study for a HIAD entry, a simple six degree of

freedom ballistic trajectory analysis was performed [56]. Coupled with a radiative heat flux correlation [57], the peak, stagnation point radiative heating on the HIAD occurred at a speed, density, and temperature of 6 km/s, 1.5e-4 kg/m^3, and 150 K, respectively. Note that these condition are similar to those predicted as the maximum heating conditions during the Huygens entry [58, 59, 60, 52]. Also, the flow field has been assumed to be laminar throughout as Johnston et al. [61] has shown that the fully laminar assumption has a negligible effect on radiative heating.

The flow field was modeled with a 21 species composition model: CH_4, CH_3, CH_2, CH, N_2, C_2, H_2, CN, NH, Ar, HCN, N, C, H, N_2^+, CN^+, N^+, C^+, H^+, Ar^+, and e^-. The 35-reaction finite-rate chemistry reduced order model presented by Gokcen [62] was used in the present study. This reduced order model was obtained through a sensitivity analysis performed at various Titan entry conditions. The 35 reactions, shown in Table B1, consist of dissociation, exchange, and ionization reactions. Shown also in this table are the uncertainty magnitudes, also identified by Gokcen [62]. Following the notation used by Gokcen[62], each reaction rate is multiplied and divided by the corresponding F_i factor to obtain the upper and lower bounds of the uncertainty interval, respectively. Because the effect of the uncertainty in the ionization reaction rates on radiative heating uncertainty was not investigated in previous studies, these rates are retained in the current uncertainty analysis. Note that Gokcen [62] suggests that the provided uncertainty ranges be considered as the lower limit of the uncertainty.

The molecular band systems considered in this study are shown in Table B2. The uncertainties in these band systems were taken from Johnston et al.[39]. Initially, the N_2 1st Positive, N_2 2nd Positive, and the N_2^- 1st Negative band systems were also considered to determine their contribution to the radiative heat flux. However, all together these three bands were observed to contribute less the 1% to the total radiative heating for the entry conditions used in the present work. Therefore, these

bands were not treated throughout this study. Emission from NH molecule excited states have also been identified as a potential source of radiation [63]. Brandis et al. [64] showed that the primary NH transition does not contribute significantly to the radiation and is, therefore, ignored in the present study. The effect of atomic line emission and photoionization from C and N atoms was also investigated, but was found to contribute less than 1% to the total radiative heat flux and are not considered throughout this study

The non-Boltzmann excitation rates considered are the excitation of CN and C_2. These reactions and their uncertainty are given in Tables B3 and B4 for the heavy particle and electron impact excitation rates, respectively. The uncertainty in these reactions are given by Johnston et al.[39].

A baseline solution was obtained for the Titan entry simulation prior to performing the UQ analysis and is depicted in Figure 7.3.3. Temperature and pressure contours of the Titan entry flow field are given in Figures 7.17(a) and 7.17(b), respectively. Also, a plot of the shock stand-off distance is given in Figure 7.17(c) and the baseline radiative heat flux distribution along the surface of the HIAD is given in Figure 7.17(d). These figures show a well defined shock layer and a smooth surface radiative heat flux.

Work by Olejniczak et al. [59] showed that the radiation during Titan entry can contribute three to five times more wall heat flux than the convection. This is primarily due to emission from the optically thin CN molecule band systems [65]. The radiation spectra are shown in Figure 7.18 at three locations along the surface of the HIAD: the stagnation point, 5.15 meters normal to the stagnation line, and 6.69 meters normal to the stagnation line. At the stagnation point, shown in Figure 7.18(a), notice the sharp contribution from the CN Violet band system between 350 and 450 nm. The remainder of the emission is coming from the CN Red band system. Moving along the surface, this emission from CN Violet begins to decrease; however,

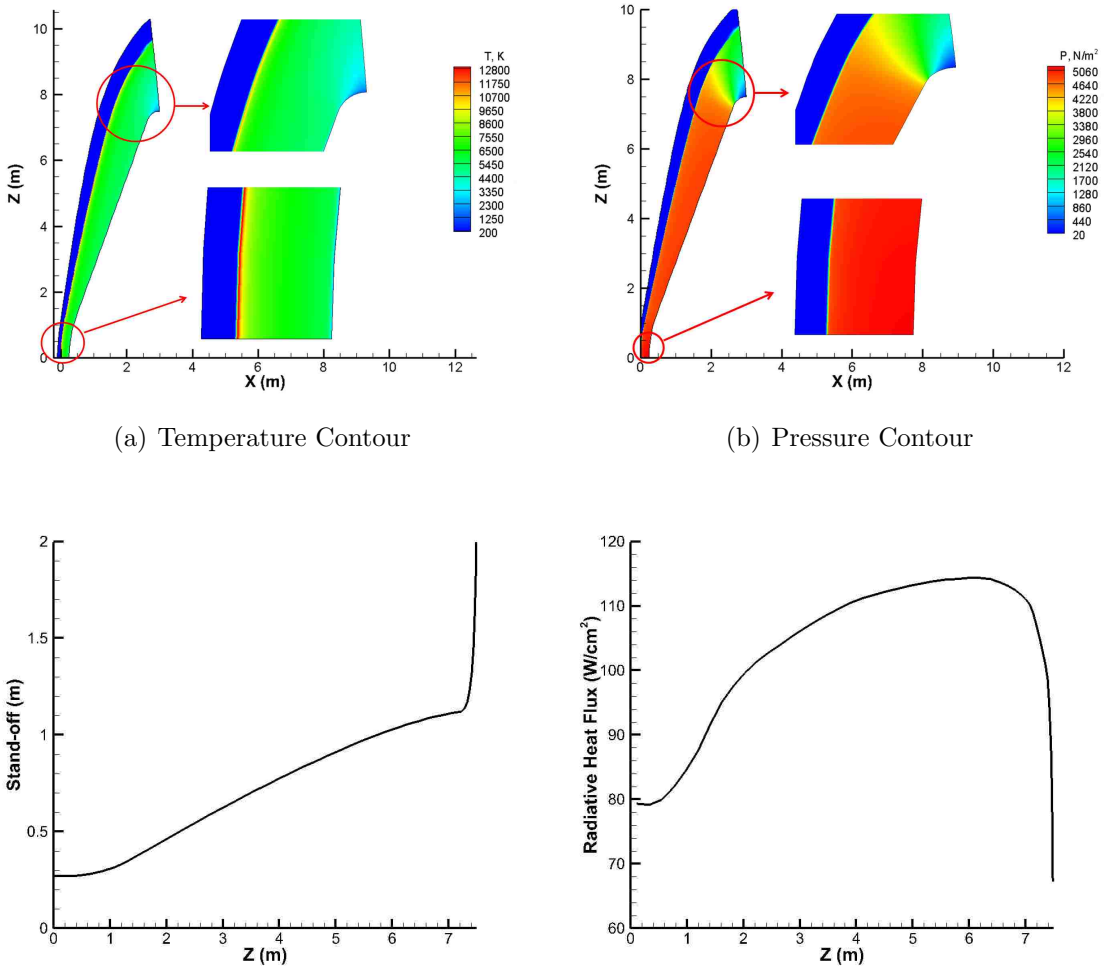

(a) Temperature Contour

(b) Pressure Contour

(c) Shock Stand-off Distance

(d) Wall Radiative Heat Flux

Figure 7.17. Titan Entry Baseline Case

the total wall radiative heat flux continues to increase. This is due to the emission from the CN Red system, which spans over a large range of wavelengths. The C_2 Swan band is visible, but only slightly contributes to the total radiation, along the surface of the HIAD.

Shock-layer temperature and radiation profiles are shown in Figures 7.19 and 7.20, respectively. Stagnation line temperature and radiation plots are shown in Figures 7.19(a) and 7.20(a), respectively. The nonequilibrium region is significant

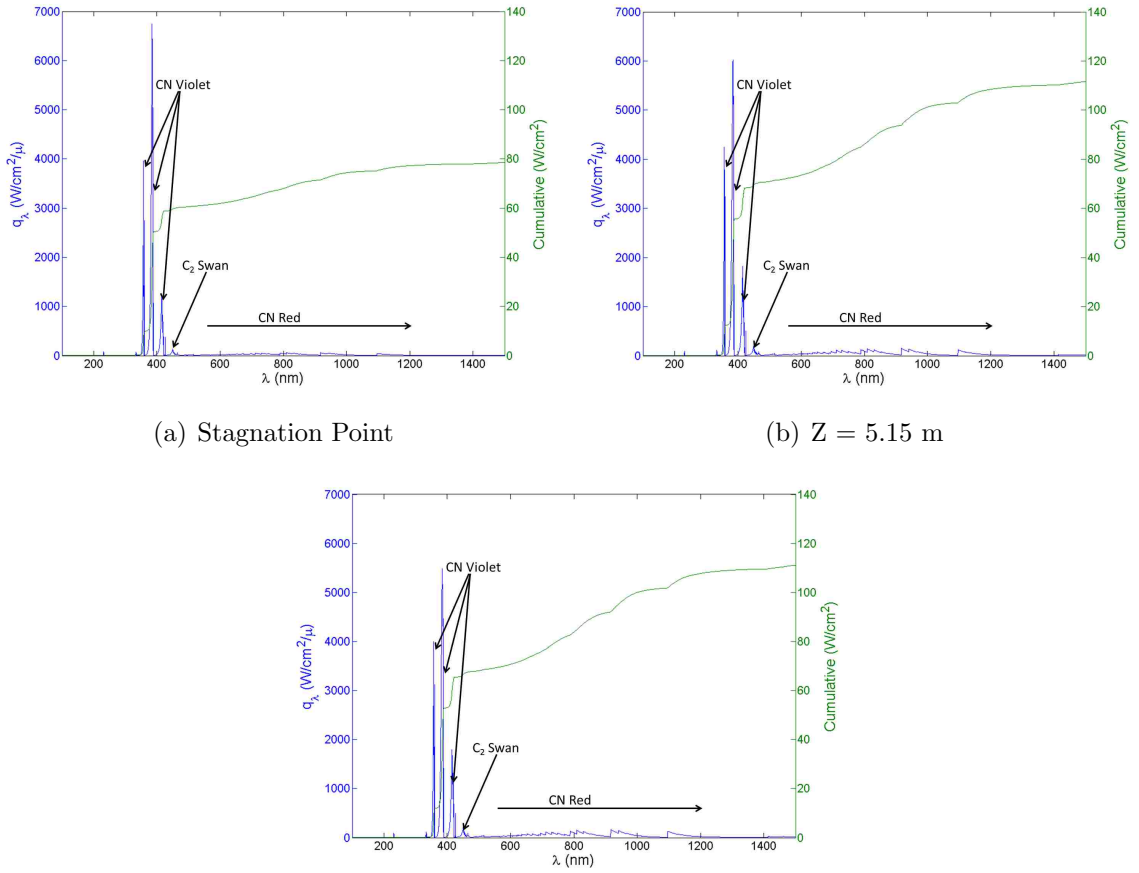

(a) Stagnation Point

(b) Z = 5.15 m

(c) Z = 6.69 m

Figure 7.18. Titan Entry Radiative Flux Spectra Along the HIAD Surface

throughout the Titan entry shock layer, as indicated by the large difference between the equilibrium and translation/vibrational temperatures. Also, the radiation actually increases across nearly the entire shock layer. Moving further along the HIAD surface, the trends seen at the stagnation point remain the same. This is shown at about the midpoint of the linear region of the fore body in Figures 7.19(b) and 7.20(b) and near the shoulder region in Figures 7.19(c) and 7.20(c). From these figures, even though the peak temperature within the shock layer decreases moving towards the shoulder, the radiative flux at the wall still grows significantly. This is

due in part to the increasing shock stand-off distance, which creates a larger path for the optically thin CN Red band system to emit.

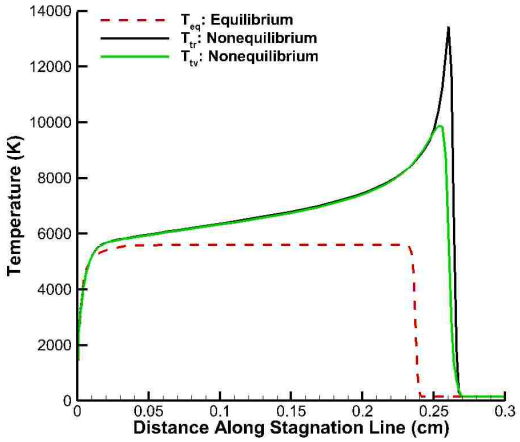

(a) Stagnation Line

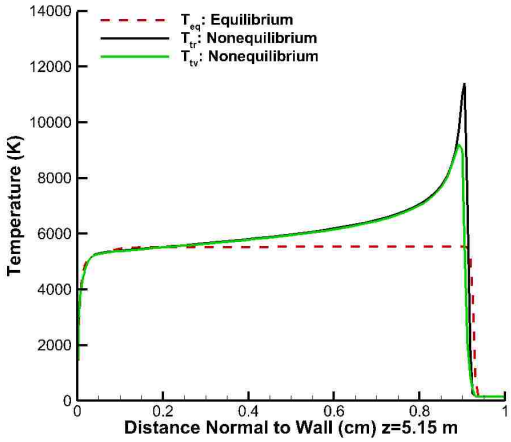

(b) Z = 5.15 m

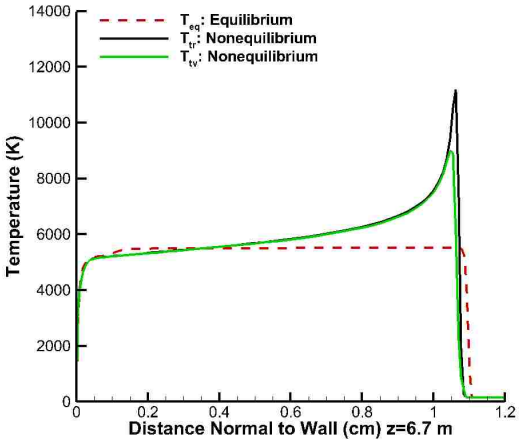

(c) Z = 6.69 m

Figure 7.19. Titan Baseline Stagnation Line Temperature and Radiative Heat Flux Distributions

An important note should be made with regards to two assumptions made in this work that may significantly affect the radiative heat predictions for the Titan case. The first is the SRB assumption used for treatment of the CN Violet and Red band

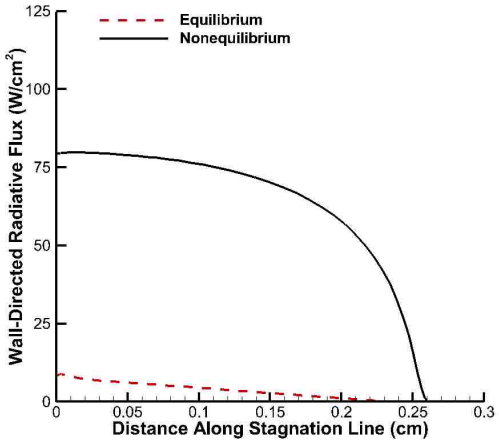

(a) Stagnation Line

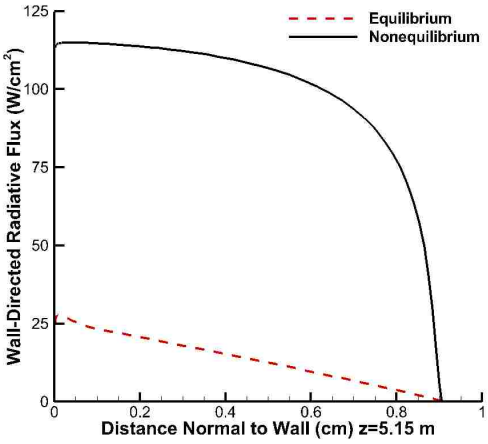

(b) Z = 5.15 m

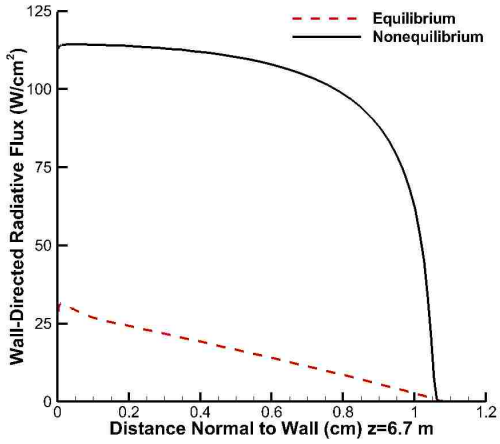

(c) Z = 6.69 m

Figure 7.20. Titan Baseline Stagnation Line Temperature and Radiative Heat Flux Distributions

systems. Figure 7.21 shows that the SRB approximation over predicts the surface radiation versus the LBL treatment. For optically thin gases, the SRB model will replicate the spectrally-integrated LBL radiative flux. Therefore, the difference seen in Figure 7.21 indicates that the CN Violet band is not optically thin. While using an SRB approach is a known simplification, it is a necessary one for a UQ analysis simply due to the extreme computational cost of the LBL calculations. A comparison

of the time required to complete a single call to radiation code showed that the SRB treatment took less than 1 minute per line of sight, while the LBL treatment took about 50 minutes per line of sight on the same single CPU. This gives an idea of the relative complexity of the two methods. Note that in this study, there were a total of 48 lines to sight. The amount of time to complete a case is also compounded by the fact that the solution is iterative, so many calls to the radiation code are required.

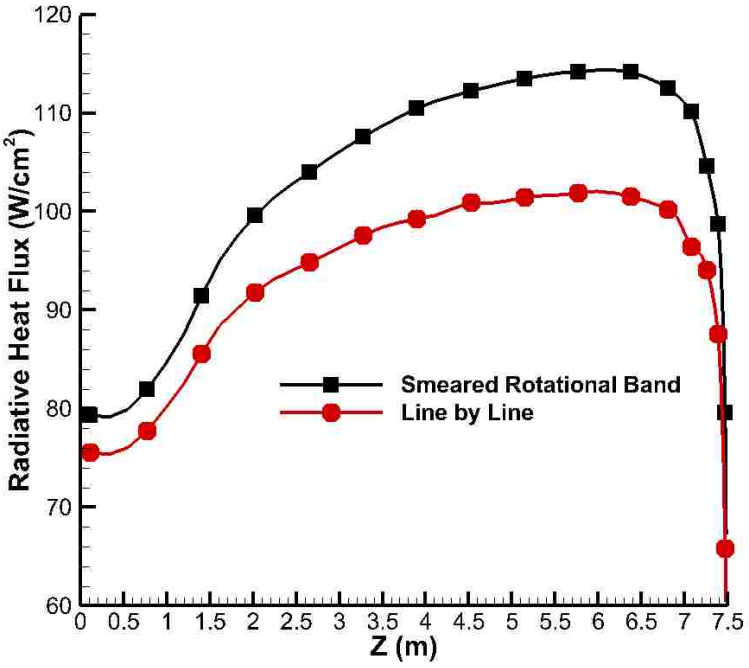

Figure 7.21. Titan Entry Comparison of LBL vs. SRB Treatment for CN Violet and Red Band Systems

The second assumption is the tangent-slab approximation used by LAURA to compute the wall-directed radiative flux. While this approach is computationally inexpensive compared to other options, Bose et al. [66] and Wright et al. [52] showed that this assumption can lead to an over prediction of the surface radiation.

Mazaheri et al. [67], developed a computationally efficient three-dimensional, ray-tracing approach that may improve radiation predictions regardless of the optical depth and may be considered in future work.

The uncertainty was propagated through the model using Monte Carlo sampling of the stochastic response surface. While large sample sizes are typically needed for accurate results (on the order of 10^5), sampling the surrogate model is extremely inexpensive compared to sampling the actual deterministic model. Two uncertainty analyses were performed: a pure epistemic analysis and a pure aleatory analysis. As discussed in the previous section, all of the uncertain parameters in this study were treated on intervals. This means that the surrogate models do not change based on the uncertain parameter classification (i.e., each surrogate will have a pure Legendre basis[11]). The purpose of performing these two analyses is to show the effect of uncertain parameter classification, interpretation of output uncertainty, and the importance of correctly representing uncertain parameters.

The epistemic UQ approach is the correct analysis because no probabilistic assumption is made on the representation of the input uncertainty sources due to the lack of sufficient information [68]. The outputs from an epistemic analysis have no associated probability of occurrence, but each output can occur. As a result, the maximum and minimum response values are the outputs of interest in this analysis. To obtain a probabilistic representation of the output uncertainty (i.e., a pure aleatory analysis), samples of the surrogate model are sorted and spaced at equal probability levels, where the number of levels is dependent on the number of samples.

As discussed in above and listed in the appendix, a total of 79 uncertain input parameters, coming from four main groups (flow field chemical kinetics, molecular band systems, heavy particle impact excitation rates, and electron impact excitation rates), are considered for the Titan entry model. Using Eq. (2), a second order PCE would have 3,240 terms. A direct solution of Eq. (3) would require at least this

many evaluations of the deterministic model. Instead, sparse approximations of the PCEs were obtained from the optimization routine in Eq. (25), which was solved with an iteratively increased sample set, from 10 samples to 500 samples, increased by 10 samples at each iteration. The convergence results are shown in Figure 7.22. Convergence of the Sobol indices at three location along the surface of the HIAD are shown in Figure 7.22(a). In 500 samples, the error drops below 1% at all three points and is an indication of the convergence of the PCE coefficients. This error is deemed acceptable given the near 85% drop in computational cost (i.e., the number of CFD evaluations). A total of 100 test points were generated in the design space to measure the accuracy of the surrogate models. The plot of the normalized empirical error is shown in Figure 7.22(b). With 500 samples, the test point error is about 8%. Given the nature and complexity of the CFD model problem, both errors are deemed acceptable especially considering the significant computational savings achieved with the current UQ approach.

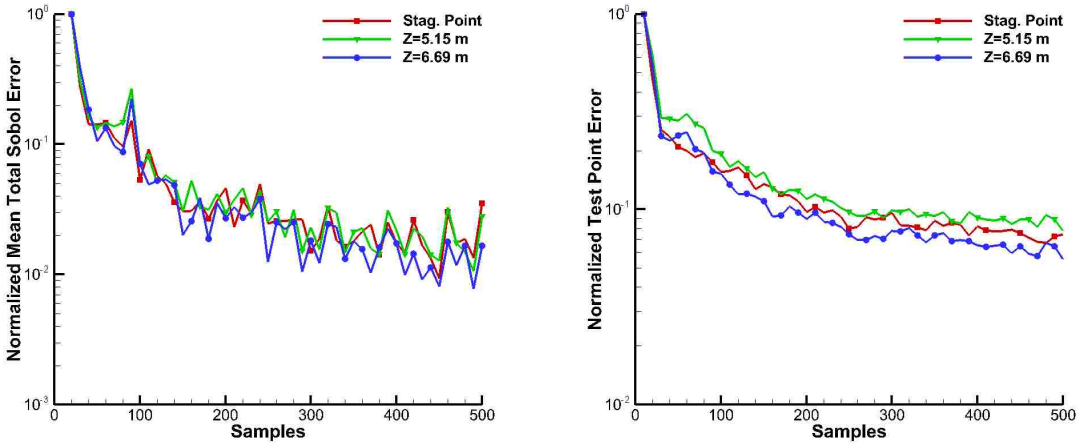

(a) Mean Sobol Index Error

(b) Test Point Error

Figure 7.22. Convergence of Sparse PCEs for Titan Entry

Thirteen surrogate models of the surface radiative heating were generated along the surface of the HIAD. The epistemic and the 95% confidence intervals of the wall radiative heat flux are shown in Figure 7.23. This figure highlights the importance of correct representation of uncertain parameters, because the 95% confidence interval is as much as a 50 W/cm^2 narrower than the epistemic interval. This under prediction of the output uncertainty is also discussed by Johnston and Kleb [69]. Many, if not all of the uncertain parameters considered in this study are epistemic simply due to the lack of knowledge about their behavior. While experimental data exists for some of the uncertain parameters, currently there is not enough to claim that these parameters exhibit obvious probabilistic uncertainty behavior. Figure 7.23 shows the substantial variation in the predicted radiative heating along the surface. At the shoulder region, the epistemic interval is nearly 150 W/cm^2 wide. This range is as much as the peak baseline prediction and is an indication of the significant contribution of the uncertain parameters to the wall radiative heating predictions.

Further checks of the convergence of the PCE coefficients can be done by checking the convergence of the intervals in Figure 7.23. The intervals are shown in Figure 7.24. At the stagnation point, convergence of both intervals are shown in Figure 7.24(a). Additionally, convergence of the intervals at Z = 5.15 meters and Z = 6.69 meters are shown in Figures 7.24(b) and 7.24(c), respectively. Notice the rapid convergence of both output intervals along the surface of the HIAD, which indicates converged PCE coefficients.

To better understand the cause of the significant variation in the radiative heating predictions, the Sobol indices used to measure the convergence of the PCEs are reviewed to determine the global, nonlinear sensitivity of the surface radiation to each of the uncertain input parameters. In a high level view, the pie charts in Figure 7.25 show the contribution from the four main groups of uncertain inputs. Clearly, the flow field reactions contribute the most to the output uncertainty, which

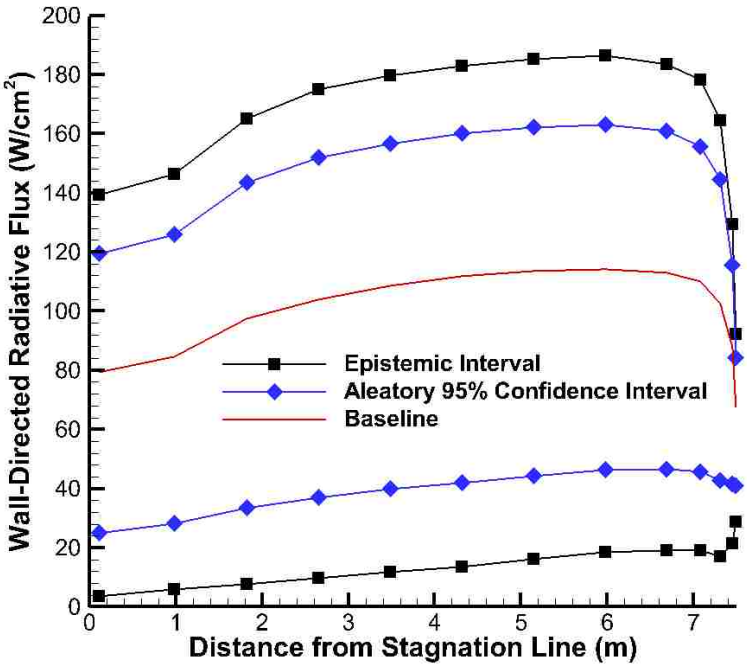

Figure 7.23. Epistemic and 95% Confidence Intervals of Wall Radiative Heat Flux for Titan Entry

is in agreement with previous works that have also shown that flow field chemistry contributes significantly to uncertainty in radiative heating predictions [48, 70, 35]. There is significant contribution from heavy particle impact excitation rates. Note that a significant change in the contribution from the different parameters along the surface of the HIAD is not observed. The flow field reactions dominate along the entire surface, with a small change between the heavy particle impacts and the molecular band contributions.

Looking closer at the contribution from individual parameters shows that only six of the 79 uncertain parameters contribute more than 1% to the total uncertainty at any point along the HIAD surface. These uncertainty sources and their contributions to the total output variance at three points along the surface are shown in Table 7.3. The most significant parameter is the reaction rate for the dissociation of N_2.

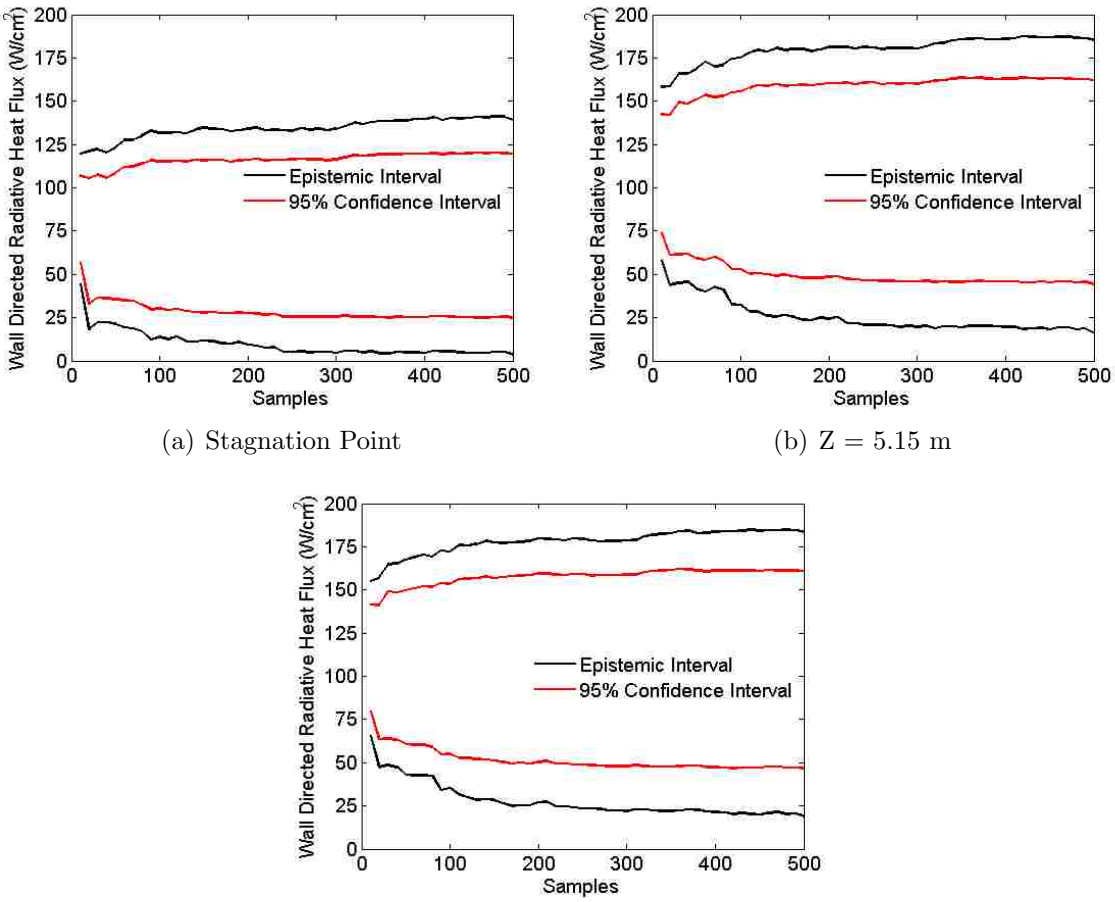

(a) Stagnation Point

(b) Z = 5.15 m

(c) Z = 6.69 m

Figure 7.24. Convergence of the Radiative Heating Uncertainty Intervals for Titan Entry

Molecular collisions contribute slightly more than atomic collisions. This sensitivity result is expected given that the freestream gas is composed of primarily N_2 and its dissociation directly affects the potential for the formation of radiating species. Bose et al. [48] notes that the H + N_2 $\leftrightarrow$ NH + N exchange reaction is highly endothermic and acts to cool the shock layer, reducing the heating from CN.

Contributions from the CN Red molecular band system, as well as the CN impact excitation rates are related to the most significant radiation contributer, CN. The excitation rates result in the excitation/de-excitation between the CN Red and

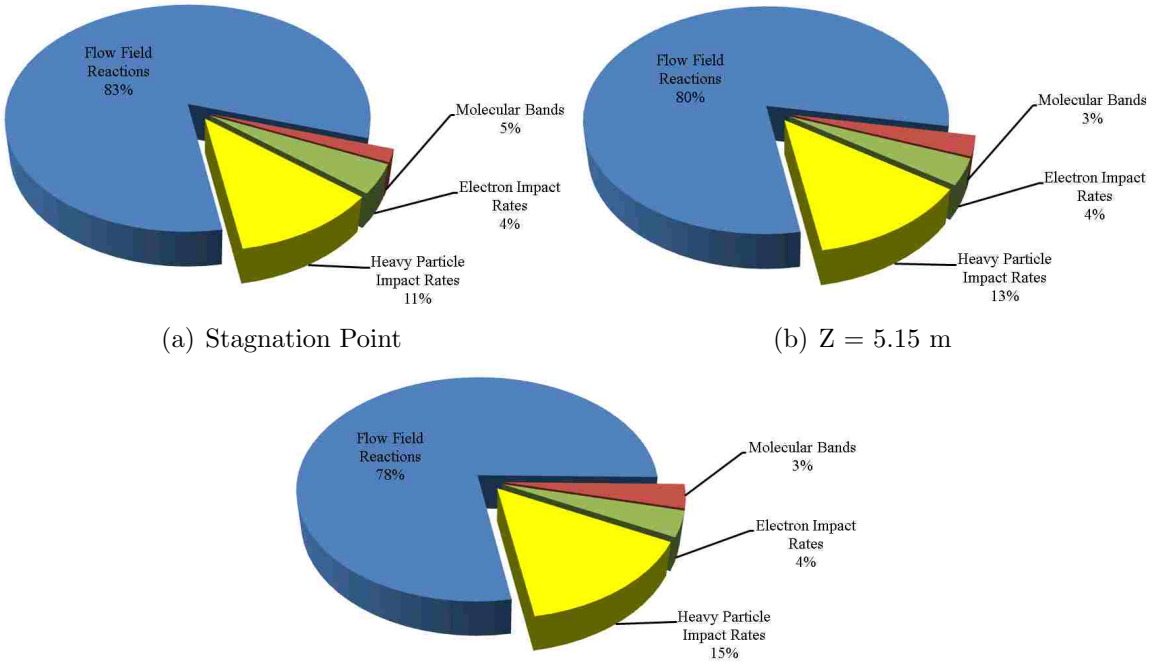

(a) Stagnation Point

(b) Z = 5.15 m

(c) Z = 6.69 m

Figure 7.25. Uncertainty Contributions to Titan Radiative Heating Along the HIAD Surface

CN Violent states, which can affect the emission from the CN molecule. From Table 7.3, the most important excitation rate is the heavy particle impact excitation rate for the transition between CN Red and CN Violet. The uncertainty in this particular excitation rate contributes about 10 - 15% to the total uncertainty in radiative heating along the surface. This contribution is quite significant to the radiative heat flux uncertainty, even though it is not the main contributor. This is a unique finding of this study, as electronic state excitation rates have not previously been considered uncertain for Titan entry radiation modeling.

Note that in previous work by West et al. [71], the Titan atmosphere was assumed to have a composition of 95% N_2 and 5% methane, which was made to align with previous work [35, 48] for comparison of the baseline and uncertainty/sensitivity analysis results. In the current study, the composition was updated to more accurately

reflect the composition of the Titan atmosphere. However, a comparison of the baseline and UQ results show that there is little change in the ranking of the important uncertain parameters and the width of the uncertainty intervals. What does change is simply the magnitude of the radiative heating. This is expected due to the reduction in the amount of carbon available for the production of CN.

Table 7.3. Top Uncertainty Sources Contributing to Radiative Heat Uncertainty

Uncertain Parameter	**Stag. Point**	**Z = 5.15 m**	**Z = 6.69 m**
N_2 + (Molecules) $\leftrightarrow$ 2N + (Molecules)	47.0%	47.9%	47.1%
N_2 + (H,C,N) $\leftrightarrow$ 2N + (H,C,N)	27.4%	28.2%	27.0%
CN($A^2\Pi$) + M $\leftrightarrow$ CN($B^2\Sigma^+$) + M	10.6%	12.3%	14.3%
CN($A^2\Pi$) + e^- $\leftrightarrow$ CN($B^2\Sigma^+$) + e^-	2.9%	2.9%	2.8%
C + e^- $\leftrightarrow$ C + e^- + e^-	2.7%	0.7%	0.4%
H + N_2 $\leftrightarrow$ NH + N	1.4%	1.6%	1.7%
CN ($A^2\Pi_i$ – $X^2\Sigma^+$)	0.6%	2.3%	3.0%
All Others	<1%	<1%	<1%

8. QUANTIFICATION OF MARGINS AND UNCERTAINTIES

Quantification of Margins and Uncertainties (QMU) is a methodology developed to facilitate analysis and communication of confidence for certification of complex systems. With the history of this approach discussed in Section 2, this section introduces enhancements to the QMU framework for improved analysis capability and efficiency. The QMU methodologies are demonstrated on two stochastic model problems. The first is a multi-system, multi-physics spacecraft reentry model, which consists of coupled reentry dynamics and heat load models to characterize design critical measurements of a spacecraft during reentry. These include the maximum g-load, a required bank angle correction, and the maximum heat load along the reentry trajectory. The second is a multi-system model for the prediction of ground noise produced by the sonic-boom from a supersonic transport vehicle.

8.1. COMPONENTS OF QMU

The key measures in the QMU are shown in Figure 8.1. In this QMU framework, for the whole aerospace system (spacecraft or aircraft) or for each sub-system, the first step will be to determine performance metrics (system outputs) relevant to the systems modeling. Then, these metrics will be evaluated at a design condition (point) determined for safe and reliable operation of the aerospace system. Each of these metrics (F) will typically involve some amount of uncertainty (U_F) due to the inherent (aleatory) or real-life variation of parameters used in physical models, as well as epistemic uncertainties. The safe and reliable operation region of the performance metrics (performance gates) may be bounded with a lower (FL) and/or an upper bound (FU) for each metric, which may also include some uncertainty (U_{FL} for FL and U_{FU} for FU) due to the aforementioned uncertainty sources. A measure of the

distance between the design value of each performance metric and the lower boundary including the effect of uncertainties U_F and U_{FL} will give the lower margin M_{LW} and the distance between the upper boundary and the design value of each performance metric including the effect of uncertainties U_F and U_{FU} will give the upper margin M_{UP}.

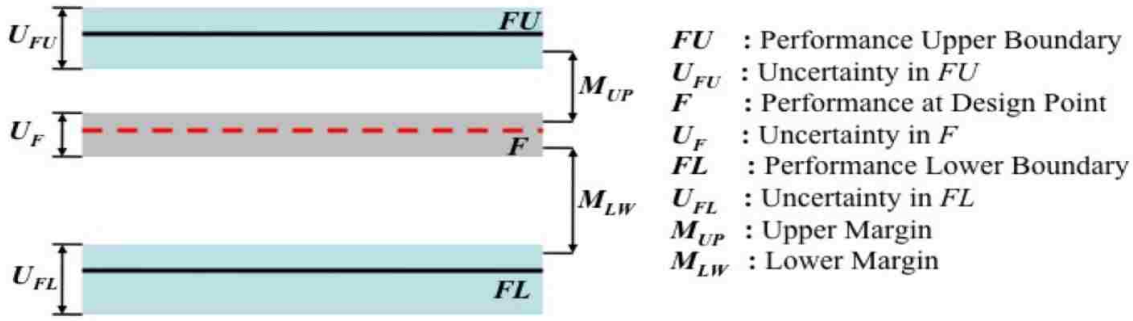

Figure 8.1. Schematic of Key Measures used in a QMU Analysis

Using the uncertainty and the margin information, a metric has to be developed to quantify and certify the confidence in safe operation of a system with a given performance metric. A confidence ratio (CR) can be defined as shown in Eq. (29). The confidence ratio is obtained as the minimum of the ratio of the margin to the uncertainty calculated for each side of a performance metric. For a system wide confidence level, the minimum of the CRs is utilized to represent the most critical or unreliable component of the system. Note that a performance metric may not possess both an upper and a lower performance boundary. In fact, in many engineering applications only a single limit may bound a performance metric. In this case, only a single ratio of the margin to the uncertainty exists and is considered as the confidence ratio for that particular metric (i.e. system performance or output.)

$$CR = Min\left[\frac{M_{UP}}{U_{UP}}, \frac{M_{LW}}{U_{LW}}\right] \tag{29}$$

8.2. UNCERTAINTY CALCULATIONS

In order to measure the uncertainty in the performance gate(s) of a system, the first step is to perform the actual uncertainty quantification of the design and the performance limits. In many problems, stochastic models may be used for determining the uncertainty in the output based on random input variables. This can be done by various UQ propagation methods; however, one of the goals of the current study to use stochastic responses surfaces for their computational efficiency and accuracy. An additional case may be that models are not directly available and the uncertainty must be quantified by other means. One example could be the use experimental test data. Then, it may be possible to represent the uncertainty of a design or performance limit with an interval or possibly fit a distribution to the data depending on its behavior.

After quantifying the uncertainty in the design and the performance limits, the next step is to quantify the uncertainty in the performance gates. For a probabilistic representation of the uncertainty, one approach would be to use Eqs. (30) and (31).

$$U_{UP} = \sqrt{\left((FU_{max})_{P=0.5} - (FU_{min})_{P=\frac{1-\beta}{2}}\right)^2 + \left((F_{min})_{P=0.5} - (F_{max})_{P=\frac{1+\beta}{2}}\right)^2} \tag{30}$$

$$U_{LW} = \sqrt{\left((F_{max})_{P=0.5} - (F_{min})_{P=\frac{1-\beta}{2}}\right)^2 + \left((FL_{min})_{P=0.5} - (FL_{max})_{P=\frac{1+\beta}{2}}\right)^2} \tag{31}$$

Here, β represents the confidence level used in the analysis and P represents the probability level at which the functional values are taken. For example, if $\beta =$

0.95, this would correspond to a 95% confidence level analysis. In case of mixed uncertainty in F, FU, and/or FL, min corresponds to the minimum and the max corresponds to maximum response value (bound) of the interval at that particular probability level, which can be obtained from the probability-box of the associated responses. Each of the square terms represents the uncertainty in either the design or a performance limit. Notice that the entire range of uncertainty in the design and the performance limits are not considered in Eqs. (30) and (31). By including only the uncertainty that will directly effect the performance gate on each side, the amount of uncertainty is restricted to each of the performance gates to avoid the under prediction of the reliability of the system as given by the CR in Eq. (29). For example, the uncertainty in the upper performance gate is measured by roughly the upper half of the uncertainty in the design and the lower half of the uncertainty in the upper performance limit. Similarly for the lower performance gate, the uncertainty is measured by roughly the lower half of the uncertainty in the design and the upper half of the uncertainty in the lower performance limit. In the case of mixed uncertainty, a conservative approach is taken to assess the amount of uncertainty in the performance gates. From Eq. (30), for example, the uncertainty in the design is measured as the distance between the upper output value at a selected probability level and the lower output value at the 50% probability level. Notice that the ladder of the two values is taken further from the performance gate in order to ensure that any uncertainty that could affect the reliability of the system is included in the measurement of the amount of uncertainty in the performance limit.

The desired approach is to generalize the uncertainty measurements in Eqs. (30) and (31) to include non-probabilistic representation of the uncertainty. This is done with Eqs. (32) and (33) where each of the terms are defined, based on the representation of the uncertainty, in Tables 8.1 and 8.2 for the upper and lower performance gates, respectively.

$$U_{UP} = \sqrt{(U_{UP1} - U_{UP2})^2 + (U_{UP3} - U_{UP4})^2} \tag{32}$$

$$U_{LW} = \sqrt{(U_{LW1} - U_{LW2})^2 + (U_{LW3} - U_{LW4})^2} \tag{33}$$

Table 8.1. Response Values of Different Uncertainty Representations for Upper Uncertainty Calculations

Uncertainty Representation	$U_{UP1}(FU)$	$U_{UP2}(FU)$	$U_{UP3}(F)$	$U_{UP4}(F)$
No Uncertainty	FU	FU	F	F
Pure Epistemic	$\frac{FU_{max}}{2}$	$\frac{FU_{min}}{2}$	$\frac{F_{max}}{2}$	$\frac{F_{min}}{2}$
Pure Aleatory	$(FU)_{P=0.5}$	$(FU)_{P=\frac{1-\beta}{2}}$	$(F)_{P=\frac{1+\beta}{2}}$	$(F)_{P=0.5}$
Mixed	$(FU_{max})_{P=0.5}$	$(FU_{min})_{P=\frac{1-\beta}{2}}$	$(F_{max})_{P=\frac{1+\beta}{2}}$	$(F_{min})_{P=0.5}$

Table 8.2. Response Values of Different Uncertainty Representations for Lower Uncertainty Calculations

Uncertainty Representation	$U_{LW1}(FL)$	$U_{LW2}(FL)$	$U_{LW3}(F)$	$U_{LW4}(F)$
No Uncertainty	FL	FL	F	F
Pure Epistemic	$\frac{FL_{max}}{2}$	$\frac{FL_{min}}{2}$	$\frac{F_{max}}{2}$	$\frac{F_{min}}{2}$
Pure Aleatory	$(FL)_{P=0.5}$	$(FL)_{P=\frac{1+\beta}{2}}$	$(F)_{P=\frac{1-\beta}{2}}$	$(F)_{P=0.5}$
Mixed	$(FL_{min})_{P=0.5}$	$(FL_{max})_{P=\frac{1+\beta}{2}}$	$(F_{min})_{P=\frac{1-\beta}{2}}$	$(F_{max})_{P=0.5}$

8.3. MARGIN CALCULATIONS

Calculation of the distance between the design condition and the performance limit, or the margin, is a critical component of QMU. Improper measurement could result in under or over prediction of the reliability of the system. While this measurement may graphically appear obvious as seen in Figure 8.1, if both the design and the performance limits posses uncertainty, the calculations should include the effects of these uncertainties to obtain an accurate margin estimate. Moreover, a general approach has been devised since the uncertainty characteristics (aleatory, epistemic, or mixed) for the design and limits may be different. Considering these, the calculation of the margins for a probabilistic representation of the uncertainty can be determined using Eqs. (34) and (35) for the upper and lower performance boundaries, respectively.

$$M_{UP} = \left| (FU_{min})_{P=\frac{1-\beta}{2}} - (F_{max})_{P=\frac{1+\beta}{2}} \right| \tag{34}$$

$$M_{LW} = \left| (F_{min})_{P=\frac{1-\beta}{2}} - (FL_{max})_{P=\frac{1+\beta}{2}} \right| \tag{35}$$

Here, β represents the confidence level used in the analysis and P represents the probability level at which the functional values are taken. For example, if $\beta = 0.95$ this would correspond to a 95% confidence level analysis.

If the distribution of the performance metric and/or the design limits are known (e.g. Gaussian) these values can be easily obtained from the statistics of the distribution. In general, the distribution of a system or model output is almost never known exactly, even when the inputs are on clearly defined distributions. In this case, response values may be obtained from a cumulative distribution function (CDF)

formulation of the output. This is the typical approach when considering problems under a pure aleatory analysis or under mixed uncertainty where the outputs carry some probabilistic representation. Note also that the "min" and "max" subscripts in Eqs. (34) and (35) indicate the response value that should be selected when multiple response values exist at a single probability level. For instance, this occurs when a model or system is subject to mixed uncertainty as mentioned in Section 3, which creates a range of values at each probability level defined by multiple CDFs (i.e., the CDFs that form the probability-box.)

Another type of uncertainty representation of either the design or the limits may be the non-probabilistic or pure epistemic representation. In this case, there is no distribution of the output and the uncertainty is only defined by an interval. Here the approach is to use the interval bounds as the measurement point for determining the margins rather than a response value defined at a specific probability level, which is not possible in this case. Note that this will be the most conservative approach and may be warranted given the unknown behavior of the uncertainty of epistemic intervals.

One of the objectives of this study is to demonstrate how a QMU analysis can be performed when the output uncertainty of design points and operational limits are different. The three possibilities include pure epistemic (interval), pure aleatory, and mixed uncertainty. Eqs. (34) and (35) can be generalized to Eqs. (36) and (37), where each term is based on the representation of the uncertainty of the specific component of the system. The possible values of the M_{UP} and M_{LW} are summarized in Table 8.3.

$$M_{UP} = |M_{UP1} - M_{UP2}| \tag{36}$$

$$M_{LW} = |M_{LW1} - M_{LW2}| \tag{37}$$

Table 8.3. Response Values of Different Uncertainty Representations for Margin Calculations

Uncertainty Representation	$M_{UP1}(FU)$	$M_{UP2}(F)$	$M_{LW1}(F)$	$M_{LW2}(FL)$
No Uncertainty	FU	F	F	FL
Pure Epistemic	FU_{min}	F_{max}	F_{min}	FL_{max}
Pure Aleatory	$(FU)_{P=\frac{1-\beta}{2}}$	$(F)_{P=\frac{1+\beta}{2}}$	$(F)_{P=\frac{1-\beta}{2}}$	$(FL)_{P=\frac{1+\beta}{2}}$
Mixed	$(FU_{min})_{P=\frac{1-\beta}{2}}$	$(F_{max})_{P=\frac{1+\beta}{2}}$	$(F_{min})_{P=\frac{1-\beta}{2}}$	$(FL_{max})_{P=\frac{1+\beta}{2}}$

8.4. CERTIFICATION PREDICTION

The QMU methodology can also be used as a tool for predicting if designs can pass specified certification criteria. In order to predict the certification plausibility of a particular configuration a process capability analysis may be employed [72]. The objective of this analysis is to compare the performance of a process, or in this case the performance metrics, against performance specifications or limits (i.e., certification values). Several factors must be considered, including a margin, measured between a performance metric and a certification value, as well as the uncertainty in a performance metric. For a probabilistic representation of the uncertainty in a particular performance metric, any margin measurement will also carry a probability. Figure 8.2 illustrates how a margin can be determined from a P-box obtained after the propagation of mixed uncertainty (see Section 3). Notice that the margin is measured between highest response value at a selected probability level or requirement (e.g., 95% confidence level) and the certification value. A positive margin, shown in Figure 8.2(a), would exist when the response value (at the probability requirement level) is less than the certification value. On the other hand, if the response value is greater

than the certification value, as in Figure 8.2(c), the margin would be negative and may indicate the design would not pass certification.

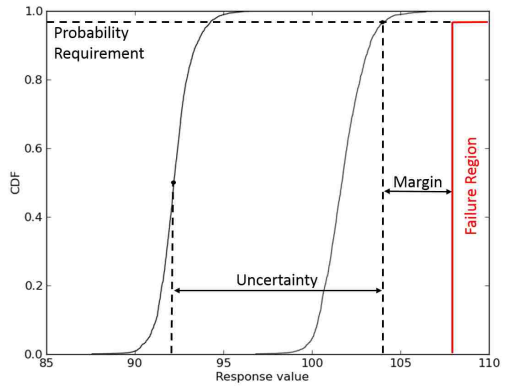

(a) Large Positive Margin

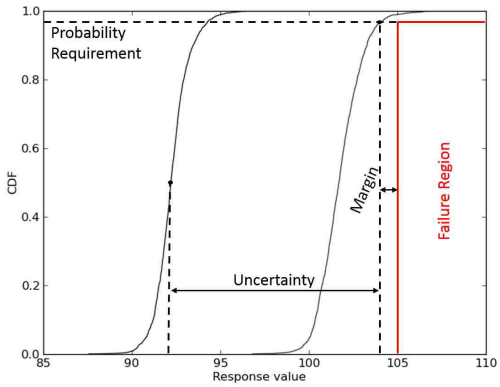

(b) Small Positive Margin

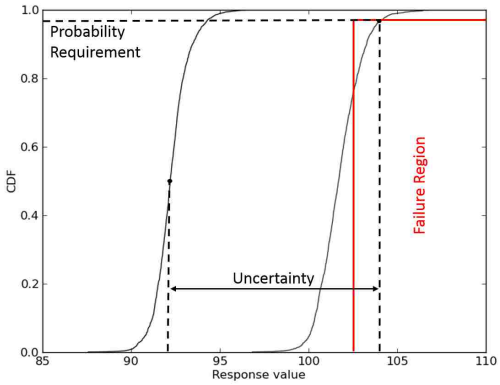

(c) Negative Margin

Figure 8.2. Certification Predication Margin and Uncertainty Measurements

Because a probability level or requirement is used as part of the margin measurement, there is a possibility that the margin may be positive, even if the boundary of the P-box hangs over the "Failure Region" of the certification value, as shown in Figure 8.2(b). While the margin is positive, the reliability of the configuration performance may be in question. Accounting for this uncertainty is desirable for a reliable design and accurate certification prediction. Using the QMU

methodologies discussed in this section, the confidence ratio, CR, and shown in Eq. (29), between the margin and the uncertainty may be used as a reliability measure in the certification prediction.

8.5. APPLICATION PROBLEMS FOR QMU

To demonstrate the QMU methodologies using stochastic expansions with various uncertainty representations between the design points and performance limits, two multi-system model problem are investigated. The first is a model of a spacecraft reentry trajectory coupled with models for heat flux prediction and bank angle modulation. The second problem is a multi-system model used to predict sonic-boom loudness of low-boom, supersonic vehicle configurations.

8.5.1. Spacecraft Reentry Trajectory Uncertainty. The first model is a multi-system, physics-based model for atmospheric, lifting entry of a spacecraft. Systems within the design include a model for six-degree of freedom reentry dynamics used for the determination of a reentry trajectory. The second system is a prediction model of stagnation point, convective heat flux used to determine the maximum heat load experienced along the reentry trajectory. In this problem, a generic planetary entry capsule similar to Crew Exploration Vehicle (CEV) was analyzed for a lunar return mission [73, 74, 75]. The purpose of this model is demonstrate the QMU of a coupled, multi-system design possessing mixed uncertainty, as well as performance boundaries with different types of uncertainty representation.

The deterministic model is shown in the system diagram in Figure 8.3. This model consists of two primary systems with three outputs or performance metrics.

The first system has two primary components or subsystems. The first of these is the trajectory model consisting of a six degree of freedom model for atmospheric entry of a lifting body. The kinematics are shown in Eqs. (38) though (41) and the equations of the dynamical system are shown in Eqs. (42) through (44) [76, 77].

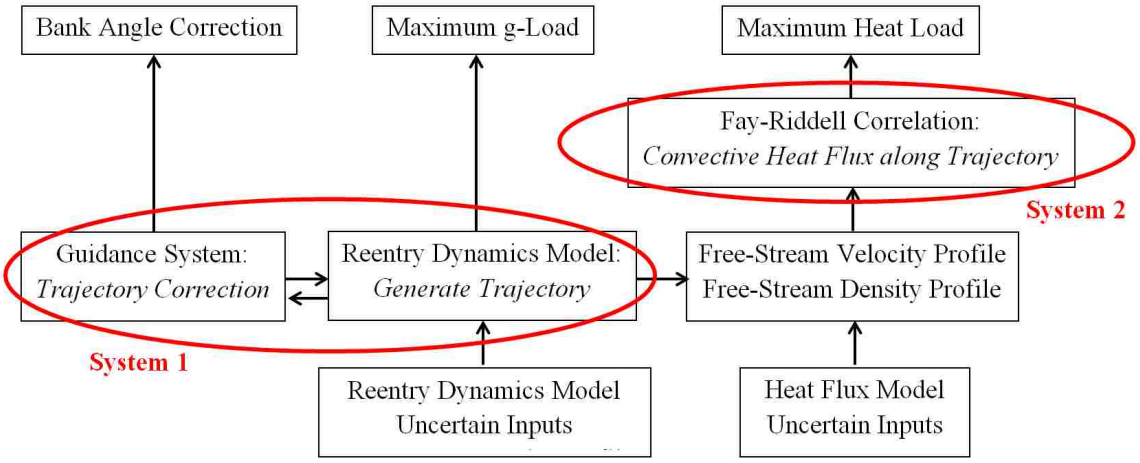

Figure 8.3. System Design Schematic for the Spacecraft Reentry Model Problem

$$\frac{dr}{dt} = V \sin\gamma \tag{38}$$

$$\frac{d\phi}{dt} = \frac{V \cos\gamma \cos\psi}{r} \tag{39}$$

$$\frac{d\theta}{dt} = \frac{V \cos\gamma \sin\psi}{r \cos\phi} \tag{40}$$

$$\frac{ds}{dt} = V cos\gamma \tag{41}$$

$$\frac{dV}{dt} = -\frac{D}{m} - g \sin\gamma + \omega^2 r \cos\phi(\sin\gamma \cos\phi - \cos\gamma \sin\phi \cos\psi) \tag{42}$$

$$V\frac{d\gamma}{dt} = \frac{L}{m}\cos\sigma - g\cos\gamma + \frac{V^2}{r}\cos\gamma + 2\omega V \cos\phi \sin\psi + \omega^2 r \cos\phi(\cos\gamma \cos\phi + \sin\gamma \sin\phi \cos\psi) \tag{43}$$

$$V\frac{d\psi}{dt} = \frac{L\sin\sigma}{m\cos\gamma} + \frac{V^2}{r}\cos\gamma\sin\psi\tan\phi - 2\omega V(\tan\gamma\cos\phi\cos\psi - \sin\phi) + \frac{\omega^2 r}{\cos\gamma}\sin\phi\cos\phi\sin\psi \tag{44}$$

In this system, V is velocity, m is mass, D is drag, L is lift, r is the orbital radius, γ is the flight path angle, θ is the longitude, ϕ is the latitude, σ is the bank angle, ω is the planetary body rotational speed, ψ is the heading angle, and s is the range. This is a system of 7 ordinary differential equations that can be numerically integrated simultaneously in time. An example trajectory for a typical lunar return skip reentry mission is shown in Figure 8.4.

The second component of this system is a guidance system, coupled to the primary reentry trajectory model. The guidance system is used to correct the trajectory in the instance of deviation from a nominal trajectory, such as when the reentry is subject to perturbation or uncertainty. In order to correct the trajectory, the guidance system uses a search algorithm to modify the bank angle of the trajectory. This effectively changes the direction of the lift vector in order the steer the spacecraft towards a target landing location. In this model problem, the reentry trajectory begins with the bank angle on the nominal value for the baseline trajectory. A single bank angle correction is performed when a sensible atmosphere is detected which occurs approximately when the g-load reaches a value of 0.05 [78]. The necessary bank angle correction is determined using a simple root finding method, shown in Eq. (45) for the i^{th} step in the search. The search is based on the distance between the target location and the projected landing location at the current bank angle shown in Eq. (46), which is only a function of the bank angle as no other control is being simulated.

$$\sigma_i = \sigma_{i-1} - \frac{\sigma_{i-1} - \sigma_{i-2}}{f(\sigma_{i-1}) - f(\sigma_{i-2})} f(\sigma_{i-1}) \tag{45}$$

where,

$$f(\sigma) = s_{miss} = s_{current} - s_{target} \tag{46}$$

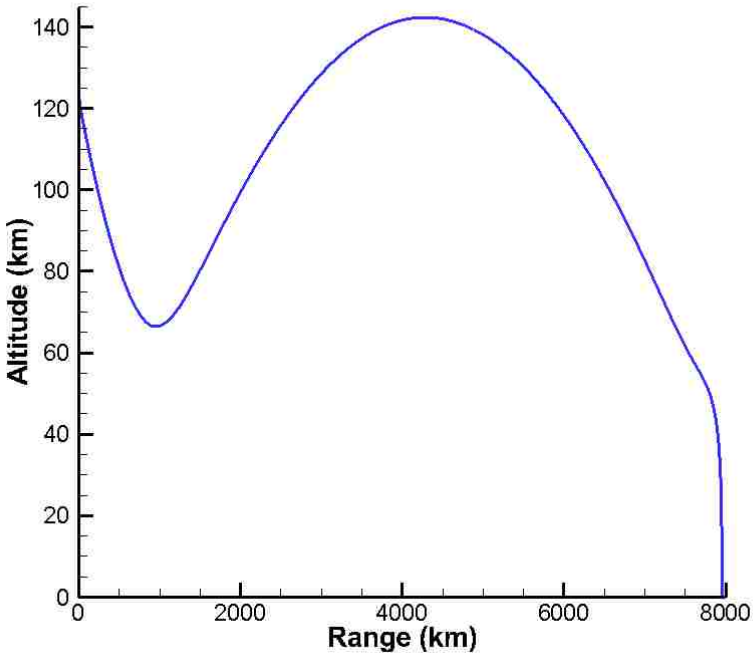

Figure 8.4. Sample Skip Reentry Trajectory

Here, $s_{current}$ is the range traveled with the current bank angle obtained from integrating the above dynamical system and s_{target} is the range to the target from the current location measured as a greater circle distance. Once the optimum bank angle is determined, the baseline bank angle is corrected instantaneously and the remainder of the trajectory is carried out.

In the reentry dynamics system, there are a total of two outputs. The first is the maximum g-load experienced along the trajectory. This is a critical trajectory and vehicle design value as it directly influences the safety of the crew as well as the structural loads that the vehicle may experience. The second output is the required bank angle correction. This value may be critical in the design of an adequate reaction control system including propulsive capabilities and propellant requirements [79].

The second system in this model is a model for the stagnation point, convective, heat flux of a blunt body in hypersonic flow. The Fay and Riddell [36] correlation was used to approximate the stagnation point heat transfer for a blunt body in hypersonic flow. This model assumes a laminar boundary layer, thermo-chemical equilibrium flow, and a fully catalytic wall. The model is shown in Eq. (19). Details of this model are given in Section 6.2.1.

For system 1, performance limits exist for both outputs. The maximum g-load is constrained by the limits the crew and the structure of the spacecraft can withstand meaning that only an upper limit exists. In order to represent this limit, an epistemic interval has been utilized. The performance limits of the bank angle correction would be based on the control and propellant limitations of the spacecraft. In this study, the upper and lower limits are firm boundaries, with no uncertainty. For system 2, there is only an upper limit on the heat flux as any lower limit would not be a concern. In this case, the upper limit was represented by an epistemic interval. This interval was selected to reflect the physical limitations of current TPS materials.

In system 1 there is a total of 10 uncertain variables, both coming from epistemic and aleatory sources. Epistemic sources include entry interface (E.I.) altitude, mass, drag coefficient and lift coefficient. Aleatory sources include E.I. velocity, E.I. flight path angle, the reference area, E.I. latitude, E.I. longitude, and E.I. heading angle. The uncertainty in these parameters and their distribution are shown in Tables 8.4.

Note that many of the selected uncertain parameters and classification are consistent with previous uncertainty work in this area [73, 74, 76, 77].

For system 2, 10 variables were selected as sources of uncertainty. Both epistemic (model form) and aleatory (inherent) forms of uncertainty were considered. The epistemic uncertain variables were as follows: Lewis number, Prandtl number, boundary layer edge viscosity, emissivity, the heats of formation for nitrogen and oxygen and the power over the Lewis number. These model variables are considered as epistemic by imposing uncertainty on them due to lack of knowledge. Note that uncertainty in the two heats of formation and the boundary layer edge viscosity were modeled through the introduction of a factor, k, to each variable, which was used to represent a variation in the uncertain variable (e.g. $x = k\ (x_{ref})$.) The factor k for each variable was treated as an epistemic uncertain variable. The other three variables were treated as aleatory (inherent) uncertain variables: free stream velocity, free stream density, and the radius of curvature of the body. Random fluctuations in the free-stream conditions are possible during flight and variations in the vehicle geometry are possible due to manufacturing processes. These variables were assumed normally distributed about some mean with a coefficient of variance (CoV) of 1%. The input uncertainties for each of the uncertain variables are summarized in Table 8.5.

For system 1, the upper performance limit is represented by an epistemic interval as stated in the previous section. The g-load limit was selected to be on the interval [10 , 11] g. Also for system 1, the limitations of the bank angle correction are defined as boundaries with no uncertainty. The boundaries were elected to be ± 20 deg. For system 2, the epistemic interval was selected to be [900 , 1200] W/cm^2. The uncertainty in this interval was extrapolated from several sources indicating different heat load values of the stardust mission including CFD simulations as well as sensor data collected during flight [80, 81, 82].

Table 8.4. Reentry Model Uncertain Parameters for System 1

Variable	**Distribution**	**Mean/ Min**	**Std./ Max**
E.I. h, m	Epistemic	121800	122000
m, kg	Epistemic	9000	9500
C_D	Epistemic	1.27	1.31
C_L	Epistemic	0.367	0.407
E.I. U_∞, m/s	Gaussian	10900	30.0
E.I. γ, deg.	Uniform	-6.1	-5.9
S, m^2	Gaussian	19.9	0.2
E.I. ϕ, deg.	Gaussian	0.0	1.0
E.I. θ, deg.	Gaussian	0.0	1.0
E.I. ψ, deg.	Gaussian	0.0	1.0

Table 8.5. Reentry Model Uncertain Parameters for System 2

Variable	**Distribution**	**Mean/ Min**	**Std./ Max**
Le	Epistemic	1.358	1.442
Pr	Epistemic	0.679	0.721
μ_e Factor	Epistemic	0.97	1.03
ϵ	Epistemic	0.776	0.824
h_f^0 (N) Factor	Epistemic	0.97	1.03
h_f^0 (O) Factor	Epistemic	0.97	1.03
Power on Le	Epistemic	0.5044	0.5356
U_∞ Factor	Gaussian	1.0	0.01
ρ_∞ Factor	Gaussian	1.0	0.01
R_n, m	Gaussian	6.93	0.0693

Performing the UQ in the system design condition and the performance limits is the next step in the analysis. From the previous section, there is a total of 20 uncertain parameters in this model problem. Using Eq. (2), 462 evaluations of the deterministic model were required for an OSR=2 with second order polynomial chaos

expansions. The upper and lower CDFs of the output P-Boxes are given in Figures 8.5 and 8.6 for the g-load and bank angle correction, respectively. Note that these were obtained using the sampling approach for mixed uncertainty outlined in Section 3.

A similar analysis was performed on system 2 of the design. A stochastic response surface could be formulated using a second order polynomial chaos expansion. The upper and lower CDFs of the output P-Box are given in Figure 8.7, which were obtained using the sampling approach for mixed uncertainty outlined in Section 3.

In the previous model problem, a comparison of Monte Carlo and NIPC results was made in order to confirm the accuracy of the NIPC response surfaces. This was possible because of the low computational cost of the model. The reentry dynamics model is significantly more computationally expensive making an accurate Monte Carlo solution infeasible to obtain. However, checking the accuracy of the surrogate model is still possible by comparing results obtained from the actual model to those obtained from the surrogate model at the same sample location in the design space. In this study, 20 sample points, distributed evenly in the design space, were used to measure the accuracy of the surrogate models. Of the three surrogates created in this model problem, the highest mean error in the sample points was about 0.2% validating the selection of second order polynomial chaos expansions. Note that these sample points differ from the sample points used to train the surrogate model.

In the performance limits, no uncertainty quantification was performed on the performance limits for this model as both models were assigned epistemic intervals or boundaries with no uncertainty.

After assessing the uncertainty in the components of the system, performing the QMU analysis is now possible. A 95% confidence analysis (i.e., $\beta = 0.95$) has been selected for this problem. Using the equations and tables given in earlier in this section, the margin calculations can be performed. For system 1, both the

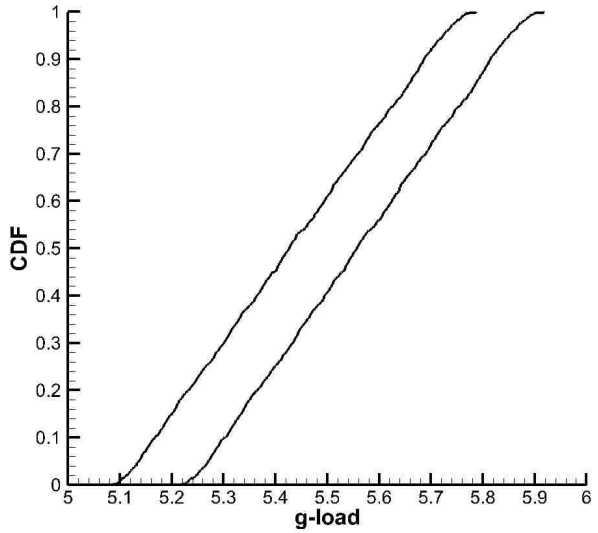

Figure 8.5. Maximum g-Load P-Box Plot from System 1

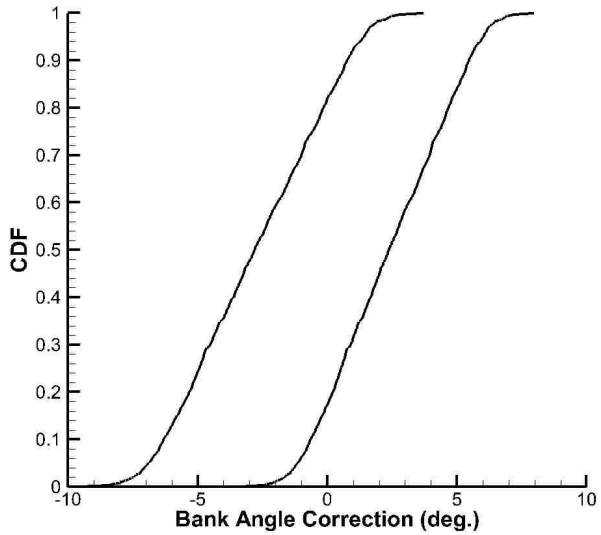

Figure 8.6. Bank Angle Correction P-Box Plot from System 1

design metrics are represented by mixed uncertainty. The upper performance limit of the maximum g-load was represented by an epistemic interval while the upper

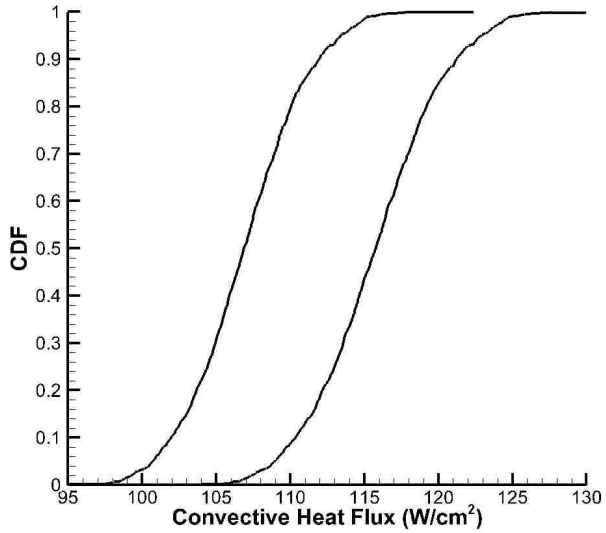

Figure 8.7. Maximum Heat Load P-Box Plot from System 2

and lower bounds of the bank angle correction were fixed values with no uncertainty. A summary of the margin and performance gate uncertainty values as well as the resulting confidence ratios of the system are given in Tables 8.6 and 8.7. Note that the minimum of these two confidence ratios is deemed the confidence ratio for the system.

Table 8.6. Maximum g-Load QMU Analysis Metrics from System 1

Performance Gate	**Margin**	**Uncertainty**	**CR**
Upper	4.13	0.67	6.17

Similarly, the QMU analysis is performed on system 2. Here, the design is represented by mixed uncertainty while the only performance limit is represented by

Table 8.7. Bank Angle Correction QMU Analysis Metrics from System 1

Performance Gate	Margin	Uncertainty	CR
Lower	12.61	9.77	1.29
Upper	13.67	9.14	1.50

an epistemic interval. A summary of the margin and performance gate uncertainty values is shown in Table 8.8 as well as the resulting confidence ratio of the system.

Table 8.8. Maximum Heat Load QMU Analysis Metrics from System 2

Performance Gate	Margin	Uncertainty	CR
Upper	775.92	150.98	5.14

There are two resulting confidence ratios from the QMU analysis, one from each system. A system wide confidence level would then be the minimum of these three ratios shown to be 1.29. This value indicates the weakest system in the design; however, in this case, the margins are greater than the uncertainty and the system design may be acceptable. If not, this would indicate that a re-analysis/design of the system, the performance limits, or both may be necessary to improve the reliability of the system.

8.5.2. Certification Prediction of Supersonic Low-Boom Configurations. The second problem is a high-fidelity CFD model of sonic booms produced by low-boom configurations. The objective is to quantify the uncertainty in ground-level noise predictions and demonstrate how QMU can be used

to assess certification prediction of multiple configurations. Analysis of sonic booms starts with capturing the pressure signature produced near the vehicle (the near-field) and then propagating that signature to the ground level. Multiple uncertainties come from various sources within the CFD and propagation models. The remainder of this section gives the details on the deterministic model, the stochastic problem, and discusses the application and findings of the QMU methodologies.

The near-field domain includes the vehicle and a region extending multiple body lengths away from the aircraft. The goal is to resolve the near-field pressure signature, parallel to the flow direction, that is generated by the body in supersonic flow. An example of this is shown in Figure 8.8. This signature is then propagated to ground level using a high fidelity propagation code called sBOOM [83]. This simulates how the signal will change while passing through the atmosphere. Once a final ground signature is predicted, output quantities of interest, such as perceived loudness (PLdB) and C-weighted sound exposure level (CSEL), are evaluated and may serve as design and certification metrics. The remainder of this section gives further detail regarding the CFD simulations and the propagation model.

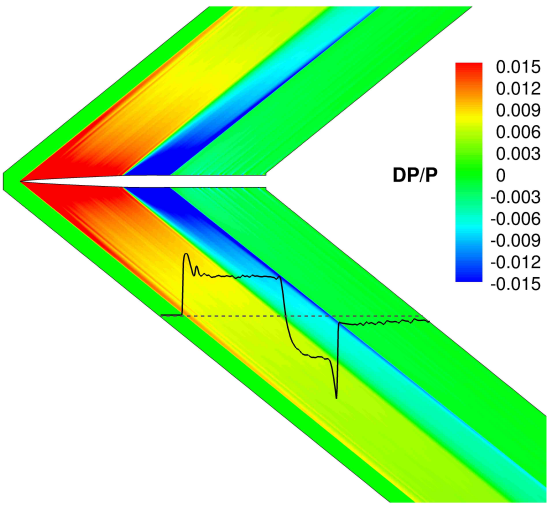

Figure 8.8. Near-Field CFD Domain with Pressure Signature

This study employed the Fully Unstructured Navier-Stokes Three-Dimensional (FUN3D)[84] flow solver for CFD analysis of low-boom configurations. FUN3D contains many tools for design optimization and analysis and was developed and is maintained at the NASA Langley Research Center. The code employs the finite volume formulation and stores flow field variables at the control volume nodes. FUN3D can handle aerodynamic simulations across a large range of Mach numbers from the subsonic to hypersonic regimes and has been used extensively for the analysis of sonic boom prediction [85, 86, 87].

All cases investigated in this study were assumed to be at steady state. Often, the Euler equations are solved in place of the full Navier-Stokes equations for high Reynolds number, aerodynamic flows by assuming the flow is inviscid. While this is a known simplification of the actual flow physics, this assumption allows for computational savings when investigating large-scale-complex problems or when large numbers of simulations are needed, such as when performing UQ. However, low-boom configurations may be designed to exploit viscous effects, which smear or dampen shocks. This would be overlooked when using an Euler assumption. In the current study, both inviscid and viscous, fully turbulent cases were explored. When solving the Euler equations, the inviscid fluxes were calculated at cell edges by employing the van Leer scheme to solve an approximate Riemann problem. For viscous cases, the inviscid fluxes are calculated by the Roe scheme for the approximate Riemann problem, if possible. In order to aid convergence, the viscous simulations of the LM-1021 and 69° Delta wing required the use of the dissipative Low Diffusion Flux Splitting scheme. For modeling the turbulence, the one equation Spalart-Allmaras [88] model was employed for computational efficiency and robustness.

The configurations of interest (SEEB-ALR, 69° Delta Wing, and the LM 1021-01) are shown in Figure 8.9. The SEEB-ALR model is described by Morgenstern et al.[89] and the 69° Delta Wing is discussed by Hunton et al. [90]. The LM 1021-01

low-boom configuration is detailed by Morgenstern et al. [91]. The discussion of the physical models, their origins, and design specific details are left to these studies.

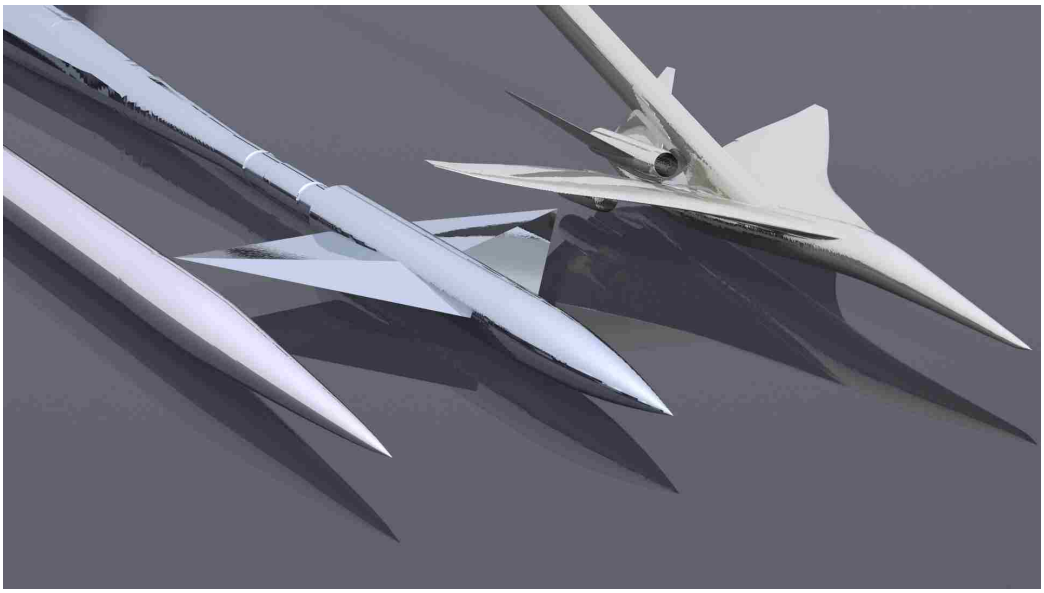

Figure 8.9. Configurations Studied in the Present Work. SEEB-ALR (left), NASA 69° Delta Wing (center), LM 1020-01 (right). Models Not to Relative Scale.[1]

The inviscid SEEB-ALR and inviscid Delta Wing grids were the same grids made available for the 2014 AIAA Sonic Boom Prediction Workshop. The SEEB-ALR and Delta Wing models began as STEP files and a solid representation was extracted. Then, a triangular surface mesh and tetrahedral volume mesh were generated using GridEx [92]. The core grid was then extruded using the Inflate method [86] in a direction aligned with the Mach angle so the relevant pressure signatures can be captured without wasting points in regions which are not influenced by the aircraft. Full details on the SEEB-ALR and 69° Delta Wing solid models, grids, and grid generation techniques for near-field sonic boom CFD are given in Park et al. [86]. A

cross section showing both the core grid and part of extruded region for the Delta Wing model is included in Figure 8.10.

One point of interest is that two versions of the SEEB-ALR solid model exist: the as-built and the as-designed. The as-designed geometry has a perfectly smooth surface, but the as-built model used in the wind tunnel testing possessed many surface imperfections as shown in Figure 8.11. These flaws are reflected in the near-field signature, which are shown later in this section. One objective of this study will be to quantify the effect of the surface imperfections on the loudness quantities of interest in this study.

Table 8.9 summarizes the grid sizes for each model. In general, viscous grids needed to be much more refined. Coupled with the turbulence model, viscous cases took 5-10 times longer to converge than the Euler cases. This is especially significant for the LM-1021. All cases were run in parallel over 192 processors.

Table 8.9. CFD Grid Dimensions and Computational Time demands

Model	**Cells**	**Nodes**	**Solution Time**
SEEB-ALR Euler	7.83e+06	2.89e+06	20 min
SEEB-ALR Viscous	3.64e+07	6.20e+06	1.3 hrs
69° Delta Wing Euler	2.24e+07	5.36e+06	10 min
69° Delta Wing Viscous	7.80e+06	2.90e+06	2 hrs
LM 1021-01 Euler	3.38e+07	8.37e+06	30 min
LM 1021-01 Viscous	7.24e+07	2.45e+07	5 hrs

To lessen the computational burden of the multiple CFD evaluations required for the UQ analysis, baseline cases with unperturbed parameter values were completed for each vehicle. These were then restarted for each random sample vector within the stochastic parameter space. For every configuration, this resulted in fewer iterations

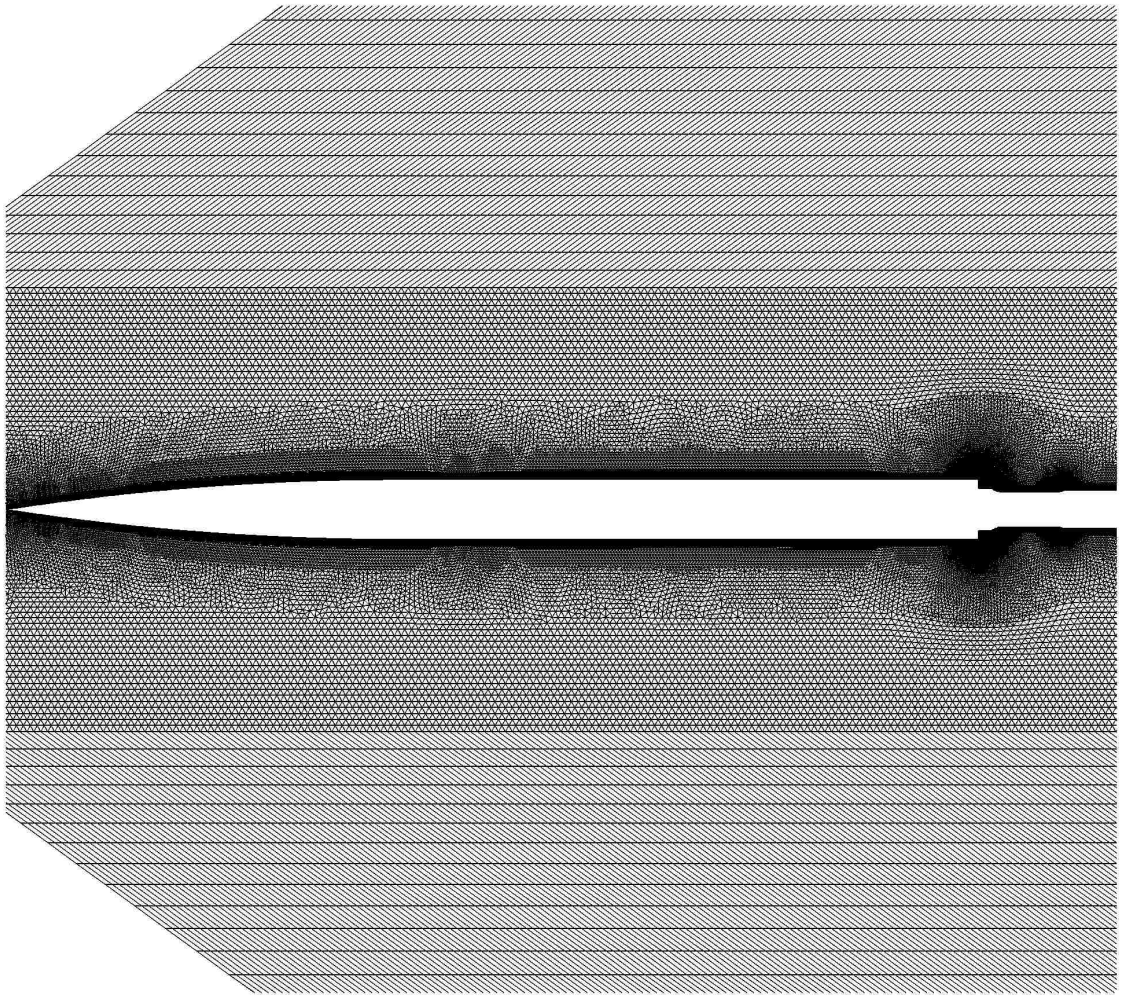

Figure 8.10. Computational Grid for the Viscous 69° Delta Wing Including Extruded Region

to achieve convergence compared to a completely new solution. This was especially significant for the LM-1021.

After obtaining the near-field pressure signature from the CFD model, it can then be propagated to the ground using a program called sBOOM. This model uses an augmented Burgers equation to propagate the near-field pressure signature to the ground level. The model takes into account nonlinear effects, thermoviscous absorption, atmospheric stratification, spreading, and many other

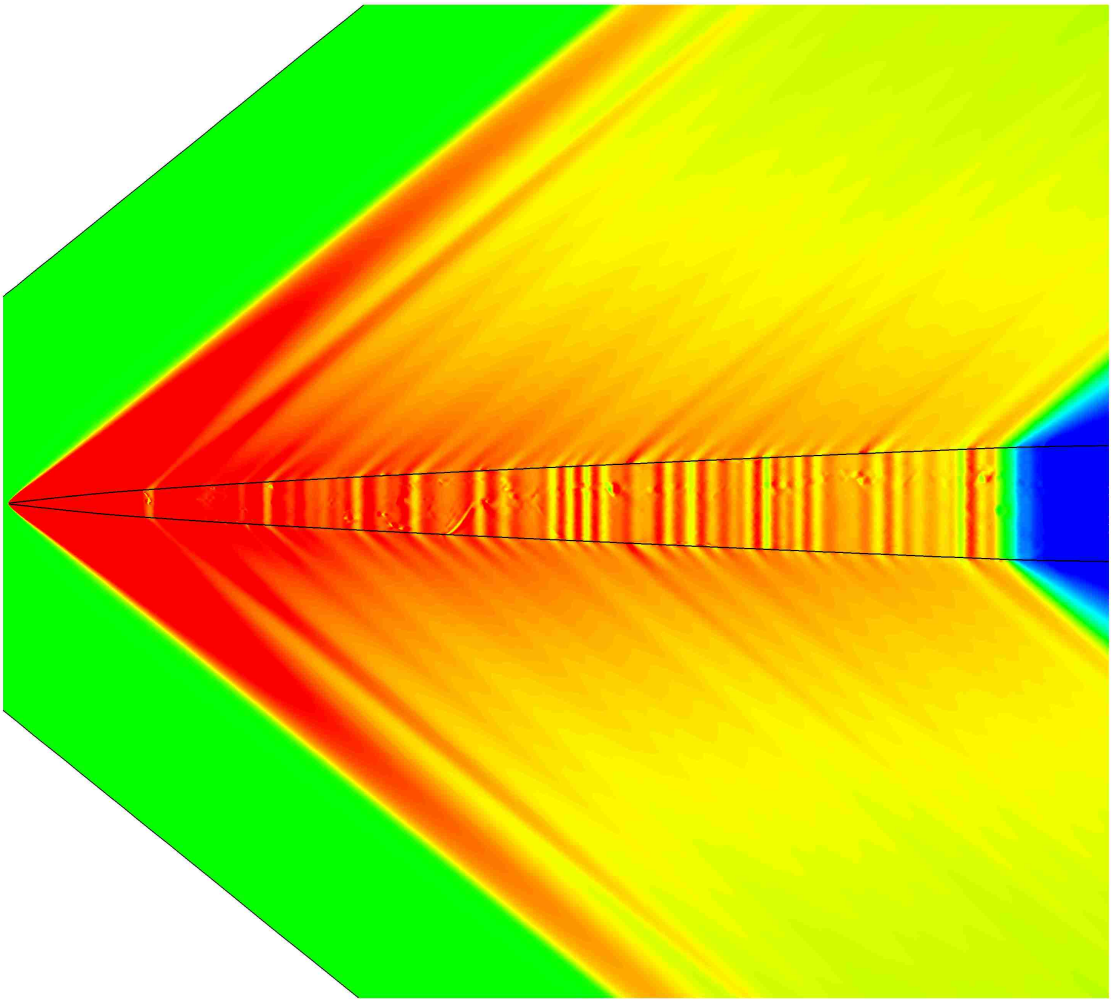

Figure 8.11. SEEB-ALR Surface Imperfections of the as-Built Model

molecular relaxation phenomena. Further details regarding this model are given by Rallabhandi [93].

One of the most critical steps in any uncertainty analysis is the identification and classification of the input uncertainties of the models. In this study, the deterministic model is decomposed into two parts. First, for the CFD model, two input uncertain parameters were identified as possible sources of uncertainty: Mach number and angle of attack. The type and amount of uncertainty are shown in Table 8.10. Note that these parameters were determined to be aleatory parameters given their possible

inherent nature. Small fluctuations in these parameters are typically unavoidable, but well characterized. For the Mach number, two mean values are considered for comparison with the experimental data. The SEEB-ALR and LM 1021-01 configurations were tested at Mach 1.6, while the Delta Wing was tested at Mach 1.7.

Table 8.10. CFD Aleatory Input Parameters

Input	**Distribution**	**Mean**	**Std. Dev.**
Angle of Attack	Gaussian	0.0	0.1
Mach Number	Gaussian	1.6/1.7	0.0016

A second set of uncertain parameters were identified as coming from the propagation model, sBOOM [93]. This model contained a particularly large amount of uncertainty, both aleatory and epistemic, due to its complexity and the large number of tunable input parameters. The aleatory parameters, listed in Table 8.11 consist of two groups. The first is uncertainty in the atmosphere that may affect the propagation of the sonic boom signature as it travels from the vehicle near-field to the ground. The second group of parameters are those that may affect the shape of the signature due to changes in vehicle orientation and orientation rates. The measurement location or azimuth is also considered uncertain. In this study, only the on-track position, with uncertainty, is investigated.

As with the CFD uncertain parameters, the aleatory parameters are those that have been modeled, but random fluctuations may still occur. However, epistemic parameters, listed in Table 8.12, exist due to lack of knowledge of the correct modeling approach. The initial step size and signature propagation points parameters are adjustable sBOOM specific input parameters. The signature propagation points

Table 8.11. sBOOM Aleatory Input Parameters

Input	Distribution	Mean	Std. Dev.
Temperature Profile (%)	Gaussian	1.0	0.01
Humidity Profile (%)	Gaussian	1.0	0.01
Climb Angle (Deg.)	Gaussian	0.0	0.1
Azimuth (Deg.)	Gaussian	0.0	0.1
Turn Rate (Deg./s)	Gaussian	0.0	0.05
Climb Rate (Deg./s)	Gaussian	0.0	0.05

variable is related to the sampling frequency of the signal and may directly affect the accuracy of the loudness metrics from the integrated ground level signature. The number of points necessary for an accurate result may vary based on the signal length, signal shape, or the signal source (i.e., the configuration). Note also that the value of this parameter is both the number of points used within the propagation routine and the number of points in the final ground level signature that is analyzed to find the loudness measures. The other two parameters (reflection factor and ground level altitude) are considered epistemic uncertain parameters as they are not being modeled for a specific flight location. These parameters may vary significantly along a flight path.

Table 8.12. sBOOM Epistemic Input Parameters

Input	Min.	Max.
Initial Step Size	0.007	0.03
Reflection Factor	1.8	2.0
Ground Elevation (ft)	0.0	5000.0
Signature Propagation Points	20000	60000

In addition to the above uncertain input parameters, inviscid and fully turbulent CFD solutions were performed for all of the configurations analyzed in this study. The purpose of this is to quantify the effect of different modeling fidelities for the various low-boom configurations studied. Note that the amount of uncertainty in each parameter discussed above was the result of much discussion among the authors and other experts in the field.

1. SEEB-ALR Body of Revolution

The first step in the UQ process is to validate the CFD solution. Near-field signatures were taken at 21.2 inches from the body to coincide with experimental data. Comparison with the experiment is shown in Figure 8.12(a) for both as-built and as-designed geometries, and for both inviscid and fully turbulent flow assumptions. A residual scale plot of the signatures is shown in Figure 8.12(b). In this figure, the averaged experimental signature is treated as a reference and is subtracted off of the uncertainty bounds and the CFD signatures. Notice that there is good agreement between the experiments and the CFD results as the CFD signatures mostly lie within the bounds of the uncertainty in the experimental results. There are some differences in the peaks of the signatures, but the experimental results have rounded peaks due to the measurement approach [94]. This agreement is deemed to be acceptable and is assumed to validate the baseline numerical solution.

After validating the CFD model, the next step is to construct the surrogate model(s) that represent the design quantities of interest. In this study, PLdB and CSEL were considered. In total, there are 12 uncertain parameters, as discussed above. Using Eq. (2), 182 evaluations of the deterministic model were necessary to construct a second order PCE with twice oversampling. In evaluating the deterministic model, the first step is to obtain CFD solutions for the near-field pressure signatures. The dispersion of the deterministic samples for the Euler as-built case are shown in Figure 8.13(a). Figure 8.13(b) shows the same dispersion of

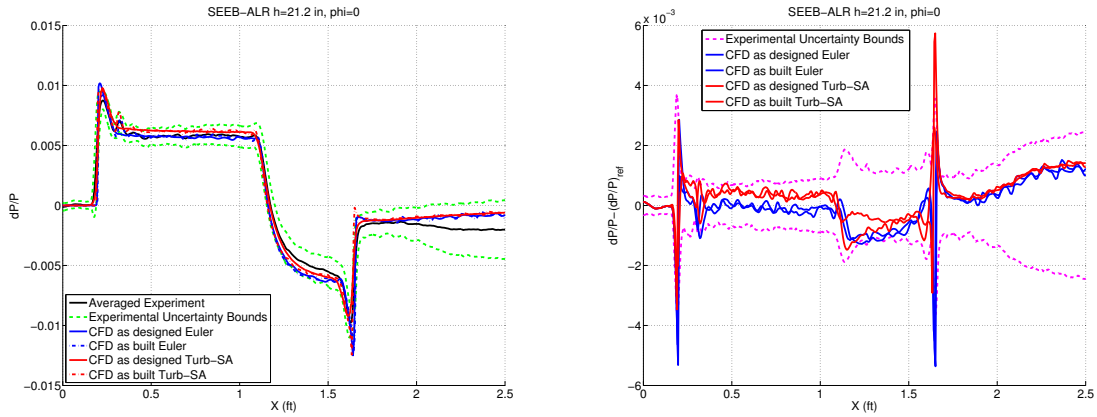

(a) Signatures (b) Residual Scale

Figure 8.12. SEEB-ALR Near-Field CFD Comparison with Experimental Results

signals, but shifted to reference location for better visualization of changes in signature amplitude.

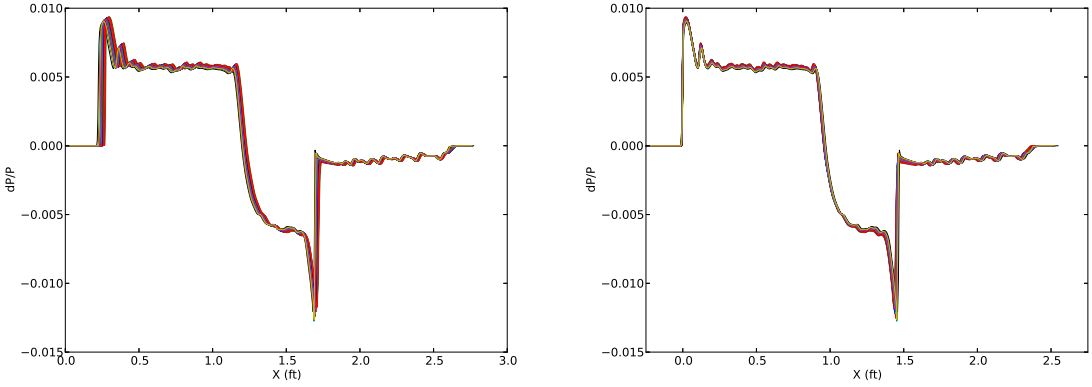

(a) Actual (b) Shifted

Figure 8.13. SEEB-ALR Euler as-Built Near-Field Pressure Signature Dispersion

The CFD signatures were then each propagated through sBOOM with the additional uncertainty that was identified for this model. For the Euler as-built case,

the resulting ground signature dispersion is shown in Figure 8.14(a) and shifted to a reference location in Figure 8.14(b). The ground signatures were then analyzed to produce the desired loudness quantities of interest.

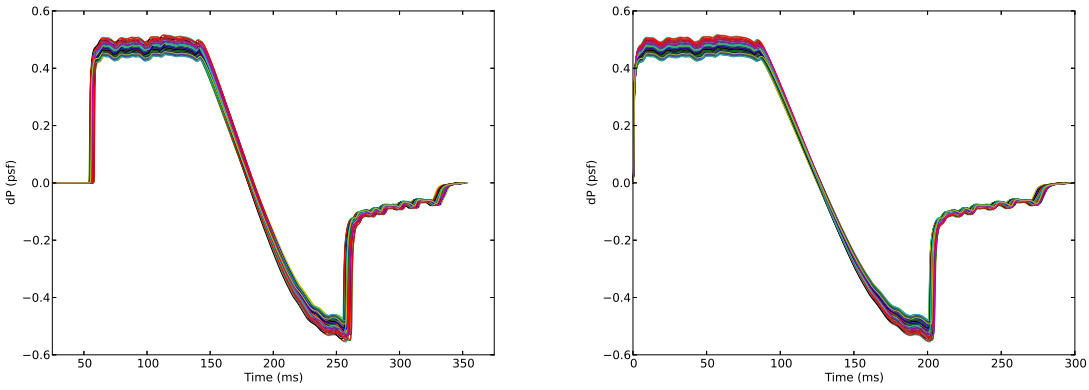

(a) Actual (b) Shifted

Figure 8.14. SEEB-ALR Euler as-Built Ground Signature Dispersion

Similar dispersions of the near-field and ground level signatures can be generated for the other three cases investigated for this model (Euler as-designed, turbulent as-built and turbulent as-designed). While not shown here, these dispersions are similar to those shown for the Euler as-built case.

Note that for most of the CFD models, the signatures do not recover fully. This can stem from the inclusion of the mounting system used within the wind tunnel in the computational geometry and/or the truncation of the computational domain. For more accurate results and to eliminate any numerical instabilities within the propagation routine/loudness measure calculations, the ends of the signatures are forced to zero and additional zero padding is added to the signatures for all of the configurations in this study.

At this point, the surrogate models for the output quantities of interest can be created by solving the linear system of equations given in Eq. (3). Measuring the accuracy of the surrogate models across the design space can be done by sampling a set of test points in the design space and comparing outputs from the deterministic model with the outputs from the surrogates at the same sample locations. Twenty new samples were taken to measure the accuracy of the surrogates. The average error at these twenty test points was determined to be less than 0.03% for all of the geometry/flow type/loudness quantity combinations indicating the selection of a second-order PCE was sufficient. Note that these test points are different from those points used to train the surrogate models and are distributed evenly throughout the design space with a Latin Hypercube sample structure.

With the surrogate models constructed and validated, the uncertainty can be propagated through the surrogates using the second-order probability analysis outlined in Section 3. This was done using the sampling approach using 2000 epistemic samples and 1600 aleatory samples (3.2×10^6 samples total), resulting in the family of 2000 CDFs. For the Euler as-built case, the boundaries of the P-boxes are shown in Figure 8.15(a) and Figure 8.15(b) for PLdB and CSEL, respectively.

A significant amount of information can be taken from P-boxes, including confidence intervals. For the case of mixed uncertainty, one approach to obtaining the 95% confidence interval, for example, is to take the upper 97.5% probability level and the lower 2.5% probability level as the interval. A summary of the 95% confidence intervals is shown in Table 8.13 for all of the models, subject to the uncertainty identified in this study.

From these results, there is a difference between the ideal as-designed geometry and the actual as-built model. The imperfections in the surface cause an increase in the PLdB level. In the case of CSEL, the same trend is not as severe, but still present. An additional conclusions is that the effect of an inviscid versus the fully turbulent

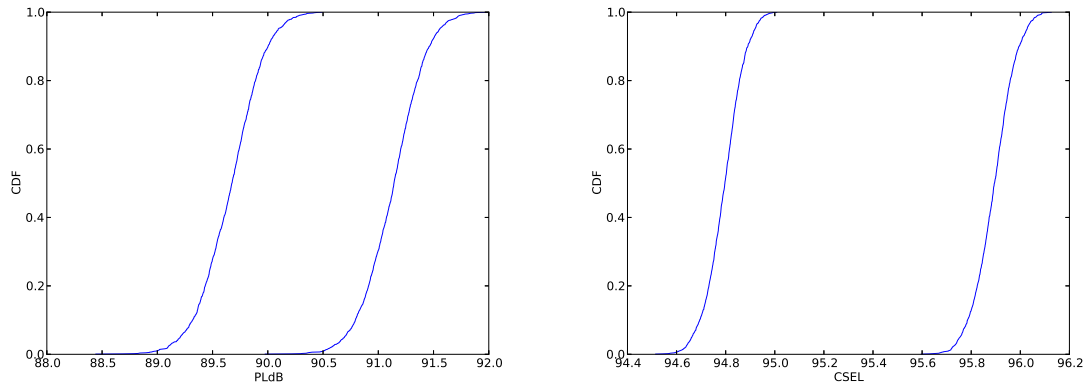

(a) PLdB (b) CSEL

Figure 8.15. SEEB-ALR Euler as-Built PLdB and CSEL Probability Box Boundaries

Table 8.13. SEEB-ALR 95% Confidence Intervals

Configuration	**PLdB**	**CSEL**
Euler as-Built	[89.12 , 91.63]	[94.64 , 96.05]
Euler as-Designed	[88.06 , 90.49]	[94.32 , 95.80]
Turbulent as-Built	[89.44 , 91.95]	[94.78 , 96.22]
Turbulent as-Designed	[88.98 , 91.61]	[94.75 , 96.20]

analysis is small and is less than that of the effect of the surface imperfections in the as-built geometry. For preliminary design and analysis, this indicates the use of the low fidelity solution may be acceptable when considering the added computational cost of a fully turbulent solution, for this configuration.

The final step in the analysis is to predict whether or not the design, under uncertainty, could potentially pass a certification based on the design quantity of interest. Currently, the actual certification value for low-boom configurations is unknown. However, the methodology described earlier in this section can be easily implemented for certification prediction. For example, if the certification requirement

was a PLdB of less than 100, the Euler as-built design would have a CR of 4.27 for a 95% confidence analysis. This may indicate that the margin is sufficiently larger than the uncertainty in the design.

A sensitivity analysis of the uncertainty parameters was performed to highlight which of the parameters contribute most significantly to the total uncertainty. The contribution of the top uncertain parameters to both PLdB and CSEL are given in Tables 8.14 and 8.15, respectively. For both metrics, the reflection factor appears to be the most dominate of the parameters considered. This is especially true for CSEL as the reflection factor contributes about 85 to 90% to the total output variance. For PLdB, a significant amount of uncertainty also arises due to the uncertainty in the atmospheric humidity profile. Loubeau and Coulouvrat [95] have shown that variation in the atmospheric humidity can significantly affect the sonic-boom rise time, which may affect the signature loudness.

Table 8.14. SEEB-ALR Top Uncertain Parameter Contribution to PLdB Total Uncertainty

Uncertain Parameter	**Euler as-Built**	**Euler as-Designed**	**Turbulent as-Built**	**Turbulent as-Designed**
Angle of Attack	4.7%	9.6%	2.4%	6.7%
Initial Step Size	1.6%	1.1%	1.7%	1.8%
Reflection Factor	46.4%	44.8%	45.9%	44.2%
Humidity Profile	38.3%	35.7%	41.6%	36.1%
Ground Elevation	7.9%	7.7%	6.8%	9.7%
All Others	<1%	<1%	<1%	<1%

2. NASA 69° Delta Wing

For the NASA 69° Delta Wing, near-field signatures were taken at 24.8 inches from the body to coincide with experimental data. Comparison with the experiment

Table 8.15. SEEB-ALR Top Uncertain Parameter Contribution to CSEL Total Uncertainty

Uncertain Parameter	**Euler as-Built**	**Euler as-Designed**	**Turbulent as-Built**	**Turbulent as-Designed**
Angle of Attack	3.6%	6.2%	4.5%	4.6%
Reflection Factor	88.2%	84.1%	86.5%	86.0%
Temperature Profile	2.2%	2.4%	2.4%	2.4%
Humidity Profile	1.7%	1.5%	1.7%	1.7%
Ground Elevation	4.1%	5.5%	4.6%	5.2%
All Others	<1%	<1%	<1%	<1%

is shown in Figure 8.16(a) for both inviscid and fully turbulent flow assumptions. A residual scale plot of the signatures is shown in Figure 8.16(b). The CFD signatures are in fairly good agreement with the experimental results as the signatures lie primarily within the bounds of the uncertainty in the experimental results. There is some rounding of the experimental results similar to the results of the SEEB-ALR model. This is due to model vibration and the instrumentation used during the wind tunnel testing [94]. However, given these small and expected differences, the baseline numerical solution is considered to be accurate and validated for the purposes of this study.

As above, surrogate models are constructed for the design quantities of interest, PLdB and CSEL. The number of uncertain parameters is the same as with the SEEB-ALR and, therefore, the deterministic model is evaluated 182 times to construct a second order PCE. The dispersion of the deterministic samples for the Euler case are shown in Figure 8.17(a). Figure 8.17(b) shows the same dispersion of signals, but shifted to reference location for better visualization of changes in signature amplitude. The resulting ground signature dispersion, for the Euler case, is shown in Figure 8.18(a) and shifted to a reference location in Figure 8.18(b). Similar dispersions

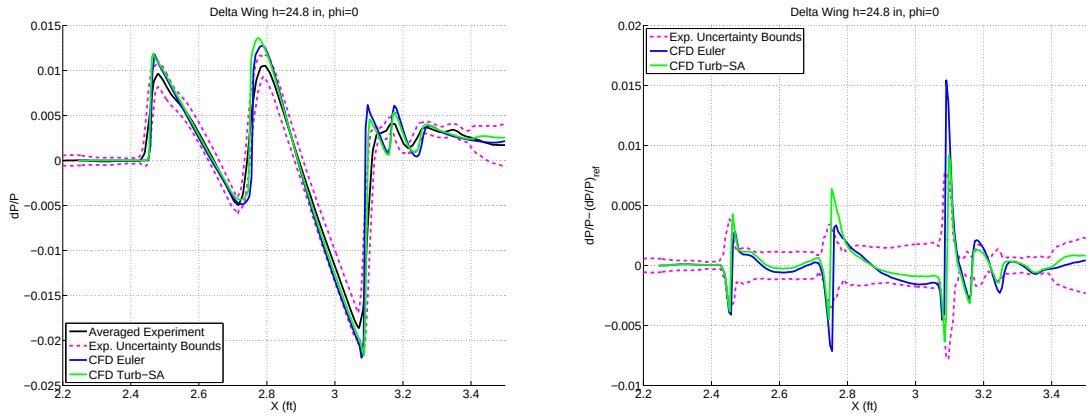

(a) Signatures (b) Residual Scale

Figure 8.16. 69° Delta Wing Near-Field CFD Comparison with Experimental Results

of the near-field and ground level signatures can be generated for the fully turbulent case. While not shown here, this dispersions are similar to those shown above for the Euler case.

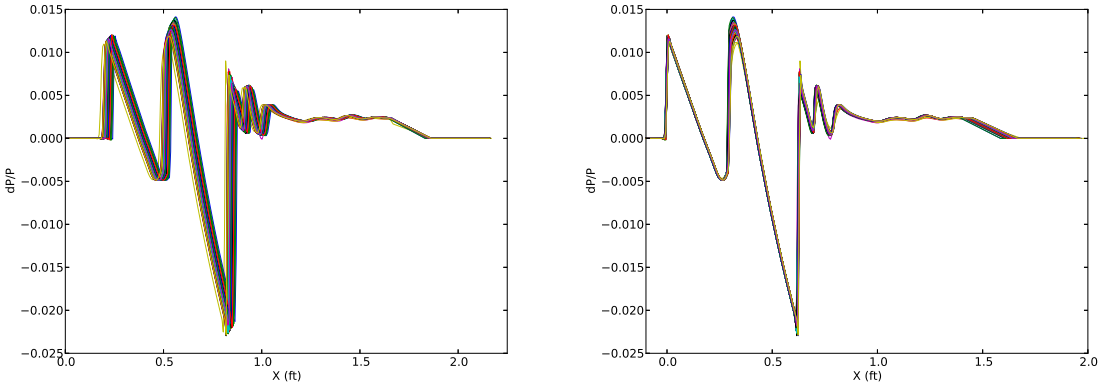

(a) Actual (b) Shifted

Figure 8.17. 69° Delta Wing Euler Near-Field Pressure Signature Dispersion

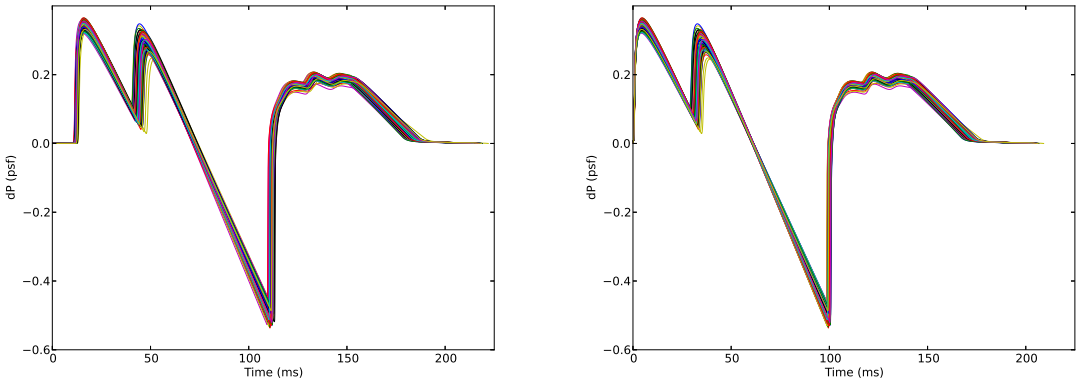

(a) Actual (b) Shifted

Figure 8.18. 69° Delta Wing Euler Ground Signature Dispersion

As with the SEEB-ALR, the accuracy of the surrogate model needs to be verified. The average error at these twenty test points was determined to be less than 0.4% for all of the flow type/loudness quantity combinations indicating the selection of a second-order PCE was sufficient. With the surrogate models constructed and validated, the uncertainty can be propagated through the surrogates using the second-order probability analysis outlined in Section 3. This was done using the sampling approach, resulting in the family of CDFs. For the Euler case, the boundaries of the probability boxes are shown in Figure 8.19(a) and Figure 8.19(b) for PLdB and CSEL, respectively.

A summary of the 95% confidence intervals for both Euler and Turbulent cases is shown in Table 8.16. From these results, the effect of an inviscid versus the fully turbulent analysis is slightly more significant compared to the SEEB-ALR model for both loudness measures. However, there is still less than a one PLdB and CSEL difference between the two levels of model fidelity. This may indicate that the use of a Euler analysis may be sufficient given the reduce computational cost over the fully turbulent analysis, for this model.

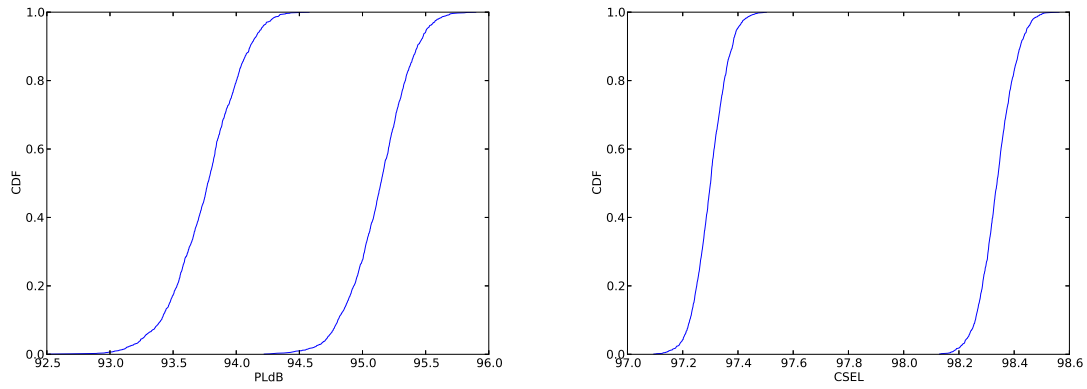

(a) PLdB (b) CSEL

Figure 8.19. 69° Delta Wing Euler PLdB and CSEL Probability Box Boundaries

Table 8.16. 69° Delta Wing 95% Confidence Intervals

Configuration	PLdB	CSEL
Euler	[93.16 , 95.58]	[97.18 , 98.46]
Turbulent	[94.03 , 96.35]	[97.63 , 98.85]

The contribution of the top uncertain parameters to both PLdB and CSEL are given in Tables 8.17 and 8.18, respectively. The results of this sensitivity analysis are similar to those observed for the SEEB-ALR. The reflection factor contributes even more to the total output uncertainty for both loudness metrics, and the contribution of the atmospheric humidity variation contributes significantly to PLdB.

3. LM 1021-01 Low-Boom Configuration

For the LM 1021-01, near-field signatures were taken at 20.7 inches from the body to coincide with experimental data. Comparison with the experiment is shown in Figure 8.20(a) for both inviscid and fully turbulent flow assumptions. A residual scale plot of the signatures is shown in Figure 8.20(b). The fully turbulent solution agrees well with the experimental results, with the exception of the rounding of the

Table 8.17. 69° Delta Wing Top Uncertain Parameter Contribution to PLdB Total Uncertainty

Uncertain Parameter	Euler	Turbulent
Initial Step Size	1.4%	1.0%
Reflection Factor	50.9%	52.0%
Temperature Profile	1.3%	1.8%
Humidity Profile	37.1%	38.0%
Ground Elevation	7.9%	6.3%
All Others	<1%	<1%

Table 8.18. 69° Delta Wing Top Uncertain Parameter Contribution to CSEL Total Uncertainty

Uncertain Parameter	Euler	Turbulent
Reflection Factor	93.1%	94.4%
Temperature Profile	2.1%	2.5%
Humidity Profile	1.1%	1.5%
Ground Elevation	1.9%	1.4%
All Others	<1%	<1%

peaks in the experimental results, similar to the delta wing and SEEB-ALR models. The inviscid solution, however, does not agree as well. Aftosmis et al.[1] identify the source of this discrepancy, which stems from a shock originating at the front of the under wing nacelle. In the viscous case, this shock is smeared by the boundary layer between the wing and nacelle, but propagates in the inviscid simulation. A more complete discussion is included in the reference. An important note should be made regarding the length of the LM 1021-01 signature. The computational domain is slightly truncated as the signature does not fully recover to zero. As stated above, the ends of the signatures are forced to zero to prevent any numerical issues in propagating the signature to the ground level. This artificial forcing of the signature, however, is

not expected to affect the loudness results as this is not in a strong shock or expansion region.

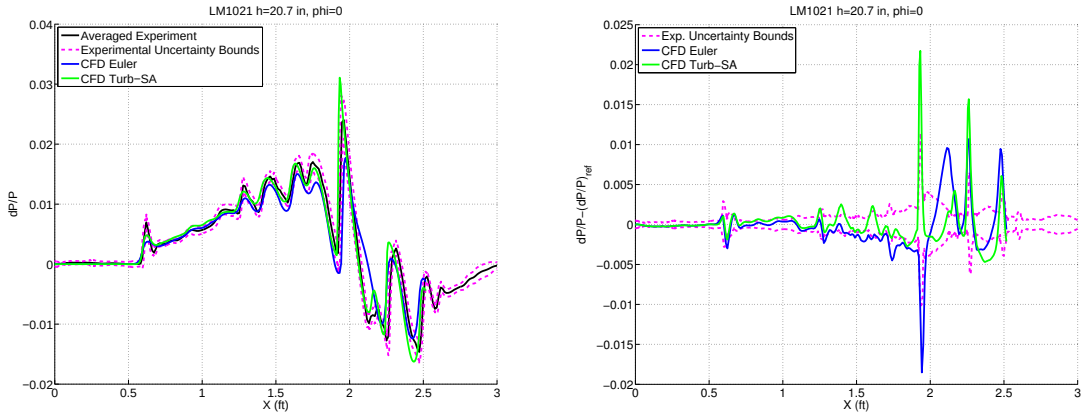

(a) Signatures (b) Residual Scale

Figure 8.20. LM 1021-01 Near-Field CFD Comparison with Experimental Results

The surrogate models for CSEL and PLdB are constructed in the same fashion as for the other cases. The dispersion of the deterministic samples for the Euler case are shown in Figure 8.21(a). Figure 8.21(b) shows the same dispersion of signals, but shifted to reference location for better visualization of changes in signature amplitude. For the Euler case, the resulting ground signature dispersion is shown in Figure 8.22(a) and shifted to a reference location in Figure 8.22(b). The ground signatures were then analyzed to produce the desired loudness quantities of interest.

Similar dispersions of the near-field and ground level signatures can be generated for the fully turbulent case. Because of the effect of different flow physics modeling, the signatures for the turbulent case are slightly different, both in the near-field, as well as at the ground level. The near-field signatures are shown in Figure 8.23(a) and shifted to a reference location in Figure 8.23(b). The ground level signatures are shown in Figure 8.24(a) and shifted to a reference location in Figure 8.24(b).

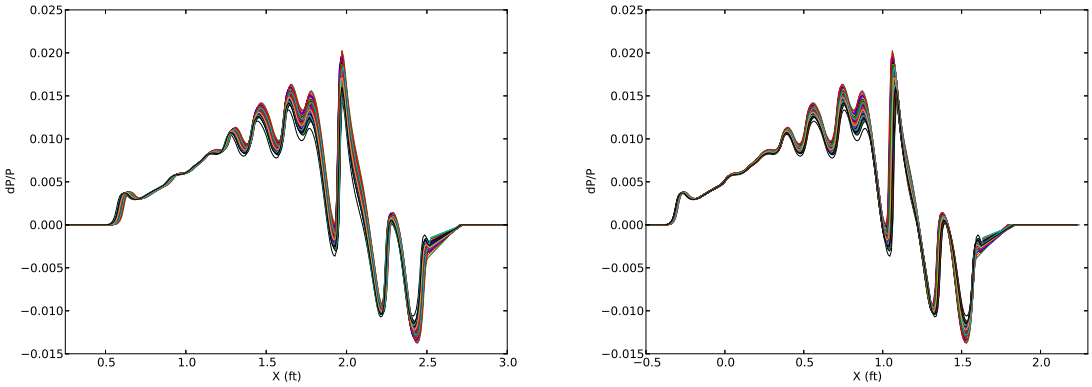

(a) Actual (b) Shifted

Figure 8.21. LM 1021-01 Euler Near-Field Pressure Signature Dispersion

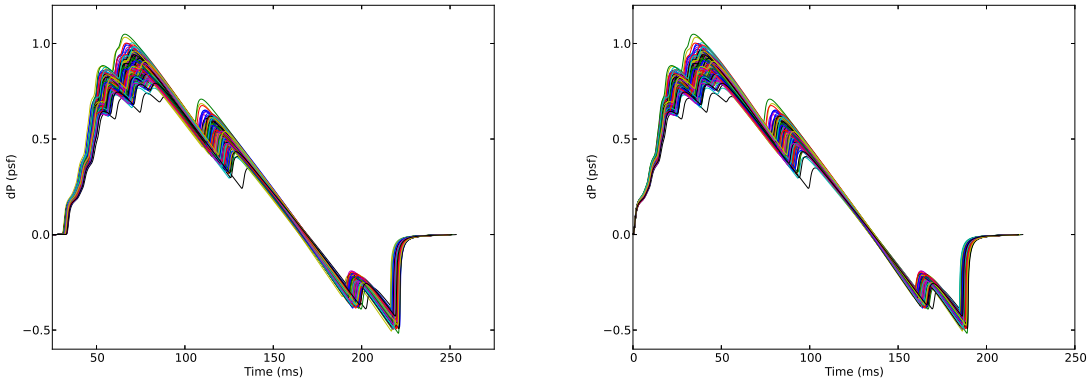

(a) Actual (b) Shifted

Figure 8.22. LM 1021-01 Euler Ground Signature Dispersion

The surrogates are validated using 20 test points distributed throughout the design space, similar to the previous two models. The average error at these 20 test points was less than 0.2% for all of the flow type/loudness quantity combinations indicating the selection of a second-order PCE was sufficient. The uncertainty is propagated through the surrogates and a family of CDFs were produced. For the

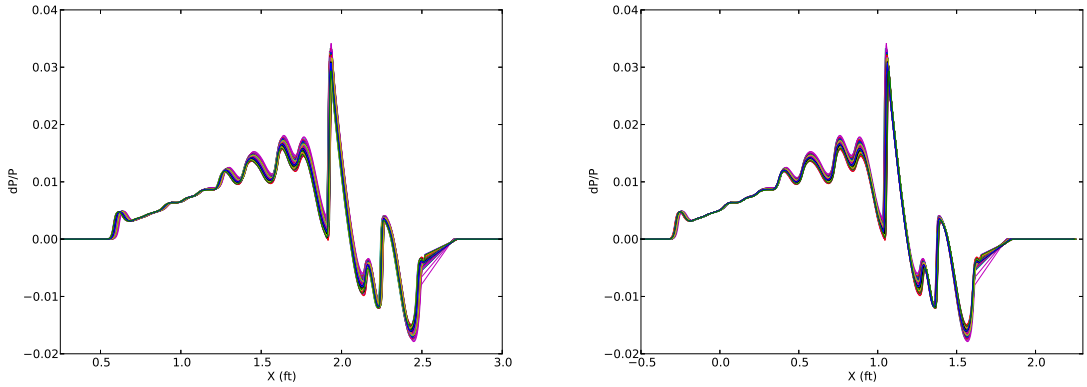

(a) Actual (b) Shifted

Figure 8.23. LM 1021-01 Turbulent Near-Field Pressure Signature Dispersion

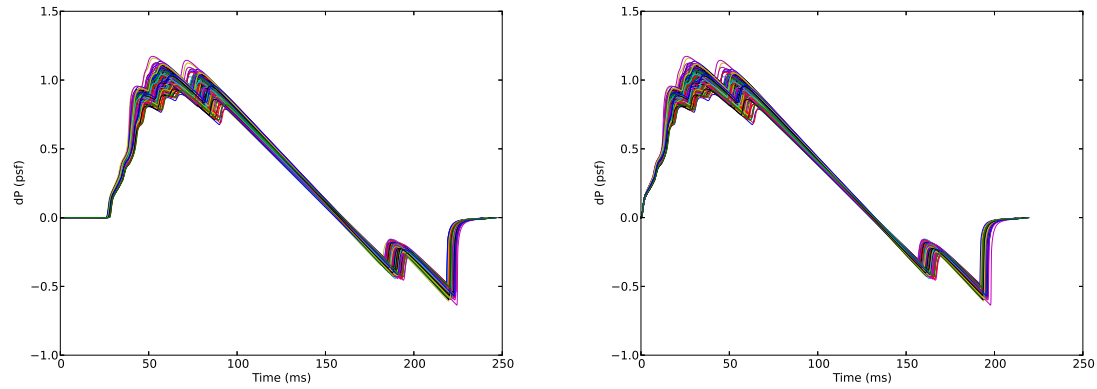

(a) Actual (b) Shifted

Figure 8.24. LM 1021-01 Turbulent Ground Signature Dispersion

Euler case, the boundaries of the probability boxes are shown in Figure 8.25(a) and Figure 8.25(b) for PLdB and CSEL, respectively.

A summary of the 95% confidence intervals for both Euler and Turbulent cases is shown in Table 8.19. From these results, the effect of an inviscid versus the fully turbulent analysis is more significant than for the SEEB-ALR and the Delta wing models for both loudness measures. This is due to the reduced order modeling fidelity

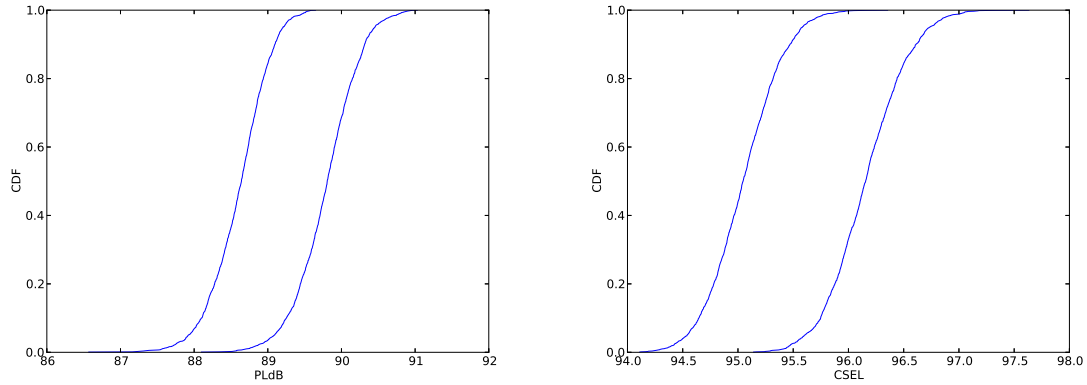

(a) PLdB (b) CSEL

Figure 8.25. LM 1021-01 Euler PLdB Probability Box Boundaries

of the Euler analysis. While the loudness values are lower for the inviscid case, which is desirable, the accuracy of the Euler model has to be in question due to this significant difference. Along with the discrepancy in the near-field signature, this indicates an inviscid assumption is not appropriate for this configuration under the current flow conditions. Aftosmis et al. [1] notes the wind tunnel experiments were conducted at a relatively low Reynolds number (which was matched for the simulations). At a higher Reynolds number, an Euler solution may be sufficient, but this must first be validated for the new freestream conditions.

Table 8.19. LM 1021-01 95% Confidence Intervals

Configuration	**PLdB**	**CSEL**
Euler	[87.76 , 90.60]	[94.43 , 96.85]
Turbulent	[90.17 , 93.79]	[96.06 , 98.76]

The contribution of the top uncertain parameters to both PLdB and CSEL are given in Tables 8.20 and 8.21, respectively. The results of this sensitivity analysis is different than that observed for the SEEB-ALR and Delta Wing models as the reflection factor is no long the top parameter. While the reflection is still significant, angle of attack now dominates the output uncertainty for both loudness metrics. Because of the specific design of the LM 1021-01, changes in angle attack may effect the use of specific design features, especially those related to shock cancellation off the body.

Table 8.20. LM 1021-01 Top Uncertain Parameter Contribution to PLdB Total Uncertainty

Uncertain Parameter	**Euler**	**Turbulent**
Mach Number	1.4%	0.2%
Angle of Attack	39.0%	55.1%
Reflection Factor	33.8%	21.9%
Temperature Profile	1.6%	0.7%
Humidity Profile	22.7%	17.9%
Ground Elevation	1.6%	4.3%
All Others	<1%	<1%

Table 8.21. LM 1021-01 Top Uncertain Parameter Contribution to CSEL Total Uncertainty

Uncertain Parameter	**Euler**	**Turbulent**
Angle of Attack	57.2%	63.9%
Reflection Factor	38.2%	32.0%
Temperature Profile	1.1%	1.3%
Ground Elevation	2.4%	2.9%
All Others	<1%	<1%

9. CONCLUSIONS AND FUTURE WORK

This section gives a brief summary of this work presented. Future work is also discussed to give guidance for possible efforts to build on or improve upon this study.

9.1. CONCLUSIONS

The objective of this work was to introduce new advancements for uncertainty quantification (UQ) with stochastic expansions and apply these methods to stochastic models of supersonic and hypersonic flows. First, a multi-step UQ approach was introduced and serves as an efficient means of dimension reduction for problems with a large number of uncertain variables. The multi-step UQ approach included several key components including a sensitivity-based dimension reduction process that used a local analysis at selected sample locations to approximate global sensitivities. Other components included a modification scheme to update existing deterministic samples after dimension reduction and a modified point-collocation non-intrusive polynomial chaos method that incorporates the local sensitivity information as part of the point-collocation solution process.

A second approach was introduced that is based on a sparse approximation of the polynomial chaos expansion. The fundamental idea was to use Basis Pursuit Denoising to recover the polynomial chaos expansion coefficients from an underdetermined system of linear equations. Solutions were obtained iteratively with increasing sample size, while tracking the convergence of the polynomial chaos expansion coefficients. This study also introduced two methods of measuring the accuracy of the expansion coefficients and their convergence when the sample size used to obtain the polynomial chaos expansion coefficients was iteratively increased. These two methods included using both the sensitivities of each uncertain parameter

via the calculation of Sobol indices and a comparison to the actual response at selected test points in the design space. This procedure allowed for a computationally efficient approach to measuring the convergence of the polynomial chaos expansion coefficients, while reducing the number of samples needed to obtain an accurate solution.

The multi-step and sparse approximation approaches were applied to stochastic models of hypersonic flows. The uncertainty in a model based on the Fay and Riddell correlation for the prediction of convective heating at the stagnation-point of a blunt-body was investigated. Additionally, high-fidelity computational fluid dynamics models of radiative heating on the surface of hypersonic inflatable aerodynamic decelerators during entry into Mars and Titan were also explored. These models possess a significant amount of uncertainty and pose challenges for efficient UQ. The methodologies developed in this work have shown that construction of an accurate surrogate model could be achieved at about 10% of the computational cost needed to construct a full dimension, total order expansion.

Another objective of this work was to introduce methodologies used for further advancement of the quantification of margins and uncertainties (QMU) methodologies implemented for aerospace system models. First, the use of stochastic expansions was introduced to efficiently quantify the uncertainty in system design performance metrics, as well as performance boundaries. Then, procedures were defined to measure margin and uncertainty metrics for QMU analysis of systems containing multiple types of uncertainty representation. To demonstrate the QMU methodologies developed in this work, two model problems were selected. The first is a model of a spacecraft reentry trajectory coupled with models for heat flux prediction and bank angle modulation. The second problem is a multi-system model used for certification prediction of sonic-boom loudness from low-boom, supersonic vehicle configurations.

Overall the methods and results of this work have outlined many effective approaches for UQ of large-scale, high-dimension supersonic and hypersonic problems

containing both epistemic and aleatory uncertainty. The methods presented showed significant reduction in the number of required evaluations of the deterministic model needed to achieve an accurate surrogate model with polynomial chaos expansions for UQ.

9.2. FUTURE WORK

While significant advancements have been made in this study, there are still several areas that warrant further work. With regards to the UQ methodologies, the multi-step approach should be coupled to a higher order sensitivity analysis approach. In this study, first-order finite differencing was used due to the lack of capability of the computational fluid dynamics models. Improved efficiency and accuracy gained using methods such as adjoint-based sensitivities would be of great interest and should be investigated in the future.

The sparse approximation approach would also stand to be improved upon. First and for most, adaptive sampling techniques should be investigated to improve the efficiency when iteratively growing the sample size. The approach used in this study is simple and easy to implement, but may not be very efficient as samples are randomly pulled from a larger sample set. Another area of improvement for this approach could to be determine a more accurate estimate of the truncation error used in the L_1 minimization approach. In this study, this value was set to zero as the solution is unique in this case. However, forcing this constraint could lead to over fitting. Obtaining an estimate of this error based on the solution of the L_1 minimization problem may yield a more accurate surrogate model.

With regards to the model problems, there is much more uncertainty that could be considered. This is particularly the case for the radiation model problems. These high-fidelity models are extremely complex both numerically and in the physics they represent. While significant effort was put in to assessing the uncertainty in these

models, there are still sources of uncertainty that may impact radiative heating predictions. Uncertainty sources not considered in the radiation problems may include vibrational relaxation times, uncertainty in the two-temperature energy equation, and model-form uncertainty due to numerical schemes used by the flow field solver and radiation model. Cross validation with other models would offer some assessment of any model-form uncertainty. Also, there is so little experimental data available simply due to the fact that replicating these environments and performing accurate measurements possess a significant engineering challenge. With advancements in modeling approaches and with additional/new experimental data, these models may be reevaluated for better estimates of the radiative heating uncertainty.

APPENDIX A

Radiation Uncertainty Sources for Mars Entry

The following appendix gives tables of the four groups of uncertain parameters for the radiative heat transfer model for Mars entry. Note that the parameters of Tables A1, A3, and A4 are those of an Arrhenius form. The equations for each of these three tables are given (Eq. (A.1), (A.2), and (A.3).) For further description of the uncertain parameters, the justification of their uncertainty ranges, and detailed discussion of the radiation modeling approach, see Johnston et al. [39]

Table A1. Uncertain Flow field Chemical Kinetics

#	Reaction	$A_{f,i}$	$n_{f,i}$	$D_{f,i}$	$T_{f,i}$	Ref.	Uncertainty
1	$CO_2 + M \leftrightarrow CO + O + M$	2.8e+22	-1.50	6.328e+4	T_a	N, C, O	-1, +0 om
		1.4e+22	-1.50	6.328e+4	T_a	others	-1, +0 om
2	$CO + M \leftrightarrow C + O + M$	3.0e+21	-1.00	1.29e+5	T_a	All	-75%, +50%
3	$C_2 + M \leftrightarrow 2C + M$	4.5e+18	-1.00	7.15e+4	T_a	All	-1, +1 om
4	$CN + M \leftrightarrow C + N + M$	6.0e+15	-0.4	7.10e+4	T_a	All	-1, +1 om
5	$N_2 + M \leftrightarrow 2N + M$	3.0e+22	-1.60	1.132e+5	T_a	N, C, O	-1, +1 om
		6.0e+3	2.6	1.132e+5	T_{ve}	e^-	-1, +1 om
		7.0e+21	-1.60	1.132e+5	T_a	others	-1, +1 om
6	$NO + M \leftrightarrow N + O + M$	1.1e+17	0.00	7.55e+4	T_a	N, C, O, NO, CO_2	-1, +1 om
		5.0e+15	0.00	7.55e+4	T_a	others	-1, +1 om
7	$O2 + M \leftrightarrow 2O + M$	1.0e+22	-1.50	5.936e+04	T_a	N, C, O	-50%, +50%
		2.0e+21	-1.50	5.936e+04	T_a	others	-50%, +50%
8	$CO_2 + O \leftrightarrow O_2 + CO$	2.71e+14	0.0	3.38e+4	T_{tr}		-1, +1 om
9	$CO + C \leftrightarrow C_2 + O$	2.4e+17	-1.00	5.80e+4	T_{tr}		-1, +1 om
10	$CO + N \leftrightarrow CN + O$	1.0e+14	0.00	3.86e+4	T_{tr}		-1, +1 om
11	$CO + NO \leftrightarrow CO_2 + N$	3.0e+6	0.88	1.33e+4	T_{tr}		-1, +1 om
12	$CO + O \leftrightarrow O_2 + C$	3.9e+13	-0.18	6.92e+4	T_{tr}		-0, +1 om
13	$C_2 + N_2 \leftrightarrow CN + CN$	1.5e+13	0.0	2.1e+4	T_{tr}		-1, +1 om
14	$CN + C \leftrightarrow C_2 + N$	3.0e+14	0.00	1.81e+4	T_{tr}		-1, +1 om
15	$CN + O \leftrightarrow NO + C$	1.6e+12	0.10	1.46e+4	T_{tr}		-1, +1 om
16	$N + CO \leftrightarrow NO + C$	1.1e+14	0.07	5.35e+4	T_{tr}		-1, +1 om
17	$N_2 + C \leftrightarrow CN + N$	1.1e+14	-0.11	2.32e+4	T_{tr}		-50%, +50%
18	$N_2 + CO \leftrightarrow CN + NO$	1.2e+16	-1.23	7.70e+4	T_{tr}		-1, +1 om
19	$N_2 + O \leftrightarrow NO + N$	6.0e+13	0.1	3.80e+4	T_{tr}		-50%, +50%
20	$O_2 + N \leftrightarrow NO + O$	2.49e+9	1.18	4.01e+3	T_{tr}		-1, +1 om

$$k_{f,i} = A_{f,i} T_{f,i}^{n_{f,i}} exp(-D_{f,i}/T_{f,i}) \tag{A.1}$$

$$K_{f,ij}^{hp} = A_{hp} \left(\frac{T_a}{6000} \right)^{n_{hp}} exp(-E_{hp}/T_a) \tag{A.2}$$

$$K_{f,ij}^{el} = A_{el} {T_{ve}}^{n_{el}} exp(-E_{el}/T_{ve}) \tag{A.3}$$

Table A2. Uncertain Molecular Band Processes

Molecule	Upper State – Lower State	Band Name	λ Range (nm)	Uncertainty
CO	$A^1\Pi - X^1\Sigma^+$	4th Positive	120 – 280	+/- 40%
CO	$b^3\Sigma^+ - a^3\Pi_r$	3rd Positive	250 – 450	+/- 50%
CO	$d^3\Delta_i - a^3\Pi_r$	Triplet	320 – 2500	+/- 50%
CO	$a'^3\Sigma^+ - a^3\Pi_r$	Asundi	370 – 2500	+/- 50%
CO	$B^1\Sigma^+ - A^1\Pi$	Angstrom	400 – 700	+/- 50%
CO	$X^1\Sigma^+ - X^1\Sigma^+$	Infrared	1200 – 7000	+/- 50%
CN	$A^2\Pi_i - X^2\Sigma^+$	Red	400 – 2800	+/- 30%
CN	$B^2\Sigma^+ - X^2\Sigma^+$	Violet	300 – 550	+/- 15%
C_2	$d^3\Pi_g - a^3\Pi_u$	Swan	390 – 1000	+/- 50%
C_2	$b^3\Sigma_g^- - a^3\Pi_u$	Ballik-Ramsay	500 – 3000	+/- 50%
C_2	$A^1\Pi_u - X^1\Sigma_g^+$	Phillips	350 – 1200	+/- 50%
C_2	$D^1\Sigma_u^+ - X^1\Sigma_g^+$	Mulliken	200 – 250	+/- 50%
C_2	$C^1\Pi_g - A^1\Pi_u$	Des.-D'Azam.	280 – 700	+/- 50%
C_2	$e^3\Pi_g - a^3\Pi_u$	Fox-Herzberg	200 – 500	+/- 50%
CO_2	$X^1\Sigma_g^+ - X^1\Sigma_g^+$	Infrared	1700 – 25000	+/- 50%
CO_2	$A^1B_2 - X^1\Sigma_g^+$	UV	190 – 320	+/- 100%

Table A3. Uncertain Heavy-Particle Impact Excitation Rates (cm^3/s) for non-Boltzmann Modeling

#	Reaction	A_{hp}	n_{hp}	E_{hp}	Uncertainty
1	$CN(X^2\Sigma^+) + M \leftrightarrow CN(A^2\Pi) + M$	M dependent			+/- 1 om
2	$CN(A^2\Pi) + M \leftrightarrow CN(B^2\Sigma^+) + M$	M dependent			+/- 1 om
3	$CN(B^2\Sigma^+) + M \leftrightarrow CN(a^4\Sigma^+) + M$	M dependent			+/- 2 om
4	$CN(a^4\Sigma^+) + M \leftrightarrow CN(D^2\Pi^+) + M$	M dependent			+/- 2 om
5	$CO(X^1\Sigma^+) + M \leftrightarrow CO(a^3\Pi) + M$	M dependent			+/- 1 om
6	$CO(X^1\Sigma^+) + M \leftrightarrow CO(a'^3\Sigma^+) + M$	5.20E-10	0.500	80370	+/- 1 om
7	$CO(X^1\Sigma^+) + M \leftrightarrow CO(d^3\Delta) + M$	2.61E-11	0.500	87975	+/- 1 om
8	$CO(X^1\Sigma^+) + M \leftrightarrow CO(A^1\Pi) + M$	2.52E-09	0.344	93669	+/- 1 om
9	$CO(a^3\Pi) + M \leftrightarrow CO(a'^3\Sigma^+) + M$	M dependent			+/- 2 om
10	$CO(a'^3\Sigma^+) + M \leftrightarrow CO(d^3\Delta) + M$	M dependent			+/- 2 om
11	$CO(d^3\Delta) + M \leftrightarrow CO(e^3\Sigma^-) + M$	M dependent			+/- 2 om
12	$CO(e^3\Sigma^-) + M \leftrightarrow CO(A^1\Pi) + M$	8.78e-11	0.498	971	+/- 2 om
13	$C_2(X^1\Sigma^+) + M \leftrightarrow C_2(b^3\Sigma^-) + M$	7.23e-10	0.773	9504.7	+/- 2 om
14	$C_2(X^1\Sigma^+) + M \leftrightarrow C_2(c^3\Sigma^+) + M$	8.67e-10	0.773	15176.6	+/- 2 om
15	$C_2(X^1\Sigma^+) + M \leftrightarrow C_2(d^3\Pi) + M$	7.49e-10	1.06	27927.7	+/- 1 om
16	$C_2(X^1\Sigma^+) + M \leftrightarrow C_2(C^1\Pi) + M$	3.76e-09	0.773	44096.6	+/- 2 om
17	$C_2(b^3\Sigma^-) + M \leftrightarrow C_2(c^3\Sigma^+) + M$	1.21e-09	0.773	5671.9	+/- 2 om
18	$C_2(b^3\Sigma^-) + M \leftrightarrow C_2(d^3\Pi) + M$	1.21e-9	0.773	18423.0	+/- 2 om
19	$C_2(b^3\Sigma^-) + M \leftrightarrow C_2(C^1\Pi) + M$	5.26e-09	0.773	34591.9	+/- 2 om
20	$C_2(c^3\Sigma^+) + M \leftrightarrow C_2(d^3\Pi) + M$	1.01e-09	0.773	12751.1	+/- 2 om
21	$C_2(c^3\Sigma^+) + M \leftrightarrow C_2(C^1\Pi) + M$	4.38e-09	0.773	28920.0	+/- 2 om
22	$C_2(d^3\Pi) + M \leftrightarrow C_2(C^1\Pi) + M$	4.38e-09	0.773	16168.9	+/- 2 om

Table A4. Uncertain Electron-Impact Excitation Rates (cm^3/s) for non-Boltzmann Modeling

#	Reaction	A_{el}	n_{el}	E_{el}	Uncertainty
1	$CN(X^2\Sigma^+) + e^- \leftrightarrow CN(A^2\Pi) + e^-$	6.41e-09	0.20	18303	+/- 1 om
2	$CN(X^2\Sigma^+) + e^- \leftrightarrow CN(B^2\Sigma^+) + e^-$	6.83e-10	0.39	40428	+/- 1 om
3	$CN(X^2\Sigma^+) + e^- \leftrightarrow CN(a^4\Sigma^+) + e^-$	5.13e-11	0.35	47323	+/- 2 om
4	$CN(X^2\Sigma^+) + e^- \leftrightarrow CN(D^2\Pi^+) + e^-$	4.07e-10	0.25	79368	+/- 2 om
5	$CN(A^2\Pi) + e^- \leftrightarrow CN(B^2\Sigma^+) + e^-$	1.36e-04	-0.74	28030	+/- 2 om
6	$CN(A^2\Pi) + e^- \leftrightarrow CN(a^4\Sigma^+) + e^-$	4.55e-04	-0.77	37548	+/- 2 om
7	$CN(A^2\Pi) + e^- \leftrightarrow CN(D^2\Pi^+) + e^-$	1.22e-03	-0.82	69300	+/- 2 om
8	$CN(B^2\Sigma^+) + e^- \leftrightarrow CN(a^4\Sigma^+) + e^-$	7.85e-05	-0.66	14148	+/- 2 om
9	$CN(B^2\Sigma^+) + e^- \leftrightarrow CN(D^2\Pi^+) + e^-$	6.29e-04	-0.79	45559	+/- 2 om
10	$CN(a^4\Sigma^+) + e^- \leftrightarrow CN(D^2\Pi^+) + e^-$	4.23e-04	-0.77	36015	+/- 2 om
11	$CO(X^1\Sigma^+) + e^- \leftrightarrow CO(a^3\Pi) + e^-$	8.42e-11	0.28	80530	+/- 1 om
12	$CO(X^1\Sigma^+) + e^- \leftrightarrow CO(a'^3\Sigma^+) + e^-$	1.82e-14	1.17	102434	+/- 1 om
13	$CO(X^1\Sigma^+) + e^- \leftrightarrow CO(d^3\Delta) + e^-$	3.16e-12	0.66	114626	+/- 1 om
14	$CO(X^1\Sigma^+) + e^- \leftrightarrow CO(e^3\Sigma^-) + e^-$	2.10e-14	1.17	113995	+/- 1 om
15	$CO(X^1\Sigma^+) + e^- \leftrightarrow CO(A^1\Pi) + e^-$	3.82e-09	0.12	95850	+/- 1 om
16	$CO(a^3\Pi) + e^- \leftrightarrow CO(a'^3\Sigma^+) + e^-$	4.43e-8	-0.73	23456	+/- 1 om
17	$CO(a^3\Pi) + e^- \leftrightarrow CO(d^3\Delta) + e^-$	7.74e-15	1.17	44552	+/- 1 om
18	$CO(a^3\Pi) + e^- \leftrightarrow CO(e^3\Sigma^-) + e^-$	3.21e-15	1.27	44896	+/- 1 om
19	$CO(a^3\Pi) + e^- \leftrightarrow CO(A^1\Pi) + e^-$	1.49e-05	-0.74	27860	+/- 2 om
20	$CO(a'^3\Sigma^+) + e^- \leftrightarrow CO(d^3\Delta) + e^-$	2.53e-11	0.16	10611	+/- 1 om
21	$CO(a'^3\Sigma^+) + e^- \leftrightarrow CO(e^3\Sigma^-) + e^-$	6.04e-13	0.61	11041	+/- 1 om
22	$CO(a'^3\Sigma^+) + e^- \leftrightarrow CO(A^1\Pi) + e^-$	6.56e-06	-0.69	17750	+/- 2 om
23	$CO(d^3\Delta) + e^- \leftrightarrow CO(e^3\Sigma^-) + e^-$	1.09e-10	1.66	10686	+/- 1 om
24	$CO(d^3\Delta) + e^- \leftrightarrow CO(A^1\Pi) + e^-$	2.62e-06	-0.63	10570	+/- 2 om
25	$CO(e^3\Sigma^-) + e^- \leftrightarrow CO(A^1\Pi) + e^-$	1.41e-06	-0.58	6971	+/- 2 om
26	$C_2(X^1\Sigma^+) + e^- \leftrightarrow C_2(b^3\Sigma^-) + e^-$	5.25e-04	-0.876	12822.89	+/- 2 om
27	$C_2(X^1\Sigma^+) + e^- \leftrightarrow C_2(c^3\Sigma^+) + e^-$	3.37e-05	-0.530	16676.24	+/- 2 om
28	$C_2(X^1\Sigma^+) + e^- \leftrightarrow C_2(d^3\Pi) + e^-$	6.45e-08	-0.179	29932.77	+/- 1 om
29	$C_2(X^1\Sigma^+) + e^- \leftrightarrow C_2(C^1\Pi) + e^-$	1.00e-04	-0.396	45526.85	+/- 2 om
30	$C_2(b^3\Sigma^-) + e^- \leftrightarrow C_2(c^3\Sigma^+) + e^-$	8.57e-03	-1.215	9893.11	+/- 2 om
31	$C_2(b^3\Sigma^-) + e^- \leftrightarrow C_2(d^3\Pi) + e^-$	1.59e-05	-0.436	19375.79	+/- 2 om
32	$C_2(b^3\Sigma^-) + e^- \leftrightarrow C_2(C^1\Pi) + e^-$	6.89e-05	-0.381	35594.37	+/- 2 om
33	$C_2(c^3\Sigma^+) + e^- \leftrightarrow C_2(d^3\Pi) + e^-$	9.03e-05	-0.647	14918.32	+/- 2 om
34	$C_2(c^3\Sigma^+) + e^- \leftrightarrow C_2(C^1\Pi) + e^-$	5.428e-05	-0.372	29691.92	+/- 2 om
35	$C_2(d^3\Pi) + e^- \leftrightarrow C_2(C^1\Pi) + e^-$	1.09e-04	-0.495	17461.08	+/- 2 om

APPENDIX B

Radiation Uncertainty Sources for Titan Entry

The following appendix gives tables of the four groups of uncertain parameters for Titan entry. Note that the parameters of Tables B1, B3, and B4 are those of an Arrhenius form. The equations for each of these three tables are given in Eq. (B.1), (B.2), and (B.3).

Table B1. Titan Entry Flow Field Chemical Kinetics

#	Reaction	$A_{f,i}$	$n_{f,i}$	$D_{f,i}$	$T_{f,i}$	Ref.	F_i
	Dissociation Reactions						
1	$N_2 + M \leftrightarrow 2N + M$	3.00e+22	-1.60	1.132e+5	T_a	N, C, H	3.0
		3.00e+24	-1.60	1.132e+5	T_a	e^-	5.0
		7.00e+21	-1.60	1.132e+5	T_a	others	5.0
2	$CH_4 + M \leftrightarrow CH_3 + H + M$	4.70e+47	-8.20	5.92e+4	T_a	All	2.0
3	$CH_3 + M \leftrightarrow CH_2 + H + M$	1.02e+16	0.00	4.56e+4	T_a	All	3.2
4	$CH_3 + M \leftrightarrow CH + H_2 + M$	5.00e+15	0.00	4.28e+4	T_a	All	2.0
5	$CH_2 + M \leftrightarrow CH + H + M$	4.00e+15	0.00	4.18e+4	T_a	All	2.0
6	$CH_2 + M \leftrightarrow C + H_2 + M$	1.30e+14	0.00	2.97e+4	T_a	All	2.0
7	$H2 + M \leftrightarrow 2O + M$	1.90e+14	0.00	3.37e+4	T_a	All	2.0
8	$CH + M \leftrightarrow C + H + M$	1.50e+16	0.00	7.16e+4	T_a	All	2.0
9	$H_2 + M \leftrightarrow 2H + M$	2.23e+14	0.00	4.835e+4	T_a	All	2.0
10	$CN + M \leftrightarrow C + N + M$	2.53e+14	0.00	7.1e+4	T_a	All	2.0
11	$NH + M \leftrightarrow N + H + M$	1.80e+14	0.00	3.76e+4	T_a	All	2.0
12	$HCN + M \leftrightarrow CN + H + N$	3.57e+26	-2.60	6.2845e+4	T_a	All	2.0
	Exchange Reactions						
13	$CH_3 + N \leftrightarrow HCN + H + H$	7.00e+13	0.00	0	T_a		10.0
14	$CH_3 + H \leftrightarrow CH_2 + H_2$	6.03e+13	0.00	7.6e+3	T_a		10.0
15	$CH_2 + N_2 \leftrightarrow HCN + NH$	4.82e+12	0.00	1.8e+4	T_a		10.0
16	$CH_2 + N \leftrightarrow HCN + H$	5.00e+13	0.00	0	T_a		10.0
17	$CH_2 + H \leftrightarrow CH + H_2$	6.03e+12	0.00	-9.0e+2	T_a		10.0
18	$CH + N_2 \leftrightarrow HCN + N$	4.40e+12	0.00	1.106e4	T_a		3.2
19	$CH + C \leftrightarrow C_2 + H$	2.00e+14	0.00	0	T_a		10.0
20	$C_2 + N_2 \leftrightarrow CN + CN$	1.50e+13	0.00	2.1e+4	T_a		2.0
21	$CN + H_2 \leftrightarrow HCN + H$	2.95e+5	0.00	1.13e+3	T_a		5.0
22	$CN + C \leftrightarrow C_2 + N$	5.00e+13	0.00	1.3e+4	T_a		5.0
23	$N + H_2 \leftrightarrow NH + H$	1.60e+14	0.00	1.265e+4	T_a		2.0
24	$C + N_2 \leftrightarrow CN + N$	5.24e+13	0.00	2.265e+4	T_a		2.0
25	$C + H_2 \leftrightarrow CH + H$	4.00e+14	0.00	1.17e+4	T_a		2.0
26	$H + N_2 \leftrightarrow NH + N$	3.00e+12	0.50	7.14e+4	T_a		3.2
27	$H + CH_4 \leftrightarrow CH_3 + H_2$	1.32e+4	3.00	4.045e+3	T_a		2.0
	Ionization Reactions						
28	$N + N \leftrightarrow N_2^+ + e^-$	4.40e+7	1.50	6.75e+4	T_a		10.0
29	$C + N \leftrightarrow CN^+ + e^-$	1.00e+15	1.50	1.644e+5	T_a		10.0
30	$N + e^- \leftrightarrow N^+ + e^- + e^-$	2.50e+34	-3.82	1.686e+5	T_a		10.0
31	$C + e^- \leftrightarrow C^+ + e^- + e^-$	3.70e+31	-3.00	1.3072e+5	T_a		10.0
32	$H + e^- \leftrightarrow H^+ + e^- + e^-$	2.20e+30	-2.80	1.578e+5	T_a		10.0
33	$Ar + e^- \leftrightarrow Ar^+ + e^- + e^-$	2.50e+34	-3.82	1.817e+5	T_a		10.0
34	$CN^+ + M \leftrightarrow CN + N^+$	2.23e+14	0.00	4.07e+4	T_a		10.0
35	$C^+ + N_2 \leftrightarrow N_2^+ + C$	2.53e+14	-0.11	5.0e+4	T_a		10.0

$$k_{f,i} = A_{f,i} T_{f,i}^{n_{f,i}} exp(-D_{f,i}/T_{f,i}) \tag{B.1}$$

$$K_{f,ij}^{hp} = A_{hp} \left(\frac{T_a}{6000} \right)^{n_{hp}} exp(-E_{hp}/T_a) \tag{B.2}$$

Table B2. Molecular Band Processes

Molecule	Upper State – Lower State	Band Name	λ Range (nm)	Uncertainty
CN	$A^2\Pi_i$ – $X^2\Sigma^+$	Red	400 – 2800	+/- 30%
CN	$B^2\Sigma^+$ – $X^2\Sigma^+$	Violet	300 – 550	+/- 15%
C_2	$d^3\Pi_g$ – $a^3\Pi_u$	Swan	390 – 1000	+/- 50%
C_2	$b^3\Sigma_g^-$ – $a^3\Pi_u$	Ballik-Ramsay	500 – 3000	+/- 50%
C_2	$A^1\Pi_u$ – $X^1\Sigma_g^+$	Phillips	350 – 1200	+/- 50%
C_2	$D^1\Sigma_u^+$ – $X^1\Sigma_g^+$	Mulliken	200 – 250	+/- 50%
C_2	$C^1\Pi_g$ – $A^1\Pi_u$	Des.-D'Azam.	280 – 700	+/- 50%
C_2	$e^3\Pi_g$ – $a^3\Pi_u$	Fox-Herzberg	200 – 500	+/- 50%

Table B3. Heavy-Particle Impact Excitation Rates (cm^3/s) for non-Boltzmann Modeling

#	Reaction	A_{hp}	n_{hp}	E_{hp}	Uncertainty
1	$CN(X^2\Sigma^+) + M \leftrightarrow CN(A^2\Pi) + M$	M dependent			+/- 1 om
2	$CN(A^2\Pi) + M \leftrightarrow CN(B^2\Sigma^+) + M$	M dependent			+/- 1 om
3	$CN(B^2\Sigma^+) + M \leftrightarrow CN(a^4\Sigma^+) + M$	M dependent			+/- 2 om
4	$CN(a^4\Sigma^+) + M \leftrightarrow CN(D^2\Pi^+) + M$	M dependent			+/- 2 om
5	$C_2(X^1\Sigma^+) + M \leftrightarrow C_2(b^3\Sigma^-) + M$	7.23e-10	0.773	9504.7	+/- 2 om
6	$C_2(X^1\Sigma^+) + M \leftrightarrow C_2(c^3\Sigma^+) + M$	8.67e-10	0.773	15176.6	+/- 2 om
7	$C_2(X^1\Sigma^+) + M \leftrightarrow C_2(d^3\Pi) + M$	7.49e-10	1.06	27927.7	+/- 1 om
8	$C_2(X^1\Sigma^+) + M \leftrightarrow C_2(C^1\Pi) + M$	3.76e-09	0.773	44096.6	+/- 2 om
9	$C_2(b^3\Sigma^-) + M \leftrightarrow C_2(c^3\Sigma^+) + M$	1.21e-09	0.773	5671.9	+/- 2 om
10	$C_2(b^3\Sigma^-) + M \leftrightarrow C_2(d^3\Pi) + M$	1.21e-9	0.773	18423.0	+/- 2 om
11	$C_2(b^3\Sigma^-) + M \leftrightarrow C_2(C^1\Pi) + M$	5.26e-09	0.773	34591.9	+/- 2 om
12	$C_2(c^3\Sigma^+) + M \leftrightarrow C_2(d^3\Pi) + M$	1.01e-09	0.773	12751.1	+/- 2 om
13	$C_2(c^3\Sigma^+) + M \leftrightarrow C_2(C^1\Pi) + M$	4.38e-09	0.773	28920.0	+/- 2 om
14	$C_2(d^3\Pi) + M \leftrightarrow C_2(C^1\Pi) + M$	4.38e-09	0.773	16168.9	+/- 2 om

$$K_{f,ij}^{el} = A_{el} {T_{ve}}^{n_{el}} exp(-E_{el}/T_{ve}) \tag{B.3}$$

Table B4. Electron-Impact Excitation Rates (cm^3/s) for non-Boltzmann Modeling

#	Reaction	A_{el}	n_{el}	E_{el}	Uncertainty
1	$CN(X^2\Sigma^+) + e^- \leftrightarrow CN(A^2\Pi) + e^-$	6.41e-09	0.20	18303	+/- 1 om
2	$CN(X^2\Sigma^+) + e^- \leftrightarrow CN(B^2\Sigma^+) + e^-$	6.83e-10	0.39	40428	+/- 1 om
3	$CN(X^2\Sigma^+) + e^- \leftrightarrow CN(a^4\Sigma^+) + e^-$	5.13e-11	0.35	47323	+/- 2 om
4	$CN(X^2\Sigma^+) + e^- \leftrightarrow CN(D^2\Pi^+) + e^-$	4.07e-10	0.25	79368	+/- 2 om
5	$CN(A^2\Pi) + e^- \leftrightarrow CN(B^2\Sigma^+) + e^-$	1.36e-04	-0.74	28030	+/- 2 om
6	$CN(A^2\Pi) + e^- \leftrightarrow CN(a^4\Sigma^+) + e^-$	4.55e-04	-0.77	37548	+/- 2 om
7	$CN(A^2\Pi) + e^- \leftrightarrow CN(D^2\Pi^+) + e^-$	1.22e-03	-0.82	69300	+/- 2 om
8	$CN(B^2\Sigma^+) + e^- \leftrightarrow CN(a^4\Sigma^+) + e^-$	7.85e-05	-0.66	14148	+/- 2 om
9	$CN(B^2\Sigma^+) + e^- \leftrightarrow CN(D^2\Pi^+) + e^-$	6.29e-04	-0.79	45559	+/- 2 om
10	$CN(a^4\Sigma^+) + e^- \leftrightarrow CN(D^2\Pi^+) + e^-$	4.23e-04	-0.77	36015	+/- 2 om
11	$C_2(X^1\Sigma^+) + e^- \leftrightarrow C_2(b^3\Sigma^-) + e^-$	5.25e-04	-0.876	12822.89	+/- 2 om
12	$C_2(X^1\Sigma^+) + e^- \leftrightarrow C_2(c^3\Sigma^+) + e^-$	3.37e-05	-0.530	16676.24	+/- 2 om
13	$C_2(X^1\Sigma^+) + e^- \leftrightarrow C_2(d^3\Pi) + e^-$	6.45e-08	-0.179	29932.77	+/- 1 om
14	$C_2(X^1\Sigma^+) + e^- \leftrightarrow C_2(C^1\Pi) + e^-$	1.00e-04	-0.396	45526.85	+/- 2 om
15	$C_2(b^3\Sigma^-) + e^- \leftrightarrow C_2(c^3\Sigma^+) + e^-$	8.57e-03	-1.215	9893.11	+/- 2 om
16	$C_2(b^3\Sigma^-) + e^- \leftrightarrow C_2(d^3\Pi) + e^-$	1.59e-05	-0.436	19375.79	+/- 2 om
17	$C_2(b^3\Sigma^-) + e^- \leftrightarrow C_2(C^1\Pi) + e^-$	6.89e-05	-0.381	35594.37	+/- 2 om
18	$C_2(c^3\Sigma^+) + e^- \leftrightarrow C_2(d^3\Pi) + e^-$	9.03e-05	-0.647	14918.32	+/- 2 om
19	$C_2(c^3\Sigma^+) + e^- \leftrightarrow C_2(C^1\Pi) + e^-$	5.428e-05	-0.372	29691.92	+/- 2 om
20	$C_2(d^3\Pi) + e^- \leftrightarrow C_2(C^1\Pi) + e^-$	1.09e-04	-0.495	17461.08	+/- 2 om

BIBLIOGRAPHY

[1] Aftosmis, M. J. and Nemec, M., "Cart3D Simulations for the First AIAA Sonic Boom Prediction Workshop," AIAA Paper 2014-0558, Jan. 2014.

[2] Wiener, N., "The Homogenous Chaos," *American Journal of Mathematics*, Vol. 60, No. 4, 1938, pp. 897–936.

[3] Ghanem, R. G. and Spanos, P. D., *Stochastic Finite Elements: A Spectral Approach*, Springer-Verlag, New York, 1991.

[4] Xiu, D. and Karniadakis, G. E., "The Wiener–Askey Polynomial Chaos for Stochastic Differential Equations," *SIAM Journal on Scientific Computing*, Vol. 24, No. 2, 2002, pp. 619–644.

[5] Walters, R. W. and Huyse, L., "Uncertainty Analysis for Fluid Mechanics with Applications," Tech. rep., ICASE 2002-1, NASA/CR-2002-211449, NASA Langley Research Center, Hampton, VA, 2002.

[6] Najm, H. N., "Uncertainty Quantification and Polynomial Chaos Techniques in Computational Fluid Dynamics," *Annu. Rev. Fluid Mech.*, Vol. 41, 2009, pp. 35–52.

[7] Hosder, S. and Bettis, B., "Uncertainty and Sensitivity Analysis for Reentry Flows with Inherent and Model-Form Uncertainties," *Journal of Spacecraft and Rockets*, Vol. 49, No. 2, 2012, pp. 193–206.

[8] Bettis, B., Hosder, S., and Winter, T., "Efficient Uncertainty Quantification in Multidisciplinary Analysis of a Reusable Launch Vehicle," AIAA Paper 2011-2393, April 2011.

[9] Hosder, S., Walters, R. W., and Balch, M., "Efficient Sampling for Non-Intrusive Polynomial Chaos Applications with Multiple Uncertain Input Variables," AIAA Paper 2007-1939, April 2007.

[10] Hosder, S., Walters, R. W., and Balch, M., "Point-Collocation Nonintrusive Polynomial Chaos Method for Stochastic Computational Fluid Dynamics," *AIAA Journal*, Vol. 48, No. 12, 2010, pp. 2721–2730.

[11] Eldred, M. S., "Recent Advances in Non-Intrusive Polynomial Chaos and Stochastic Collocation Methods for Uncertainty Analysis and Design," AIAA Paper 2009-2274, May 2009.

[12] Lockwood, B. and Mavriplis, D., "Gradient-Based Methods for Uncertainty Quantification in Hypersonic Flows," *Computers and Fluids Journal*, Vol. 85, No. 1, Oct. 2013, pp. 27–38.

[13] Roderick, O., Anitescu, M., and Fischer, P., "Polynomial Regression Approaches Using Derivative Information for Uncertainty Quantification," *Nuclear Science and Engineering*, Vol. 164, No. 2, 2010, pp. 122–139.

[14] Doostan, A. and Owhadi, H., "A non-adapted sparse approximation of PDEs with stochastic inputs," *Journal of Computational Physics*, Vol. 230, No. 8, 2011, pp. 3015–3034.

[15] Witteveen, J., Duraisamy, K., and Iaccarino, G., "Uncertainty Quantification and Error Estimation in Scramjet Simulation," AIAA Paper 2011-2283, April 2011.

[16] Hosder, S. and Maddalena, L., "Efficient Uncertainty Quantification for the Design of a Supersonic Pressure Probe," AIAA Paper 2009-2285, May 2009.

[17] Suga, Y. and Yamazaki, W., "Aerodynamic Uncertainty Quantification of Supersonic Biplane Airfoil via Polynomial Chaos Approach," AIAA Paper 2015-1815, Jan. 2015.

[18] Kulakhmetov, M. and Alexeenko, A., "Modeling Uncertainties in Direct Simulation Monte Carlo Calculations of Hypersonic Leading Edge Flows," *Journal of Spacecraft and Rockets*, Vol. 49, No. 3, 2012, pp. 461–473.

[19] Sharp, D. H. and Wood-Schultz, M. M., "QMU and Nuclear Weapons Certification. Whats Under the Hood," *Los Alamos Science*, , No. 28, 2003, pp. 47–53.

[20] Eardley, D., "Quantification of Margins and Uncertainties (QMU)," Tech. Rep. JSR-04-330 (JASON), EECS Department, University of California, Berkeley, mar 2005.

[21] Pilch, M., Trucano, T. G., and Helton, J. C., "Ideas Underlying Quantification of Margins and Uncertainties (QMU): A White Paper," *Sandia National Laboratories Report*, Vol. SAND2006-5001, Sept. 2006.

[22] Helton, J. C., "Conceptual and Computational Basis for the Quantification of Margins and Uncertainty," *Sandia National Laboratories Report*, Vol. SAND2009-3055, June 2009.

[23] Romero, V. J., "Some Issues and Needs in Quantification of Margins and Uncertainty in Complex Coupled Systems," AIAA Paper 2006-1989, May 2006.

[24] Pepin, J. E., Rutherford, A. C., and Hemez, F. M., "Defining a Practical QMU Metric," AIAA Paper 2008-1717, April 2008.

[25] Iaccariono, G., Pecnik, R., Glimm, J., and Sharp, D., "A QMU Approach for Characterizing the Operability Limits of Air-Breathing Hypersonic Vehicles," *LANL Report*, Vol. LA-UR 09-01863, 2009.

[26] Lucas, L. J., Owhadi, H., and Ortiz, M., "Rigorous Verification, Validation, Uncertainty Quantification and Certification Through Concentration-of-Measure Inequalities," *Computer Methods in Applied Mechanics and Engineering*, Vol. 197, 2008, pp. 4591–4609.

[27] Swiler, L. P., Paez, T. L., Mayes, R. L., and Eldred, M. S., "Epistemic Uncertainty in the Calculation of Margins," AIAA Paper 2009-2249, May 2009.

[28] Oberkampf, W., Helton, J., and Sentz, K., "Mathematical representation of uncertainty," AIAA Paper 2001-1645, June 2001.

[29] Eldred, M. and Swiler, L., "Efficient Algorithms for Mixed Aleatory-Epistemic Uncertainty Quantification with Application to Radiation-Hardened Electronics," *Sandia National Laboratories Report*, Vol. SAND2009-5805, Sept. 2009.

[30] Witteveen, J. A. S. and Bijl, H., "Efficient Quantification of the Effect of Uncertainties in AdvectionDiffusion Problems Using Polynomial Chaos," *Numerical Heat Transfer*, Vol. 53, No. 5, 2008, pp. 437–465.

[31] Han, D. and Hosder, S., "Inherent and Model-Form Uncertainty Analysis for CFD Simulation of Synthetic Jet Actuators," AIAA Paper 2012-0082, Jan. 2012.

[32] West IV, T. K., Hosder, S., and Johnston, C. O., "Multi-Step Uncertainty Quantification Approach Applied to Hypersonic Reentry Flows," *Journal of Spacecraft and Rockets*, Vol. 51, No. 1, 2014, pp. 296–310.

[33] West IV, T. K., Hosder, S., and Johnston, C. O., "A Multi-Step Uncertainty Quantification Approach Applied to Hypersonic Reentry Flows," AIAA Paper 2011-2524, Grapevine, TX, Jan. 2013.

[34] Sudret, B., "Global sensitivity analysis using polynomial chaos expansion," *Reliability Engineering and System Safety*, Vol. 93, No. 7, 2008, pp. 964–979.

[35] Ghaffari, S., Magin, T., and Iaccarino, G., "Uncertainty Quantification of Radiative Heat Flux Modeling for Titan Atmospheric Entry," AIAA Paper 2010-0239, Jan. 2010.

[36] Fay, J. A. and Riddell, F. R., "Theory of stagnation point heat transfer in dissociated air," *Journal of Aeronautical Sciences*, Vol. 25, No. 25, 1958, pp. 73–85.

[37] Anderson Jr., J. D., *Hypersonic and High-Temperature Gas Dynamics*, American Institute of Aeronautics and Astronautics, Reston, VA, 2nd ed., 2006.

[38] Tannehill, J. C. and Mugge, P. H., "Improved Curve Fits for the Thermodynamic Properties of Equilibrium Air Suitable for Numerical Computation Using Time-Dependent or Shock-Capturing Methods," Tech. rep., NASA/CR-2470, Oct. 1974.

[39] Johnston, C. O., Brandis, A. M., and Sutton, K., "Shock Layer Radiation Modeling and Uncertainty for Mars Entry," AIAA Paper 2012-2866, June 2012.

[40] Mazaheri, A., Gnoffo, P. A., Johnston, C. O., and Kleb, B., "LAURA Users Manual: 5.4-54166," Tech. rep., NASA/TM-2011-217092, May 2009.

[41] Johnson, C. O., Hollis, B. R., and Sutton, K., "Spectrum Modeling for Air Shock-layer Radiation at Lunar-Return Conditions," *Journal of Spacecraft and Rockets*, Vol. 45, No. 5, 2008, pp. 865–878.

[42] Johnson, C. O., Hollis, B. R., and Sutton, K., "Non-Boltzman Modeling for Air Shock Layers at Lunar Return Conditions," *Journal of Spacecraft and Rockets*, Vol. 45, No. 5, 2008, pp. 879–890.

[43] Yang, A., Ganesh, A., Sastry, S., and Ma, Y., "Fast L1-Minimization Algorithms and An Application in Robust Face Recognition: A Review," Tech. Rep. UCB/EECS-2010-13, EECS Department, University of California, Berkeley, Feb 2010.

[44] Asif, M. S. and Romberg, J., "Fast and Accurate Algorithms for Re-Weighted l_1-Norm Minimization," *IEEE Transactions on Signal Processing*, Vol. 61, No. 23, 2013, pp. 5905–4916.

[45] Blatman, G. and Sudret, B., "Adaptive sparse polynomial chaos expansion based on least angle regression," *Journal of Computational Physics*, Vol. 230, No. 6, 2011, pp. 2345–2367.

[46] Gnoffo, P. A., Gupta, R. N., and Shinn, J. L., "Conservation Equations and Physical Models for Hypersonic Air Flows in Thermal and Chemical Nonequilibrium," Tech. rep., NASA TP 2867, Feb. 1989.

[47] Park, C., Howe, J. T., Jaffe, R. L., and Candler, G. V., "Review of Chemical-Kinetic Problems for Future NASA Missions, II: Mars Entries," *Journal of Thermophysics and Heat Transfer*, Vol. 8, No. 1, 1994, pp. 9–23.

[48] Bose, D., Wright, M., and Gokcen, T., "Uncertainty and Sensitivity Analysis of Thermochemical Modeling for Titan Atmospheric Entry," AIAA Paper 2004-2455, June 2004.

[49] Ralchenko, Y., Jou, F. C., Kelleher, D. E., Kramida, A. E., Musgrove, A., Reader, J., Wiese, W. L., and Olsen, K., "NIST Atomic Spectra Database, Version 3.1.0," July 2006.

[50] The Opacity Project Team, *The Opacity Project*, Vol. 1, 1995.

[51] Cunto, W., Mendoza, C., Ochsenbein, F., and Zeippen, C., "TOPbase at the CDS," *Astronomy and Astrophysics*, Vol. 275, 1993, pp. L5–L8.

[52] Wright, M., Bose, D., and Olejniczak, J., "Impact of Flowfield-Radiation Coupling on Aeroheating for Titan Aerocapture," *Journal of Thermophysics and Heat Transfer*, Vol. 19, No. 1, 2005, pp. 17–27.

[53] Johnston, C. O., Hollis, B. R., and Sutton, K., "Radiative Heating Methodology for the Huygens Probe," *Journal of Spacecraft and Rockets*, Vol. 44, No. 5, 2007, pp. 993–1002.

[54] Lingard, J. S. and Underwood, J. C., "Huygens DCSS Post Flight Reconstruction," AIAA Paper 2007-2579, May 2007.

[55] Kazeminejad, B., Atkinson, D. H., Perez-Ayucar, M., Lebrenton, J., and Sollazzo, C., "Huygens entry and descent through Titan's atmosphereMethodology and results of the trajectory reconstruction," *Planetary and Space Science*, Vol. 55, No. 13, 2007, pp. 1845–1876.

[56] Brune, A. J., West IV, T. K., and Hosder, S., "Comprehensive Uncertianty Analysis of Mars Entry Flows Over Hypersonic Inflatable Atmospheric Decelerators," AIAA Paper 2014-2805, June 2014.

[57] "TSSM in situ elements, ESA contribution to the Titan Saturn System Mission, Assessment Study Report," Tech. Rep. ESA-SRE (2008)4, ESA, 2008.

[58] Takashima, N., Hollis, B., Olejniczak, J., Wright, M., and Sutton, K., "Preliminary Aerothermodynamics of Titan Aerocapture Aeroshell," AIAA Paper 2003-4952, July 2003.

[59] Olejniczak, J., Prabhu, D., Wright, M., Takashima, N., Hollis, B., Sutton, K., and Zoby, V., "An Analysis of the Radiative Heating for Titan Aerocapture at Titan," AIAA Paper 2003-4953, July 2003.

[60] Olejniczak, J., Bose, D., and Wright, M., "Aeroheating Analysis for the Afterbody of a Titan Probe," AIAA Paper 2004-0486, Jan. 2004.

[61] Johnston, J. O., Mazaheri, A., Gnoffo, P., Kleb, B., and Bose, D., "Radiative Heating Uncertainty for Hyperbolic Earth Entry, Part 1: Flight Simulation Modeling and Uncertainty," *Journal of Spacecraft and Rockets*, Vol. 50, No. 1, 2013, pp. 19–38.

[62] Gokcen, T., "N2-CH4-Ar Chemical Kinetic Model for Simulations of Atmospheric Entry to Titan," *Journal of Thermophysics and Heat Transfer*, Vol. 21, No. 1, 2007, pp. 9–18.

[63] Ndiaye, A. A. and Lago, V., "Optical spectroscopy investigation of N2-CH4 plasma jets simulating Titan atmospheric entry conditions," *Plasma Sources Sci. Technol.*, Vol. 20, No. 1, 2011.

[64] Brandis, A. M., Laux, C. O., Magin, T., McIntyre, T. J., and Morgan, R. G., "Comparison of Titan Entry Radiation Shock-Tube Data with Collisional-Radiative Models," *Journal of Thermophysics and Heat Transfer*, Vol. 28, No. 1, 2014, pp. 32–38.

[65] Brandis, A. M., Morgan, R. G., McIntyre, T., and Jacobs, P. A., "Nonequilibrium Radiation Intensity Measurements in Simulated Titan Atmospheres," AIAA Paper 2008-4136, June 2008.

[66] Bose, D. and Wright, M. J., "View-Factor Based Radiation Transport in a Hypersonic Shock Layer," *Journal of Thermophysics and Heat Transfer*, Vol. 18, No. 4, 2004, pp. 553–555.

[67] Mazaheri, A., Johnston, C. O., and Sefidbakht, S., "Three-Dimensional Radiation Ray-Tracing for Shock-Layer Radiative Heating Simulations," *Journal of Spacecraft and Rockets*, Vol. 50, No. 3, 2013, pp. 485–493.

[68] Kreinovich, K. and Nguyen, H. T., "Towards a Neural-Based Understanding of the Cauchy Deviate Method for Processing Interval and Fuzzy Uncertainty," Proceedings of Joint 2009 International Fuzzy Systems Association World Congress and 2009 European Society of Fuzzy Logic and Technology Conference, July 2009.

[69] Johnston, C. O. and Kleb, B., "Uncertainty Analysis of Air Radiation for Lunar-Return Shock Layers," *Journal of Spacecraft and Rockets*, Vol. 49, No. 3, 2012, pp. 425–434.

[70] Brandis, A. M., Morgan, R. G., and McIntyre, T. J., "Analysis of Nonequilibrium CN Radiation Encountered During Titan Atmospheric Entry," *Journal of Thermophysics and Heat Transfer*, Vol. 25, No. 4, 2011, pp. 493–499.

[71] West IV, T. K., Brune, A. J., and Hosder, S., "Uncertainty Analysis of Radiative Heating for Multiple Planetary Entry Cases (Invited)," AIAA Paper 2014-2805, June 2014.

[72] *NIST/SEMATECH e-Handbook of Statistical Methods*, 2013.

[73] De Zaiacomo, G., M., K., Haya, R., and Penin, L. F., "Robust Skip Entry Guidance and Control for a Capsule Returning from Lunar Orbit," AIAA Paper 2009-5771, Aug. 2009.

[74] Hoelscher, B., "Orion Entry, Descent, and Landing," AIAA Paper 2007-6428, Aug. 2007.

[75] Berger, K., "Aerothermodynamic Testing of the Crew Exploration Vehicle in the LaRC 20-Inch Mach 6 and 31-Inch Mach 10 Tunnels," AIAA Paper 2008-1225, Jan. 2008.

[76] Xue, S. and Lu, P., "Constrained Predictor-Corrector Entry Guidance," *Journal of Guidance, Control, and Dynamics*, Vol. 33, No. 4, 2010, pp. 1273–1281.

[77] Brunner, C., , and Lu, P., "Skip Entry Trajectory Planning and Guidance," AIAA Paper 2007-6777, Aug. 2007.

[78] D'Souza, S.and Sarigul-Klijn, N., "Investigation of Trajectory Generation for a Mission Adaptive Planetary Entry Guidance Algorithm," AIAA Paper 2012-4508, Aug. 2012.

[79] Hoelscher, B. R., Strahan, A. L., Stachowiak, S. J., and Loe, G. R., "Orion Entry Flight Control Modifications and Performance," AIAA Paper 2008-7152, Aug. 2008.

[80] Trumble, K., Cozmuta, I., Sepka, S., Jenniskens, P., and Winter, M., "Postflight Aerothermal Analysis of Stardust Sample Return Capsule," *Journal of Spacecraft and Rockets*, Vol. 47, No. 5, 2010, pp. 765–774.

[81] Chen, Y., Squire, T., Laub, B., and Wright, M., "Monte Carlo Analysis for Thermal Protection System Design," AIAA Paper 2006-2951, June 2006.

[82] Shang, J. and Surzhikov, T., "Simulating Stardust Earth Reentry with Radiation Heat Transfer," *Journal of Spacecraft and Rockets*, Vol. 48, No. 3, 2011, pp. 385–396.

[83] Rallabhandi, S., Nielsen, E., and Diskin, B., "Sonic-Boom Mitigation Through Aircraft Design and Adjoint Methodology," *Journal of Aircraft*, Vol. 51, No. 2, March–April 2014, pp. 502–510.

[84] Biedron, R. T. and et al., "FUN3D Manual: 12.4-69883," Tech. rep., NASA/TM-2014-218179, March 2014.

[85] Park, M. A., "Low Boom Configuration Analysis with FUN3D Adjoint Simulation Framework," AIAA Paper 2011-3337, June 2011.

[86] Park, M. A., Cambell, R. L., Elmiligui, A., Cliff, S. E., and Nayani, S. N., "Specialized CFD Grid Generation Methods for Near-Field Sonic Boom Prediction," AIAA Paper 2014-0115, Jan. 2014.

[87] Casper, J. H., Cliff, S. E., Thomas, S. D., Park, M. A., McMullen, M. S., Melton, J. E., and Durston, D. A., "Assessment of Near-Field Sonic Boom Simulation Tools," AIAA Paper 2008-6592, Aug. 2008.

[88] Spalart, P. R. and Allmaras, S. R., "One-Equation Turbulence Model for Aerodynamic Flows," AIAA Paper 92-1992, Jan. 1992.

[89] Morgenstern, J., Norstrud, N., Sokhey, J., Martens, S., and Alonso, J. J., "Advanced Concept Studies for Supersonic Commercial Transports Entering Service in the 2018 to 2020 Period," NASA CR-2013-217820, NASA Langley Research Center, Feb. 2013.

[90] Hunton, L. W., Hicks, R. M., and Mendoza, J. P., "Some Effects of Wing Planform on Sonic Boom," Tech. rep., NASA TN D-7160, Jan. 1973.

[91] Morgenstern, J. M., Buonanno, M., and Marconi, F., "Full Configuration Low Boom Model and Grids for 2014 Sonic Boom Prediction Workshop," AIAA Paper 2013-0647, Grapvine, TX, Jan. 2013.

[92] Jones, W. T., "GridEx - An Integrated Grid Generation Package for CFD," AIAA Paper 2003-4129, Aug. 2003.

[93] Rallabhandi, S. K., "Advanced Sonic Boom Prediction Using the Augmented Burgers Equation," *Journal of Aircraft*, Vol. 48, No. 4, July–Aug. 2011, pp. 1245–1253.

[94] Cliff, S. E., Durston, D. A., Elmiligui, A. A., Jensen, J. C., and Chan, W. M., "Computational and Experimental Assessment of Models for the First AIAA Sonic Boom Prediction Workshop," AIAA Paper 2014-0560, Jan. 2014.

[95] Loubeau, A. and Coulouvrat, F., "Effects of Meteorological Variability on Sonic Boom Propagation from Hypersonic Aircraft," *AIAA Journal*, Vol. 47, No. 11, Nov. 2009, pp. 2632–2641.

VITA

Thomas Kelsey West IV was born in Lake St. Louis Missouri. After graduating from Troy Buchanan High School in Troy, MO in 2006, he began his undergraduate education at the Missouri University of Science and Technology. Over the course of his undergraduate education, he was selected for the NASA Undergraduate Student Research Program where he spent a semester at NASAs Jet Propulsion Laboratory in 2008. In 2010, Thomas graduated Summa Cum Laude earning Bachelor of Science degrees in both Aerospace Engineering and Mechanical Engineering, as well as an undergraduate minor in Applied Mathematics. He then continued his education earning a Master of Science degree in Aerospace Engineering from the Missouri University of Science and Technology in 2012 and a Doctor of Philosophy in Aerospace Engineering in 2015. As a graduate student, Thomas had multiple internships at the NASA Langley Research Center, spanning over two years.